VARIATIONS OF SOURCE PARAMETERS DUE TO ANISOTROPIC FOCAL REGION

by

Deniz Ertuncay

B.S., Geophysical Engineering, İstanbul University, 2013

Submitted to the Kandilli Observatory and Earthquake Research Institute in partial fulfillment of the requirements for the degree of Master of Science

Graduate Program in Geophysics

Boğaziçi University

2016

ACKNOWLEDGEMENTS

I would first like to thank my thesis advisor Assistant Prof. Dr. Çağrı Diner of the Geophysics Department at Boğaziçi University. He consistently allowed this thesis to be my own work, but steered me in the right the direction whenever he thought I needed it.

My completion of this project could not have been accomplished without the support of my classmates, Rıdvan Örsvuran and Ekrem Bekin.

I would also like to acknowledge Assoc. Prof. Dr. Ali Özgün Konca of the Geophysics Department at Boğaziçi University as the second reader of this thesis, and I am gratefully indebted to his for his very valuable comments on this thesis.

Finally, I take this opportunity to express the profound gratitude from my deep heart to my beloved parents and grandparents for their love and continuous support – both spiritually and materially. This thesis would not have been finished without their supports. Thank you.

ABSTRACT

VARIATIONS OF SOURCE PARAMETERS DUE TO ANISOTROPIC FOCAL REGION

Seismic sources in anisotropic medium have more complex moment tensor structures compared with the moment tensors of isotropic medium. Shear sources in an isotropic focal medium generate pure double-couple (DC) moment tensors. However in an anisotropic medium, shear sources can generate moment tensors with DC, compensated linear vector dipole (CLVD) and isotropic (ISO) components. The DC, CLVD and ISO percentages of a moment tensor depend on the magnitude and the orientation of the anisotropy.

In this study, we choose five fault types namely, left/right strike slip, normal, reverse and dip-slip faults in a medium of different anisotropy classes; transversely isotropic, orthotropic and monoclinic. We rotated the anisotropic elasticity tensors of the medium for every possible orientation and evaluate the moment tensors of each cases. Then moment tensor decomposition is applied and DC, CLVD and ISO components are found. We plot the DC, CLVD and ISO percentages of the moment tensors generated by different fault types and anisotropy classes. By using the DC components, first we obtained fault plane orientation then we calculate the deviation from the original fault mechanism. Effects of anisotropy of the source region on calculated fault parameters are found. Distance from isotropic space of given anisotropic elasticity tensor and P/S wave velocity anisotropy percentages are measured. These percentages are proportional to the distane from isotropy. There is a correlation between distance to isotropy and P wave anisotropy with variation of fault plane parameters and percentages of non-DC components of earthquake source.

ÖZET

ANİZOTROPİK DEPREM ODAĞININ KAYNAK PARAMETERLERİNDE YARATTIĞI DEĞİŞİMLER

İzotropik ortamdaki sismik kaynaklar anizotropik ortamdakilere göre daha karmaşık moment tensörü yapısına sahiptirler. İzotropik ortamdaki kayma şeklinde oluşan depremler tamamen çift kuvvet çifti (DC) özelliğine sahip moment tensörler üretirler. Anizotropik ortamdaki kayma şeklinde oluşan depremler ise çift kuvvet çifti, izotropik (ISO) ve telafi edilmiş doğrusal vektör dipolleri (CLVD) bileşenler üretir. Moment tensörde bulunan DC, CLVD ve ISO yüzdeleri anizotropinin yüzdesine, yönelimine ve büyüklüğüne bağlıdır.

Bu çalışmada normal fay, ters fay, eğim atımlı fay, sol yanal atımlı fay ve sağ yanal atımlı fay olmak üzere beş ana fay türü seçilmiştir. Bu fay türleri enine izotropik, ortotropik ve monoklinik simetri sınıflarına sahip altı farklı materyalden oluşan ortamlara uygulanmıştır. Anizotropik elastisite tensörü olası bütün açılarda döndürülmüş ve her döndürmede oluşan yeni elastisite tensörü kullanılarak moment tensörler üretilmiştir. Sonrasında bu moment tensörlerin moment tensör çözümleri yapılmış ve ISO, CLVD ve DC bileşenleri bulunmuştur. Moment tensörlerin DC, CLVD ve ISO yüzdeleri farklı fay türleri için çizdirilmiştir. DC bileşeni kullanarak fay düzlemi oryantasyonu bulunmuş ve orjinal fay düzlemi parameterlerinden olan sapmaları hesaplanmıştır. Anizotropik ortamın fay düzlemi parametreleri üzerindeki etkisi bulunmuştur. Verilen anizotropik materyalin en yakın izotropik uzaya ulan uzaklığı bulunmuştur. MTEX yazılımı kullanılarak P ve S dalgası anizotropileri bulunmuş ve P ve S dalgası azinotropi yüzdelerinin elastisite tensörlerinin izotropik uzaya ulan uzaklıkları ile ilişkilendirilmiştir. P dalgası anizotropi yüzdesi ve elastisite tensörlerinin izotropik uzaya olan uzaklıklarının fay parametrelerindeki değişmde ve çift kuvvet çifti olmayan kaynağın yüzdesi arasında bir ilişki olduğu bulunmuştur.

TABLE OF CONTENTS

ACKNOWLEDGEMENTS . . . iii

ABSTRACT . . . iv

ÖZET . . . v

LIST OF FIGURES . . . ix

LIST OF TABLES . . . xix

LIST OF SYMBOLS . . . xx

LIST OF ACRONYMS/ABBREVIATIONS . . . xxii

1. INTRODUCTION . . . 1

2. DATA AND METHOD . . . 4

  2.1. Fault Plane Parameters . . . 4

  2.2. Elasticity Tensor . . . 5

  2.3. Orthogonal Transformations . . . 6

  2.4. Rotation of an Elasticity Tensor . . . 9

  2.5. Anisotropy Classes . . . 11

    2.5.1. Transversely Isotropic . . . 12

    2.5.2. Orthotropic . . . 12

    2.5.3. Monoclinic . . . 13

  2.6. Moment Tensor . . . 14

  2.7. Eigenvalues of Moment Tensor . . . 19

  2.8. Moment Tensor of Shear Faulting for Different Anisotropy Classes With Varying Orientations . . . 23

  2.9. Moment Tensor Decomposition . . . 25

  2.10. Physical Interpretation of Non-DC Components . . . 27

  2.11. Determining Closest Isotropic Elasticity Tensor . . . 29

  2.12. Data . . . 30

    2.12.1. Elasticity Tensors . . . 30

      2.12.1.1. Transversely Isotropic Elasticity Tensors . . . 30

      2.12.1.2. Orthotropic Elasticity Tensors . . . 33

2.12.1.3. Monoclinic Elasticity Tensors 35
2.12.2. Fault Parameters 37
3. RESULTS 39
3.1. Variation on Fault Angles 40
3.1.1. Gneiss 40
3.1.2. Amphibolite 42
3.1.3. Granite 44
3.1.4. Tonga Deep Zone 47
3.1.4.1. Normal Fault 47
3.1.4.2. Reverse Fault 50
3.1.4.3. Dip-Slip Fault 53
3.1.4.4. Left Lateral Strike Slip Fault 56
3.1.4.5. Right Lateral Strike Slip Fault 59
3.1.5. Albite 62
3.1.6. Sanidine 65
3.2. Variation on Non Double Couple Sources 68
3.2.1. Gneiss 68
3.2.2. Amphibolite 69
3.2.3. Granite 70
3.2.4. Tonga Deep Zone 70
3.2.4.1. Normal Fault 72
3.2.4.2. Reverse Fault 75
3.2.4.3. Dip-Slip Fault 78
3.2.4.4. Left Lateral Strike Slip Fault 81
3.2.4.5. Right Lateral Strike Slip Fault 84
3.2.5. Albite 87
3.2.6. Sanidine 89
3.3. Distance From Closest Isotropic Space 91
3.3.1. MTEX Results 91
4. DISCUSSION 98
5. CONCLUSION 102

REFERENCES 104
APPENDIX A: DISTANCE FUNCTION 110
APPENDIX B: VOIGT AND KELVIN NOTATIONS OF ELASTICITY TENSOR . 111
APPENDIX C: SYMMETRY CLASSES 116
C.1. Isotropic 116
C.2. Cubic 116
C.3. Tetragonal 117
C.4. Trigonal 118
C.5. Generally Anisotropic 118

LIST OF FIGURES

Figure 2.1. Fault Plane Representation in Cartesian Coordinates 5

Figure 2.2. Graphical representation of elementary transformations by using rotation matrices. $\{e_1, e_2, e_3\}$ coordinate system transformed to $\{e_1^{'}, e_2^{'}, e_3^{'}\}$ by using ψ, ϕ and θ. 10

Figure 2.3. Orders of eight rotation classes. Arrows indicates subgroup relations. For instance; Orthotropic is a subgroup of Tetragonal. Symmetry classes rather than TI, Monoclinic and orthotropic are explained in Appendix C 14

Figure 2.4. The nine generalized couples [1] 16

Figure 2.5. Body forces equivalents of ISO and CLVD components. In this figure both ISO and CLVD components have positive signs. Negative signs of ISO and CLVD components can be obtained by reversing the arrows. 28

Figure 2.6. Distance Function of Elasticity tensor of Gneiss. Distance function calculates the distance between given elasticity tensor and monoclinic space [2]. By using these figure we can see the symmetry or the orientation of the elasticity tensor of layering. Dark blue represent the normal of the mirror plane orientation. 31

Figure 2.7. Distance Function of Elasticity tensor of Amphibolite 32

Figure 2.8. Distance Function of Elasticity tensor of Granite. Thus we can see that there are three mirror planes that orthogonal to each other. Dark blue represent the normal of the mirror plane orientation. 34

Figure 2.9. Distance Function of Elasticity tensor of Tonga Deep Zone . . 35

Figure 2.10. Distance Function of Elasticity tensor of Albite. Monoclinic elasticity tensor has only one mirror plane. Dark blue represent the normal of the mirror plane orientation. 36

Figure 2.11. Distance Function of Elasticity tensor of Sanidine. Dark blue represent the normal of the mirror plane orientation. However, figure suggest that corresponding elasticity tensor is close to orthotropic symmetry. 37

Figure 3.1. Variation of Fault parameters Φ (a), δ (b) and λ (c) of Gneiss. Red arrow ($\mathbf{u}$) and green arrow ($\mathbf{v}$) are slip vector and fault normal, respectively. Red colored areas imply high variations and dark blue colored areas imply low or no variations. ψ angle increase from left to right on figures. ϕ angle increase from North pole to South pole for fixed ψ angle. 41

Figure 3.2. Variation of Fault parameters Φ (a), δ (b) and λ (c) of Amphibolite. Red arrow ($\mathbf{u}$) and green arrow ($\mathbf{v}$) are slip vector and fault normal, respectively. Red colored areas imply high variations and dark blue colored areas imply low or no variations. ψ angle increase from left to right on figures. ϕ angle increase from North pole to South pole for fixed ψ angle. 43

Figure 3.3. Maximum variation of Fault parameters Φ (a), δ (b) and λ (c) of Granite. Red arrow ($\mathbf{u}$) and green arrow ($\mathbf{v}$) are slip vector and fault normal, respectively. Red colored areas imply high variations and dark blue colored areas imply low or no variations. ψ angle increase from left to right on figures. ϕ angle increase from North pole to South pole for fixed ψ angle. 45

Figure 3.4. Mean variation of Fault parameters Φ (a), δ (b) and λ (c) of Granite. Red arrow ($\mathbf{u}$) and green arrow ($\mathbf{v}$) are slip vector and fault normal, respectively. Red colored areas imply high variations and dark blue colored areas imply low or no variations. ψ angle increase from left to right on figures. ϕ angle increase from North pole to South pole for fixed ψ angle. 46

Figure 3.5. Maximum variation of fault parameters Φ (a), δ (b) and λ (c) of Tonga Deep Zone for Normal Fault. Red arrow (**u**) and green arrow (**v**) are slip vector and fault normal, respectively. Red colored areas imply high variations and dark blue colored areas imply low or no variations. ψ angle increase from left to right on figures. ϕ angle increase from North pole to South pole for fixed ψ angle. 48

Figure 3.6. Mean variation of fault parameters Φ (a), δ (b) and λ (c) of Tonga Deep Zone for Normal Fault. Red arrow (**u**) and green arrow (**v**) are slip vector and fault normal, respectively. Red colored areas imply high variations and dark blue colored areas imply low or no variations. ψ angle increase from left to right on figures. ϕ angle increase from North pole to South pole for fixed ψ angle. 49

Figure 3.7. Maximum variation of fault parameters Φ (a), δ (b) and λ (c) of Tonga Deep Zone for Reverse Fault. Red arrow (**u**) and green arrow (**v**) are slip vector and fault normal, respectively. Red colored areas imply high variations and dark blue colored areas imply low or no variations. ψ angle increase from left to right on figures. ϕ angle increase from North pole to South pole for fixed ψ angle. 51

Figure 3.8. Mean variation of fault parameters Φ (a), δ (b) and λ (c) of Tonga Deep Zone for Reverse Fault. Red arrow (**u**) and green arrow (**v**) are slip vector and fault normal, respectively. Red colored areas imply high variations and dark blue colored areas imply low or no variations. ψ angle increase from left to right on figures. ϕ angle increase from North pole to South pole for fixed ψ angle. 52

Figure 3.9. Maximum variation of fault parameters Φ (a), δ (b) and λ (c) of Tonga Deep Zone for Dip-Slip Fault. Red arrow (**u**) and green arrow (**v**) are slip vector and fault normal, respectively. Red colored areas imply high variations and dark blue colored areas imply low or no variations. ψ angle increase from left to right on figures. ϕ angle increase from North pole to South pole for fixed ψ angle. 54

Figure 3.10. Mean variation of fault parameters Φ (a), δ (b) and λ (c) of Tonga Deep Zone for Dip-Slip Fault. Red arrow (**u**) and green arrow (**v**) are slip vector and fault normal, respectively. Red colored areas imply high variations and dark blue colored areas imply low or no variations. ψ angle increase from left to right on figures. ϕ angle increase from North pole to South pole for fixed ψ angle. 55

Figure 3.11. Maximum variation of fault parameters Φ (a), δ (b) and λ (c) of Tonga Deep Zone for Left Lateral Strike Slip Fault. Red arrow (**u**) and green arrow (**v**) are slip vector and fault normal, respectively. Red colored areas imply high variations and dark blue colored areas imply low or no variations. ψ angle increase from left to right on figures. ϕ angle increase from North pole to South pole for fixed ψ angle. 57

Figure 3.12. Mean variation of fault parameters Φ (a), δ (b) and λ (c) of Tonga Deep Zone for Left Lateral Strike Slip Fault. Red arrow (**u**) and green arrow (**v**) are slip vector and fault normal, respectively. Red colored areas imply high variations and dark blue colored areas imply low or no variations. ψ angle increase from left to right on figures. ϕ angle increase from North pole to South pole for fixed ψ angle. 58

Figure 3.13. Maximum variation of fault parameters Φ (a), δ (b) and λ (c) of Tonga Deep Zone for Right Lateral Strike Slip Fault. Red arrow (**u**) and green arrow (**v**) are slip vector and fault normal, respectively. Red colored areas imply high variations and dark blue colored areas imply low or no variations. ψ angle increase from left to right on figures. ϕ angle increase from North pole to South pole for fixed ψ angle. 60

Figure 3.14. Mean variation of fault parameters Φ (a), δ (b) and λ (c) of Tonga Deep Zone for Right Lateral Strike Slip Fault. 61

Figure 3.15. Maximum variation of Fault parameters Φ (a), δ (b) and λ (c) of Albite. Red arrow (**u**) and green arrow (**v**) are slip vector and fault normal, respectively. Red colored areas imply high variations and dark blue colored areas imply low or no variations. ψ angle increase from left to right on figures. ϕ angle increase from North pole to South pole for fixed ψ angle. 63

Figure 3.16. Mean variation of Fault parameters Φ (a), δ (b) and λ (c) of Albite. Red arrow (**u**) and green arrow (**v**) are slip vector and fault normal, respectively. Red colored areas imply high variations and dark blue colored areas imply low or no variations. ψ angle increase from left to right on figures. ϕ angle increase from North pole to South pole for fixed ψ angle. 64

Figure 3.17. Maximum variation of Fault parameters Φ (a), δ (b) and λ (c) of Sanidine. Red arrow (**u**) and green arrow (**v**) are slip vector and fault normal, respectively. Red colored areas imply high variations and dark blue colored areas imply low or no variations. ψ angle increase from left to right on figures. ϕ angle increase from North pole to South pole for fixed ψ angle. 66

Figure 3.18. Mean variation of Fault parameters Φ (a), δ (b) and λ (c) of Sanidine. Red arrow (**u**) and green arrow (**v**) are slip vector and fault normal, respectively. Red colored areas imply high variations and dark blue colored areas imply low or no variations. ψ angle increase from left to right on figures. ϕ angle increase from North pole to South pole for fixed ψ angle. 67

Figure 3.19. Percentage of CLVD (a) and ISO (b) parts of earthquake source of Gneiss. Red arrow (**u**) and green arrow (**v**) are slip vector and fault normal, respectively. Red colored areas imply high percentages and dark blue colored areas imply low or zero percentages. ψ angle increase from left to right on figures. ϕ angle increase from North pole to South pole for fixed ψ angle. 69

Figure 3.20. Percentage of CLVD (a) and ISO (b) parts of earthquake source of Amphibolite. Red arrow (**u**) and green arrow (**v**) are slip vector and fault normal, respectively. Red colored areas imply high percentages and dark blue colored areas imply low or zero percentages. ψ angle increase from left to right on figures. ϕ angle increase from North pole to South pole for fixed ψ angle. 70

Figure 3.21. Percentage of maximum CLVD (a) and ISO (b) parts of earthquake source of Granite. Red arrow (**u**) and green arrow (**v**) are slip vector and fault normal, respectively. Red colored areas imply high percentages and dark blue colored areas imply low or zero percentages. ψ angle increase from left to right on figures. ϕ angle increase from North pole to South pole for fixed ψ angle. 71

Figure 3.22. Percentage of mean CLVD (a) and ISO (b) parts of earthquake source of Granite. Red arrow (**u**) and green arrow (**v**) are slip vector and fault normal, respectively. Red colored areas imply high percentages and dark blue colored areas imply low or zero percentages. ψ angle increase from left to right on figures. ϕ angle increase from North pole to South pole for fixed ψ angle. 71

Figure 3.23. Percentage of maximum positive and negative CLVD (a) and ISO (b) parts of earthquake source of Tonga Deep Zone for Normal Fault. Red arrow (**u**) and green arrow (**v**) are slip vector and fault normal, respectively. Red colored areas imply high percentages and dark blue colored areas imply low or zero percentages for positive result. Indication of colors are reversed for negative results. ψ angle increase from left to right on figures. ϕ angle increase from North pole to South pole for fixed ψ angle. 73

Figure 3.24. Percentage of mean positive and negative CLVD (a) and ISO (b) parts of earthquake source of Tonga Deep Zone for Normal Fault. Red arrow (**u**) and green arrow (**v**) are slip vector and fault normal, respectively. Red colored areas imply high percentages and dark blue colored areas imply low or zero percentages for positive result. Indication of colors are reversed for negative results. ψ angle increase from left to right on figures. ϕ angle increase from North pole to South pole for fixed ψ angle. 74

Figure 3.25. Percentage of maximum positive and negative CLVD (a) and ISO (b) parts of earthquake source of Tonga Deep Zone for Reverse Fault. Red arrow (**u**) and green arrow (**v**) are slip vector and fault normal, respectively. Red colored areas imply high percentages and dark blue colored areas imply low or zero percentages for positive result. Indication of colors are reversed for negative results. ψ angle increase from left to right on figures. ϕ angle increase from North pole to South pole for fixed ψ angle. 76

Figure 3.26. Percentage of mean positive and negative CLVD (a) and ISO (b) parts of earthquake source of Tonga Deep Zone for Normal Fault. Red arrow (**u**) and green arrow (**v**) are slip vector and fault normal, respectively. Red colored areas imply high percentages and dark blue colored areas imply low or zero percentages for positive result. Indication of colors are reversed for negative results. ψ angle increase from left to right on figures. ϕ angle increase from North pole to South pole for fixed ψ angle. 77

Figure 3.27. Percentage of maximum positive and negative CLVD (a) and ISO (b) parts of earthquake source of Tonga Deep Zone for Dip-Slip Fault. Red arrow (**u**) and green arrow (**v**) are slip vector and fault normal, respectively. Red colored areas imply high percentages and dark blue colored areas imply low or zero percentages for positive result. Indication of colors are reversed for negative results. ψ angle increase from left to right on figures. ϕ angle increase from North pole to South pole for fixed ψ angle. 79

Figure 3.28. Percentage of mean positive and negative CLVD (a) and ISO (b) parts of earthquake source of Tonga Deep Zone for Dip-Slip Fault. Red arrow (**u**) and green arrow (**v**) are slip vector and fault normal, respectively. Red colored areas imply high percentages and dark blue colored areas imply low or zero percentages for positive result. Indication of colors are reversed for negative results. ψ angle increase from left to right on figures. ϕ angle increase from North pole to South pole for fixed ψ angle. 80

Figure 3.29. Percentage of maximum positive and negative CLVD (a) and ISO (b) parts of earthquake source of Tonga Deep Zone for Left Lateral Strike Slip Fault. Red arrow (**u**) and green arrow (**v**) are slip vector and fault normal, respectively. Red colored areas imply high percentages and dark blue colored areas imply low or zero percentages for positive result. Indication of colors are reversed for negative results. ψ angle increase from left to right on figures. ϕ angle increase from North pole to South pole for fixed ψ angle. 82

Figure 3.30. Percentage of mean positive and negative CLVD (a) and ISO (b) parts of earthquake source of Tonga Deep Zone for Left Lateral Strike Slip Fault. Red arrow (**u**) and green arrow (**v**) are slip vector and fault normal, respectively. Red colored areas imply high percentages and dark blue colored areas imply low or zero percentages for positive result. Indication of colors are reversed for negative results. ψ angle increase from left to right on figures. ϕ angle increase from North pole to South pole for fixed ψ angle. 83

Figure 3.31. Percentage of maximum positive and negative CLVD (a) and ISO (b) parts of earthquake source of Tonga Deep Zone for Right Lateral Strike Slip Fault. Red arrow (**u**) and green arrow (**v**) are slip vector and fault normal, respectively. Red colored areas imply high percentages and dark blue colored areas imply low or zero percentages for positive result. Indication of colors are reversed for negative results. ψ angle increase from left to right on figures. ϕ angle increase from North pole to South pole for fixed ψ angle. 85

Figure 3.32. Percentage of mean positive and negative CLVD (a) and ISO (b) parts of earthquake source of Tonga Deep Zone for Right Lateral Strike Slip Fault. Red arrow (**u**) and green arrow (**v**) are slip vector and fault normal, respectively. Red colored areas imply high percentages and dark blue colored areas imply low or zero percentages for positive result. Indication of colors are reversed for negative results. ψ angle increase from left to right on figures. ϕ angle increase from North pole to South pole for fixed ψ angle. 86

Figure 3.33. Percentage of maximum CLVD (a) and ISO (b) parts of earthquake source of Albite. Red arrow (**u**) and green arrow (**v**) are slip vector and fault normal, respectively. Red colored areas imply high percentages and dark blue colored areas imply low or zero percentages. ψ angle increase from left to right on figures. ϕ angle increase from North pole to South pole for fixed ψ angle. 88

Figure 3.34. Percentage of mean CLVD (a) and ISO (b) parts of earthquake source of Albite. Red arrow (**u**) and green arrow (**v**) are slip vector and fault normal, respectively. Red colored areas imply high percentages and dark blue colored areas imply low or zero percentages. ψ angle increase from left to right on figures. ϕ angle increase from North pole to South pole for fixed ψ angle. 88

Figure 3.35. Percentage of maximum CLVD (a) and ISO (b) parts of earthquake source of Sanidine. Red arrow (**u**) and green arrow (**v**) are slip vector and fault normal, respectively. Red colored areas imply high percentages and dark blue colored areas imply low or zero percentages. ψ angle increase from left to right on figures. ϕ angle increase from North pole to South pole for fixed ψ angle. 90

Figure 3.36. Percentage of mean CLVD (a) and ISO (b) parts of earthquake source of Sanidine. Red arrow (**u**) and green arrow (**v**) are slip vector and fault normal, respectively. Red colored areas imply high percentages and dark blue colored areas imply low or zero percentages. ψ angle increase from left to right on figures. ϕ angle increase from North pole to South pole for fixed ψ angle. 90

Figure 3.37. P & S wave anisotropies, velocities and polarization and P/S wave ratio of Gneiss 92

Figure 3.38. P & S wave anisotropies, velocities and polarization and P/S wave ratio of Amphibolite 93

Figure 3.39. P & S wave anisotropies, velocities and polarization and P/S wave ratio of Granite 94

Figure 3.40. P & S wave anisotropies, velocities and polarization and P/S wave ratio of Tonga Deep Zone 95

Figure 3.41. P & S wave anisotropies, velocities and polarization and P/S wave ratio of Albite 96

Figure 3.42. P & S wave anisotropies, velocities and polarization and P/S wave ratio of Sanidine 97

LIST OF TABLES

Table 2.1. Fault Parameters 38
Table 3.1. Table of Distance From Isotropic Spaces 91
Table 3.2. P Wave Anisotropy (%) 91
Table 4.1. Moment Tensor Decomposition Results of Elasticity Tensors . . 98

LIST OF SYMBOLS

A	Orthogonal Transformation Tensor
$\overline{A}$	6 x 6 Transformation Tensor
a_i	Orthonormal eigenvector
b	Eigenvector which corresponds the null eigenvalue
C_{ij}	2^{nd} order elasticity tensor
c_{ijpq}	4^{th} order elasticity tensor
c'_{ijpq}	4^{th} order elasticity tensor on a new coordinate frame
D	Slip of a Fault (cm)
d	Fault Vector
$dist_{mono}$	Distance from monoclinic space of a given elasticity tensor
e_i	Unit vector of i^{th} axis
e'_i	Representation of an unit vector of i^{th} axis on a new coordinate frame
F	Applied Force
G_{np}	Green's Function
G^{sym}	Symmetry Group
I	Identity Matrix
L	Dimensions of source
M	Moment Tensor
M_0	Seismic Moment
M_w	Moment Magnitude
m	Moment Density Function
$\overline{m_1}$	Deviatoric Part of **M**
m_i^*	Purely Deviatoric Eigenvalue
r	Distance of the Observation Point
S	Fault Area (km^2)
$pr_{sym}(c)$	Orthogonal Projection
p	Eigenvector which corresponds the negative eigenvalue

tr(M)	Trace of a matrix M
t	Eigenvector which corresponds the positive eigenvalue
u	Slip Vector
$\bar{u}$	Mean Displacement on the Fault Plane
u_n	Displacement on the n direction
v	Fault Normal
x	Location of Reciever
Z_i	i^{th} Euler Rotation Matrix
δ	Dip Angle of a Fault Plane
ε	Strain Tensor
η	Eta
θ	2^{nd} Euler Rotation Angle
λ	Rake Angle of a Fault Plane
λ_{em}	Elasticity Modulus
λ_{wl}	Wavelength
μ	Rigidity
ξ_q	Location of a Source
Σ	Surface Area
σ	Stress Tensor
$\sigma^{'}$	Stress Tensor on a new coordinate frame
τ	Source Time
Φ	Strike Angle of a Fault Plane
ϕ	1^{st} Euler Rotation Angle
ψ	3^{rd} Euler Rotation Angle

LIST OF ACRONYMS/ABBREVIATIONS

6D	Six Dimensional
CLVD	Compensated Linear Vector Dipole
DC	Double Couple
ISO	Isotropic
KTB	German Continental Drilling Program
non-DC	non double couple
TI	Transversely Isotropic

1. INTRODUCTION

In geophysics, fault plane solutions are determined by using the assumption of isotropic seismic source medium. However, earthquake source medium might have anisotropic properties. Anisotropy of a medium has an influence on the calculated moment tensors [1]. Fault plane orientation can change according to isotropic and anisotropic sources. In this thesis, we seek a solution for the problem of effects of anisotropic source medium on calculated fault plane solutions.

In order to determine these effects, one must decompose the moment tensor. There are several moment tensor decomposition methods [3–10]. We used the method proposed by Knopoff [3] and Fitch [5]. Vavryčuk determines the effects of different types of anisotropic source regions on fault plane orientations [9]. Vavryčuk also make an inversion from non double couple (non-DC) of the moment tensors to fin elastic parameters of non-DC parts of earthquake. [11]. Moreover, moment tensors of specific areas and events are obtained Vavryčuk [12], Fojtikova [13] and Stierle [14].

Anisotropy can be seen in Earth's crust and upper mantle [15–18]. Layered geological structures, micro cracks, fluid injections in geothermal or volcanic areas, fractures or atomic texture of mineral can cause anisotropy [19–25].

Moreover, these properties of geological formations can cause seismic anisotropy. Seismic anisotropy is related with the change of seismic wave velocities depending on the orientation of the ray propagating in an anisotropic medium. Thus it is usually understood as a structural property of the medium [26–28]. Anisotropy of source medium is directly affects the moment tensor which contains important information of the earthquake. Type of the faulting mechanism is one of them. For instance, shear faulting with anisotropic source medium can cause non-DC components [29]. Since non-DC components can be seen in many earthquakes [6, 7, 30, 31], this problem is worth to be considered as an important one.

Seismic sources in anisotropic medium have more complex moment tensor structures compared with the moment tensors of isotropic medium. It is a well known fact that shear sources in an isotropic elasticity tensor, seismic sources generate pure double-couple (DC) moment tensors. However, in anisotropic source medium, shear seismic sources can generate moment tensors with DC, compensated linear vector dipole (CLVD) and isotropic (ISO) components. The DC, CLVD and ISO percentages of the moment tensors depend on the magnitude of the anisotropy.

In this thesis, for simplicity, five fundamental fault types, left/right lateral strike slip, normal, reverse and dip-slip faults are chosen. Fault planes can be expressed with strike, dip and rake (slip) angles. In a source medium with different anisotropy classes, isotropic, transversely isotropic, orthotropic and monoclinic are used. Elasticity tensors are calculated for several minerals, rocks and sub surfaces of earth. Effects of anisotropy types and their rotations on moment tensors are found for each fault type. Moment tensors are decomposed by using the Knopoff [3] and Fitch [5] decomposition method. Percentages of DC, CLVD and ISO on moment tensors are found. In order to explain the effect of anisotropy, fault plane angles are recalculated by using DC part of moment tensors.

Then, closest isotropic elasticity tensors that represent rotated anisotropic elasticity tensors are found. Strike, dip and rake angles are recalculated. The purpose of this process is to determine the difference between the true values of fault plane angles.

In chapter 2, physical meaning of the fault plane angles is mentioned briefly. Five fundamental fault types and four anisotropic elasticity tensors that are used in this thesis is explained. Moment tensor and earthquake source properties are also explained. Moment density tensor in both isotropic and anisotropic medium is expressed. Definition of elasticity tensor and its properties are explained. Rotation of elasticity tensor and its mathematical and geometrical meanings are mentioned. Determining of a closest isotropic elasticity tensor of a given anisotropic elasticity tensor is mentioned briefly. Mathematical process of moment tensor evaluation and decomposition are explained. Demonstration of fault plane and normal plane as a vector can also be found in chapter 2. Geometrical meaning of moment tensor is mentioned. Recalculation of fault plane parameters is also explained in this chapter. In chapter 3, results of moment tensor decomposition can be found. Variation of fault plane angles for given elasticity tensor and its rotations is explained. These explanations are also made for closest isotropic elasticity tensor assumptions. Results are interpreted in chapter 4. Materials with symmetry group of transversely isotropy are discussed with each other and the results of Vavryčuk [9]. Decomposition results of materials with orthotropic and monoclinic symmetry classes are discussed with their materials with their own symmetry class. Effects of fault plane orientation are mentioned in this chapter. Distance from isotropic space of given anisotropic material is correlated with P and S wave anisotropy percentages which are calculated by using MTEX software. In last chapter, chapter 5, the physical meaning of these results are interpreted.

2. DATA AND METHOD

In this chapter, physical and mathematical definition of fault planes, moment tensors, elasticity tensors, rotation matrices, process of defining closest isotropic elasticity tensor of given anisotropic elasticity tensor, moment tensor decomposition are expressed. Elasticity tensors that used in the thesis are also given in this chapter.

2.1. Fault Plane Parameters

A fault is a planar fracture or discontinuity in a volume of rock, across which there has been significant displacement as a result of rock mass movement. A fault plane is the plane that represents the fracture surface of a fault. One can define the orientation of fault plane on Cartesian coordinates such that strike (Φ), dip (δ) and slip (λ). These parameters can be expressed by slip vector ($\mathbf{u}$) and fault normal ($\mathbf{v}$) which are vital on moment tensors. Φ is measured clockwise from north with the fault plane dipping to the right when looking along the strike direction, δ; measures the deviation from horizontal down and λ the slip direction measured in the fault plane (Figure 2.1). Angles of these parameters can vary between $0 \leq \Phi \leq 2\pi$,$0 \leq \delta \leq \frac{\pi}{2}$ and $-\pi \leq \lambda \leq \pi$ [1,32].

If Φ, δ and λ are known, $\mathbf{u}$ and $\mathbf{v}$ can be calculated by Aki [1] as,

$$\begin{aligned} \mathbf{u} = &\overline{u}(\cos\lambda + \cos\Phi + \cos\delta\sin\lambda\sin\Phi)\mathbf{e}_x \\ &+\overline{u}(\cos\lambda + \sin\Phi - \cos\delta\sin\lambda\cos\Phi)\mathbf{e}_y \\ &-\overline{u}(\sin\delta\sin\lambda)\mathbf{e}_z \end{aligned} \tag{2.1}$$

$$\mathbf{v} = -\sin\delta\sin\Phi\mathbf{e}_x + \sin\delta\cos\Phi\mathbf{e}_y - \cos\delta\mathbf{e}_z \tag{2.2}$$

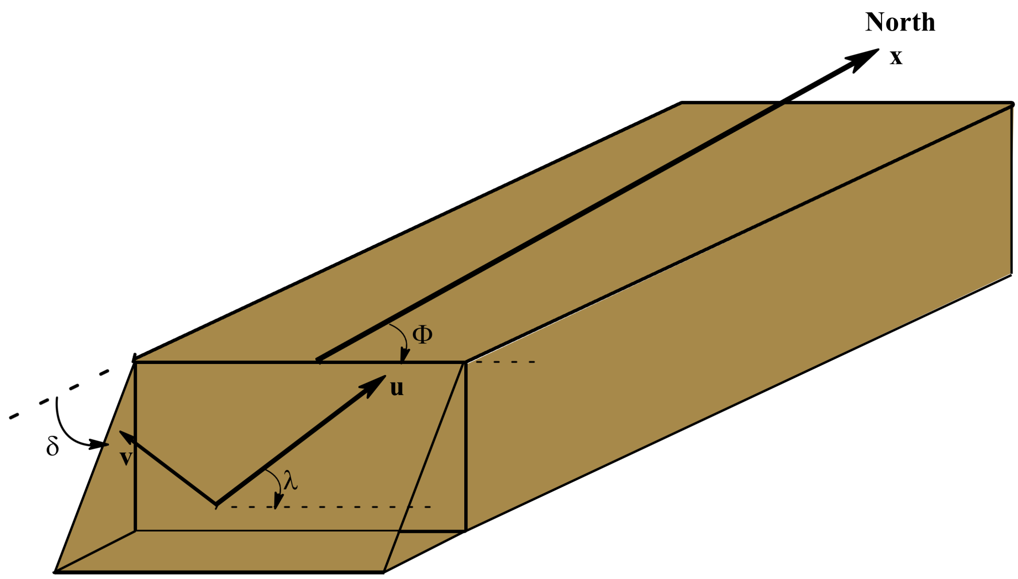

Figure 2.1. Fault Plane Representation in Cartesian Coordinates

$\bar{u}$ is the mean displacement on the fault plane. $\bar{u}$ has a vital role on determining scalar seismic moment M_0 which is an important parameter for moment magnitude (M_w) calculations.

2.2. Elasticity Tensor

Elasticity means the ability of a material to recover its original dimensions, and to return its original shape, after being subjected to a stress. Hooke's Law explain the mechanisms of this process. If the amount of stress σ is infinitesimally small then the amount of strain ε, which is also infinitesimal, is linearly proportional to the strain and can be written as:

$$\sigma_{ij} = c_{ijkl}\varepsilon_{kl} \tag{2.3}$$

where c_{ijkl} is forth rank elasticity tensor, σ_{ij} and ε_{kl} are second rank tensors.

2.3. Orthogonal Transformations

Let $\mathbf{e}_1$, $\mathbf{e}_2$ and $\mathbf{e}_3$ be the unit vectors of x,y and z axis, respectively. In this system,

$$e_1 = (1,0,0),$$
$$e_2 = (0,1,0),$$
$$e_3 = (0,0,1).$$

Let σ be a linear transformation that maps $\mathbf{a}$ to $\mathbf{b}$;

$$\mathbf{b} = \sigma(\mathbf{a}) = a_1\sigma(\mathbf{e}_1) + a_2\sigma(\mathbf{e}_2) + a_3\sigma(\mathbf{e}_3) \tag{2.4}$$
$$b_i = a_j e_i \cdot \sigma_{ij}(e_j) \tag{2.5}$$

σ in $e_i \cdot \sigma(e_j)$ can be written as a tensor form,

$$\sigma_{ij} = e_i \cdot \sigma(\mathbf{e}_j) \tag{2.6}$$

Then we can rewrite the Equation 2.5 as,

$$b_i = \sigma_{ij} a_j \tag{2.7}$$

These equations can be written as matrix form,

$$\begin{bmatrix} b_1 \\ b_2 \\ b_3 \end{bmatrix} = \begin{bmatrix} \sigma_{11} & \sigma_{12} & \sigma_{13} \\ \sigma_{21} & \sigma_{22} & \sigma_{23} \\ \sigma_{31} & \sigma_{32} & \sigma_{33} \end{bmatrix} = \begin{bmatrix} a_1 \\ a_2 \\ a_3 \end{bmatrix} \tag{2.8}$$

σ matrix is called matrix of the linear transformation or the the tensor σ with respect to the orthogonal coordinate system $\{e_1, e_2, e_3\}$
A tensor has infinitely many matrix representations since it can be represented in any coordinate system. If $\{e_1, e_2, e_3\}$ and $\{e_1^{'}, e_2^{'}, e_3^{'}\}$ are two different bases, then we denote the components of tensor σ by σ_{ij} and $\sigma_{ij}^{'}$ for each of the basis vectors, respectively. The entries of σ in the $\{e_1^{'}, e_2^{'}, e_3^{'}\}$ basis can be evaluated, similar to Equation 2.6, as $\sigma_{ij}^{'} = e_i^{'} \cdot \sigma^{'}(\mathbf{e}_j)$.

This gives $\{e_1^{'}, e_2^{'}, e_3^{'}\}$ and $\{e_1, e_2, e_3\}$ are related with an orthogonal transformation tensor, A. In other words, $\{e_1^{'}, e_2^{'}, e_3^{'}\}$ can be obtained by applying an orthogonal transformation to $\{e_1, e_2, e_3\}$.

$$\mathbf{e}_i^{'} = A(\mathbf{e})_i = A_{mi}\mathbf{e}_m \tag{2.9}$$

Components of A can be obtained by using Equation 2.9 and it would be like below,

$$A_{mi} = \mathbf{e}_m \cdot A(\mathbf{e}_i) = \mathbf{e}_m \cdot \mathbf{e}_i^{'} \tag{2.10}$$

Euler's rotation theorem states that a rotation matrix can be decomposed as a product of three elementary rotations. By using this theorem, we can find a rotation matrix that transform $\{e_1, e_2, e_3\}$ coordinate system to $\{e_1^{'}, e_2^{'}, e_3^{'}\}$ coordinate system.

Now let's consider a linear transformation σ. The components of σ with respect to $\{e_1, e_2, e_3\}$ and $\{e_1^{'}, e_2^{'}, e_3^{'}\}$ are $\sigma_{ij} = \mathbf{e}_i \cdot \sigma(\mathbf{e}_j)$ and $\sigma_{ij}^{'} = \mathbf{e}_j^{'} \cdot \sigma(\mathbf{e}_j^{'})$, respectively.
Since

$$\begin{aligned} \sigma_{ij}^{'} &= \mathbf{e}_j^{'} \cdot \sigma(\mathbf{e}_j^{'}) \\ &= A_{im}\mathbf{e}_m \cdot \sigma(A_{nj}\mathbf{e}_n) \\ &= A_{mi}A_{nj}(\mathbf{e}_m \cdot \sigma(\mathbf{e}_n)), \end{aligned} \tag{2.11}$$

we obtain

$$\sigma_{ij}^{'} = A_{mi}A_{nj}\sigma_{mn}. \tag{2.12}$$

This can be written in matrix form as,

$$\begin{bmatrix} \sigma_{11}^{'} & \sigma_{12}^{'} & \sigma_{13}^{'} \\ \sigma_{21}^{'} & \sigma_{22}^{'} & \sigma_{23}^{'} \\ \sigma_{31}^{'} & \sigma_{32}^{'} & \sigma_{33}^{'} \end{bmatrix} = \begin{bmatrix} A_{11} & A_{21} & A_{31} \\ A_{12} & A_{22} & A_{32} \\ A_{13} & A_{23} & A_{33} \end{bmatrix} \begin{bmatrix} \sigma_{11} & \sigma_{12} & \sigma_{13} \\ \sigma_{21} & \sigma_{22} & \sigma_{23} \\ \sigma_{31} & \sigma_{32} & \sigma_{33} \end{bmatrix} \begin{bmatrix} A_{11} & A_{12} & A_{13} \\ A_{21} & A_{22} & A_{23} \\ A_{31} & A_{32} & A_{33} \end{bmatrix} \tag{2.13}$$

in short,

$$\sigma^{'} = A^T \sigma A \tag{2.14}$$

We can use this method to change the coordinate system of elasticity tensor which is a forth rank tensor. The transformation can be shown as below,

$$c'_{ijkl} = A_{pi}A_{qj}A_{rk}A_{si}c_{pqrs}, \tag{2.15}$$

elasticity tensor expressed in $\{e_1, e_2, e_3\}$ coordinate system. Here in, c' is expressed in the rotated coordinate system, namely $\{A(\mathbf{e}_1), A(\mathbf{e}_2), A(\mathbf{e}_3)\}$.

2.4. Rotation of an Elasticity Tensor

In this chapter we will explain how to evaluate matrix A that we express in section 2.3. Elasticity tensor can be represent in $\{e_1, e_2, e_3\}$. However, in the nature Earth's material can be rotated by many reasons, such as the forces that moves the plates. This rotation may have no affects on isotropic elasticity tensor whereas other types of elasticity tensors may get affected by in the end of this process. Rotation process can be done by using three rotation matrices which transform $\{e_1, e_2, e_3\}$ to $\{e'_1, e'_2, e'_3\}$. According to Euler's theorem, any rotation matrix can be archived by multiplication of three elementary rotations; Z_1, Z_2 and Z_3.

To obtain e'_3 one applies a rotation around the e_3 axis. This can be done by Z_1 and Z_2

$$Z_1 = \begin{bmatrix} cos\psi & -sin\psi & 0 \\ sin\psi & cos\psi & 0 \\ 0 & 0 & 1 \end{bmatrix} \tag{2.16}$$

Then, rotation around e_1 is done by Z_2

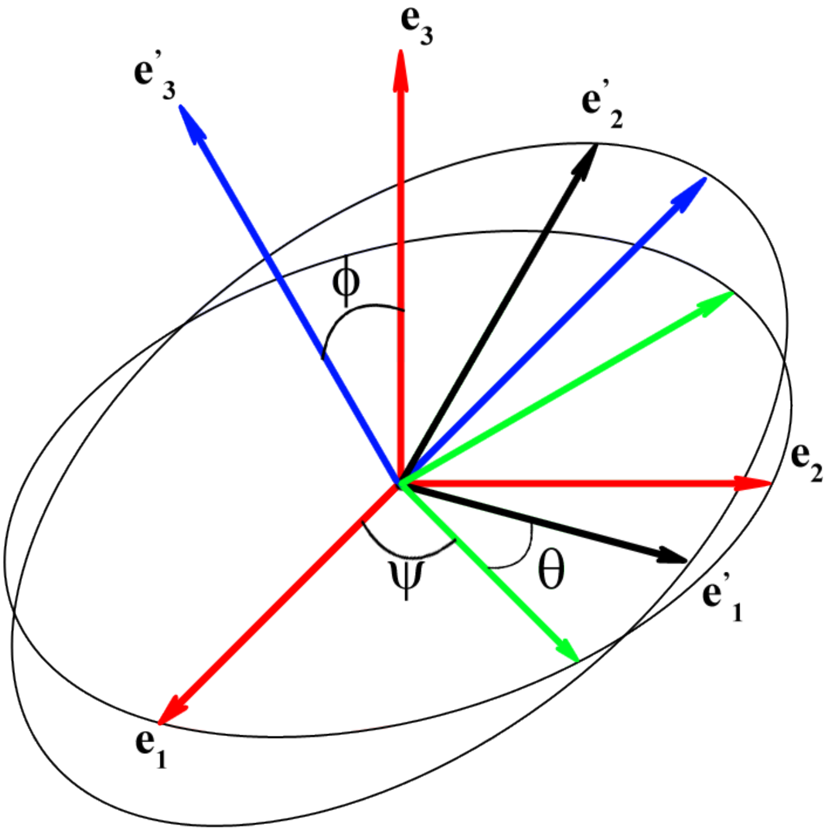

Figure 2.2. Graphical representation of elementary transformations by using rotation matrices. $\{e_1, e_2, e_3\}$ coordinate system transformed to $\{e_1^{'}, e_2^{'}, e_3^{'}\}$ by using ψ, ϕ and θ.

$$Z_2 = \begin{bmatrix} 1 & 0 & 0 \\ 0 & cos\phi & -sin\phi \\ 0 & sin\phi & cos\phi \end{bmatrix} \tag{2.17}$$

In order to rotate e_1 and e_2 to $e_1^{'}$ and $e_2^{'}$ one must use Z_3 rotation matrix around $e_3^{'}$ axis

$$Z_3 = \begin{bmatrix} cos\theta & -sin\theta & 0 \\ sin\theta & cos\theta & 0 \\ 0 & 0 & 1 \end{bmatrix} \tag{2.18}$$

$\{e_1, e_2, e_3\}$, $\{e_1^{'}, e_2^{'}, e_3^{'}\}$, Euler's angles ψ, ϕ and θ can be seen in Figure 2.2.

Thus $A = Z_1 Z_2 Z_3$ rotates to basis vector $\{e_1, e_2, e_3\}$ to $\{e_1^{'}, e_2^{'}, e_3^{'}\}$.

Matrix A is 3 x 3 matrix however elasticity tensor **C** is a 6 x 6 matrix. In order to overcome this problem **C** must be written in Kelvin notation and transformation matrix A must be written as below,

$$\overline{A} = \begin{bmatrix} A_{11}A_{11} & A_{12}A_{12} & A_{13}A_{13} & \sqrt{2}A_{12}A_{13} & \sqrt{2}A_{11}A_{13} & \sqrt{2}A_{11}A_{12} \\ A_{21}A_{21} & A_{22}A_{22} & A_{23}A_{23} & \sqrt{2}A_{22}A_{23} & \sqrt{2}A_{21}A_{23} & \sqrt{2}A_{21}A_{22} \\ A_{31}A_{31} & A_{32}A_{32} & A_{33}A_{33} & \sqrt{2}A_{32}A_{33} & \sqrt{2}A_{31}A_{33} & \sqrt{2}A_{31}A_{32} \\ \sqrt{2}A_{21}A_{31} & \sqrt{2}A_{22}A_{32} & \sqrt{2}A_{23}A_{33} & A_{22}A_{33}+A_{23}A_{32} & A_{21}A_{33}+A_{23}A_{31} & A_{21}A_{32}+A_{22}A_{31} \\ \sqrt{2}A_{11}A_{31} & \sqrt{2}A_{12}A_{32} & \sqrt{2}A_{13}A_{33} & A_{12}A_{33}+A_{13}A_{32} & A_{11}A_{33}+A_{13}A_{31} & A_{11}A_{32}+A_{12}A_{31} \\ \sqrt{2}A_{11}A_{21} & \sqrt{2}A_{12}A_{22} & \sqrt{2}A_{13}A_{23} & A_{12}A_{23}+A_{13}A_{22} & A_{11}A_{23}+A_{13}A_{21} & A_{11}A_{22}+A_{12}A_{21} \end{bmatrix}. \tag{2.19}$$

2.5. Anisotropy Classes

There are eight type of symmetry classes of a material [33]. There is a subgroup relation between classes which can be seen in Figure 2.3. Anisotropy classes are; generally anisotropy, monoclinic, orthotropic, tetragonal, transversely isotropic (TI), trigonal, cubic and isotropic which can be seen in Figure 2.3. In this chapter, properties of these classes are explained. TI, orthotropic and monoclinic elasticity tensors are chosen for the numerical applications. All elasticity tensors are given by using Voigt notation.

2.5.1. Transversely Isotropic

Assuming natural coordinate system is represented as $\{e_1, e_2, e_3\}$, then the orientation of e_1 and e_2 do not matter if e_3 is parallel to the axis rotation. The matrix representation of transversely isotropic symmetry in matrix form is shown below,

$$C^{TI} = \begin{bmatrix} C_{11} & C_{12} & C_{13} & 0 & 0 & 0 \\ C_{12} & C_{11} & C_{13} & 0 & 0 & 0 \\ C_{13} & C_{13} & C_{33} & 0 & 0 & 0 \\ 0 & 0 & 0 & C_{44} & 0 & 0 \\ 0 & 0 & 0 & 0 & C_{44} & 0 \\ 0 & 0 & 0 & 0 & 0 & \dfrac{C_{11}-C_{12}}{2} \end{bmatrix}.$$

Note that five parameters, namely C_{11}, C_{12}, C_{13}, C_{33} and C_{44} are enough to describe TI. TI corresponds to a planar structures layering in sediments or fractures persistent of layers along parallel directions.

2.5.2. Orthotropic

Orthotopic symmetry class has three orthogonal symmetry planes. If any two mirror planes orthogonal to each other, then the third plane is perpendicular to first two planes. In natural basis, orthotropic elasticity tensor can be shown as a matrix form:

$$C^{ORTHOTROPIC} = \begin{bmatrix} C_{11} & C_{12} & C_{13} & 0 & 0 & 0 \\ C_{12} & C_{22} & C_{23} & 0 & 0 & 0 \\ C_{13} & C_{23} & C_{33} & 0 & 0 & 0 \\ 0 & 0 & 0 & C_{44} & 0 & 0 \\ 0 & 0 & 0 & 0 & C_{55} & 0 \\ 0 & 0 & 0 & 0 & 0 & C_{66} \end{bmatrix}.$$

If there are two planar structures which are perpendicular to each other than orthotropic symmetry class can explain this symmetry class.

2.5.3. Monoclinic

Monoclinic symmetry class contains a reflection about a plane through the origin. Let say a coordinate system such that reflection take place at e_1e_2 plane, which means along the e_3. In such system monoclinic elasticity tensor can be written as below,

$$C^{MONOCLINIC} = \begin{bmatrix} C_{11} & C_{12} & C_{13} & 0 & 0 & C_{16} \\ C_{12} & C_{22} & C_{23} & 0 & 0 & C_{26} \\ C_{13} & C_{23} & C_{33} & 0 & 0 & C_{36} \\ 0 & 0 & 0 & C_{44} & C_{45} & 0 \\ 0 & 0 & 0 & C_{45} & C_{55} & 0 \\ C_{16} & C_{26} & C_{36} & 0 & 0 & C_{66} \end{bmatrix}.$$

Two planar structures have oblique angle relation with each other.

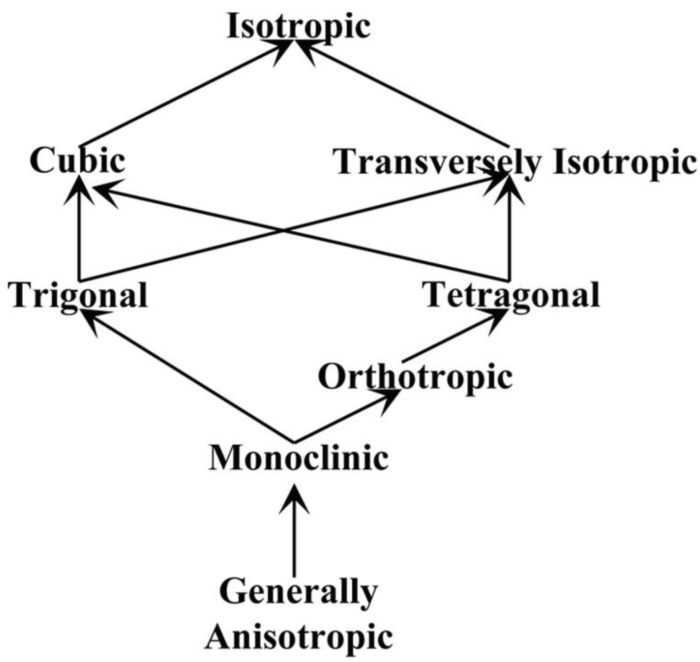

Figure 2.3. Orders of eight rotation classes. Arrows indicates subgroup relations. For instance; Orthotropic is a subgroup of Tetragonal. Symmetry classes rather than TI, Monoclinic and orthotropic are explained in Appendix C

2.6. Moment Tensor

Moment tensor can be defined as equivalent body forces of seismic sources (Figure 2.4). Moment Tensor, denoted by **M**, depends on source strength and fault orientation. Number of studies state that seismic sources can generate non-DC components [31]. An explosion, for instance, can generate non-DC components. Collapse of cavity in mines, shear faulting on a non-planar fault, fluid injection in geothermal or volcanic areas or seismic anisotropy in focal area can also generate non-DC components [6, 8–10, 19, 20, 29, 34–36].

In order to define these forces, first we need to explain moment density function, **m**. By using representation theorem displacement can be calculated as below,

$$u_n(x,t) = \iint_{\Sigma} [u_i]\nu_j c_{ijpq} * \frac{\partial G_{np}}{\partial \xi_q} d\Sigma \tag{2.20}$$

Notice that $*$ is convolution symbol.

Displacement at a point which is created by a point source can be found by $F_p * G_{np}$ under the assumption of force is applied at ξ is $F(\xi,\tau)$. Convolving with Green's function's derivative indicates a force couple. Sum over q means that each displacement component at x is equivalent to the effect of a sum of couples distributed over Σ. For displacement discontinuities as in the formula above, there are instead derivatives of G_{np} with respect to the source coordinates ξ_q. This derivative can be thought of physically as the equivalent of having a single couple with arm in the ξ_q direction on Σ at ξ.

Since $[u_i]v_j c_{ijpq} * \frac{\partial G_{np}}{\partial \xi_q}$ in the formula is the n-component of the field at x due to couples at ξ, it follows that $[u_i]v_j c_{ijpq}$ is the strength of the (p,q) couple. We define

$$m_{pq} = [u_i]v_j c_{ijpq} \tag{2.21}$$

to be the components of moment density function $\mathbf{m}$.

For three components of force and three arm directions, there are nine generalized couples, as shown in Figure 2.4. Thus equivalent surface force corresponding to an an infinitely small surface element $d\Sigma(\xi)$ can be represented as a combination of nine couples.
The representation theorem for displacement at x due to general displacement discontinuity $[\mathbf{u}(\xi,\tau)]$ across Σ can be written by using the moment tensor as

$$u_n(x,t) = \iint_{\Sigma} m_{pq} * G_{np,q} \, d\Sigma \tag{2.22}$$

If x is many wavelengths away from ξ and if the wavelengths of the observations are larger than the source dimensions, then convolution with $\mathbf{G}$ gives the displacement at (x,t) that depends on what occurs at ξ only at retarded time. This is called point source approximation. This can be written as $r\lambda_{wl} \gg L^2$ where r is the distance of the observation point from the source, λ_{wl} is wavelength and L is dimensions of source [37].

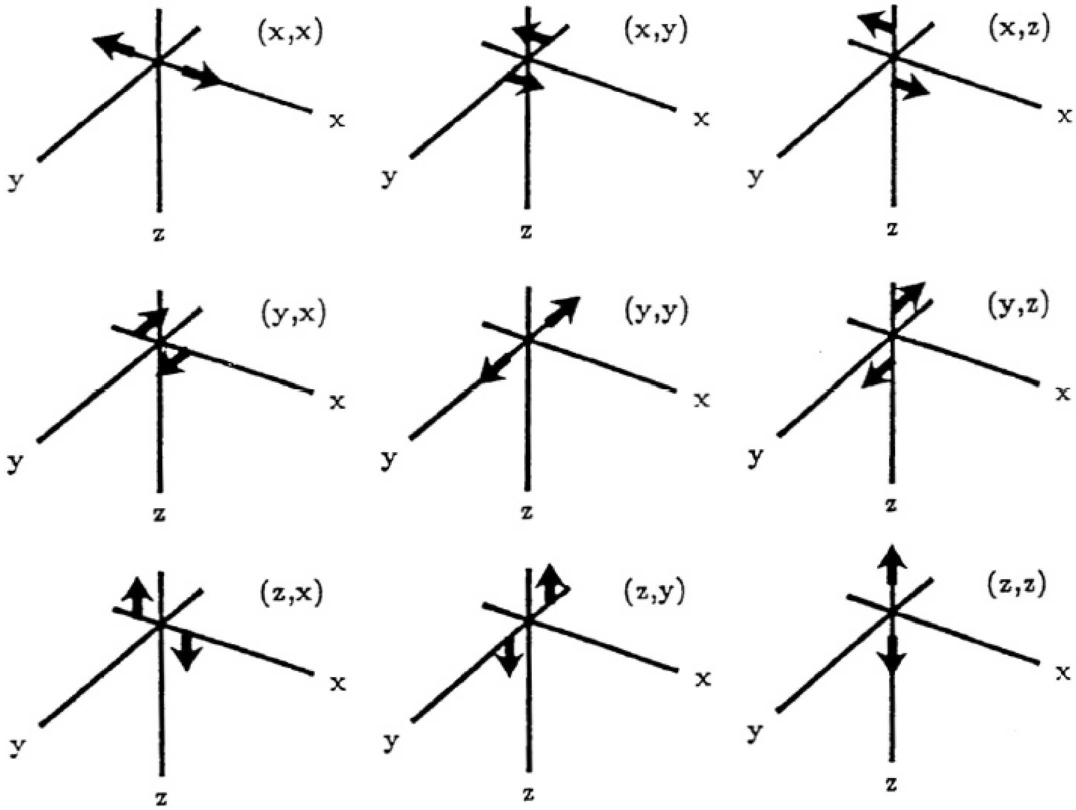

Figure 2.4. The nine generalized couples [1]

This results are for fault plane with finite extent. However, in practice seismographs can only good at certain periods for which the whole of Σ is a point source. In such situation whole surface, Σ, can be thought as a point, center of Σ, with moment tensor equal to the integral of moment density over Σ. Thus, for an effective point source,

$$u_n(x,t) = M_{pq} * G_{np,q} \tag{2.23}$$

where the moment tensor components are

$$\begin{aligned} M_{pq} &= \iint_{\Sigma} m_{pq}\, d\Sigma = \iint_{\Sigma} [u_i] v_j C_{ijpq}\, d\Sigma \\ &= \iint_{\Sigma} \mu(v_p[u_q] + v_q[u_p]) \end{aligned} \tag{2.24}$$

Theorem

It's known that moment density tensor in anisotropic medium is given as

$$m_{pq} = [u_i]v_j c_{ijpq} \tag{2.25}$$

For an isotropic medium, above expression can be written as $M_{pq} = \mu A([u_p]v_q + [u_q]v_p)$

Proof

For an isotropic body,

$$m_{pq} = \lambda_{em} v_k [u_k] \delta_{pq} + \mu(v_p[u_q] + v_q[u_p]) \tag{2.26}$$

If the displacement discontinuity (or slip) is parallel to Σ at ξ, the scalar product $\mathbf{v} \cdot \mathbf{u}$ is zero and

$$m_{pq} = \mu(v_p[u_q] + v_q[u_p]) \tag{2.27}$$

First, we will show the form of the isotropic elasticity tensor and elasticity matrix. Then substitute the elasticity tensor into the moment density tensor $m_{pq} = [u_i]v_j c_{ijpq}$.

$$\begin{aligned} m_{pq} &= [u_i]v_j c_{ijpq} \\ &= \lambda_{em}\delta_{ij}[u_i]v_j\delta_{pq} + \mu\delta_{ip}\delta_{jq}[u_i]v_j + \mu\delta_{iq}\delta_{jp}[u_i]v_j \\ &= \lambda_{em}[u_k]v_k + \mu(u_p v_q + u_q v_p) \end{aligned} \tag{2.28}$$

For isotropic medium, 21 parameters of elasticity tensor reduces to 2 parameters:

$$\begin{bmatrix} C_{11} & C_{12} & C_{13} & C_{14} & C_{15} & C_{16} \\ * & C_{22} & C_{23} & C_{24} & C_{25} & C_{26} \\ * & * & C_{33} & C_{34} & C_{35} & C_{36} \\ * & * & * & C_{44} & C_{45} & C_{46} \\ * & * & * & * & C_{55} & C_{56} \\ * & * & * & * & * & C_{66} \end{bmatrix} = \begin{bmatrix} \lambda_{em}+2\mu & \lambda_{em} & \lambda & 0 & 0 & 0 \\ \lambda_{em} & \lambda_{em}+2\mu & \lambda_{em} & 0 & 0 & 0 \\ \lambda_{em} & \lambda_{em} & \lambda_{em}+2\mu & 0 & 0 & 0 \\ 0 & 0 & 0 & \mu & 0 & 0 \\ 0 & 0 & 0 & 0 & \mu & 0 \\ 0 & 0 & 0 & 0 & 0 & \mu \end{bmatrix} \tag{2.29}$$

λ_{em} and μ are called Lame parameters. These are the only parameters for isotropic medium.

We can observe that the isotropic elasticity matrix defined in Equation 2.29 can be written in tensor form as,

$$c_{ijpq} = \lambda_{em}\delta_{ij}\delta_{pq} + \mu(\delta_{ip}\delta_{jq} + \delta_{iq}\delta_{jp}) \tag{2.30}$$

Equation 2.28 can also be demonstrated as,

$$m_{pq} = \lambda_{em}v_k[u_k]\delta_{pq} + \mu(v_p[u_q] + v_q[u_p]) \tag{2.31}$$

Assuming that the slip is parallel to Σ, $v.[\mathbf{u}] = v_k u_k = 0$, Equation 2.31 reduces to,

$$m_{pq} = \mu(v_p[u_q] + v_q[u_p]) \tag{2.32}$$

The relation between the moment density tensor and moment tensor in isotropic medium is given as Equation 2.33.

$$\begin{aligned} M_{pq} &= \iint_{\Sigma} m_{pq}\, d\Sigma = \iint_{\Sigma} [u_i] v_j C_{ijpq}\, d\Sigma \\ &= \iint_{\Sigma} \mu(v_p[u_q] + v_q[u_p]) \end{aligned} \tag{2.33}$$

Assuming that the earthquake acts a point source $[u_p]$,v_q and μ are constant throughout Σ. Since we assume the source as a point $\iint_{\Sigma} d\Sigma = A$. Then we can take these expressions out of the integral and obtain,

$$M_{pq} = \mu A([u_p]v_q + [u_q]v_p) \tag{2.34}$$

We note that the roles of the vectors **u** and **v** could be interchanged without any affecting the displacement filed. This causes the well known fault plane - auxiliary plane ambiguity.

2.7. Eigenvalues of Moment Tensor

The expression $M_{pq} = \mu A(u_p v_q + u_q v_p)$ is a second tensor, describing a double couple. This tensor is real and symmetric, giving real eigenvalues and orthogonal eigenvectors. The eigenvalues are proportional to (1,0,-1). The characteristic properties of a moment tensor representing a double couple are

i) one eigenvalue of the moment tensor vanishes

ii)the sum of the eigenvalues vanishes, i.e. trace=0

Theorem : t, b and p are eigenvectors of M_{pq} which are corresponding eigenvalues are positive, 0 and negative, respectively.

Proof

Eigenvectors of M_{pq} are **t**, **b** and **p**:

$$\begin{aligned}
\mathbf{t} &= \frac{1}{\sqrt{2}}(\mathbf{v}+\mathbf{u}) \\
\mathbf{b} &= \mathbf{v}\times\mathbf{u} \\
\mathbf{p} &= \frac{1}{\sqrt{2}}(\mathbf{v}-\mathbf{u}),
\end{aligned} \tag{2.35}$$

where **v** and **u** are taken to be unit vectors.

The eigenvectors **t**, **b** and **p** represents positive, zero and negative eigenvalues, respectively.

In order to show that **t** is an eigenvector of M_{pq}, it should satisfy the equation $M_{pq}t_j = \lambda t_k$:

$$\begin{aligned}
M_{pq}(v_q+u_q) &= (u_p v_q + u_q v_p)(v_q+u_q) \\
&= u_p v_q v_q + u_q v_k v_q + u_p v_q u_q + u_q v_p u_q \\
&= |\vec{v}|^2 u_p + |\vec{u}|^2 v_p
\end{aligned} \tag{2.36}$$

since $\bar{u}$ and $\bar{v}$ are perpendicular, $u_q v_q = 0$

$$M_{pq}(v_q + u_q) = u_p + v_p \tag{2.37}$$

since $\bar{u}$ and $\bar{v}$ are unit vectors.

$$|\vec{v}| = v_q v_q \bar{u} = \frac{\vec{u}}{|u|} \tag{2.38}$$

where $\bar{u}$ is a unit vector in the direction of $\vec{u}$ Similarly we can show that **b** and **p** are eigenvectors of M_{pq}:

$$\begin{aligned} M_{pq}(v_q - u_q) &= (u_p v_q + u_q v_p)(v_q - u_q) \\ &= u_p v_q v_q + u_q v_p v_q - u_p v_q u_q - u_q v_p u_q \\ &= |\vec{v}|^2 u_p - |\vec{u}|^2 v_p \end{aligned} \tag{2.39}$$

since **u** and **v** are perpendicular, $u_q v_q = 0$

$$M_{pq}(v_q - u_q) = u_p + v_p \tag{2.40}$$

$$
\begin{aligned}
M_{pq}(v \times u)_q &= (u_p v_q + u_q v_p)(v \times u)_q \\
&= u_p v_q (v \times u)_q + u_q v_p (v \times u)_q \\
&= 0
\end{aligned}
\tag{2.41}
$$

since $\mathbf{v}$ is perpendicular to $\mathbf{v} \times \mathbf{u}$ and $\mathbf{u}$ is perpendicular to $v \times u$.

Thus we obtain that eigenvalues of M_{pq} are 0,1 and -1. Thus trace of $\mathbf{u}$ and $\mathbf{v}$ are unit vectors of shear faulting.

The double couple $u_p v_q + u_q v_p$ can equivalently be described by its eigenvectors [38].

$$
\begin{gathered}
u_p v_q + u_q v_p = t_p t_q - p_p p_q \\
0.5[(t_p + p_p)(t_q - p_q) + (t_p - p_p)(t_q + p_q)]
\end{gathered}
\tag{2.42}
$$

Comparing these terms, we can find the relation between slip vector and fault normal:

$$
\begin{aligned}
\mathbf{u} &= \frac{1}{\sqrt{2}}(\mathbf{t} + \mathbf{p}) \\
\mathbf{v} &= \frac{1}{\sqrt{2}}(\mathbf{t} - \mathbf{p})
\end{aligned}
\tag{2.43}
$$

The other nodal plane is defined by

$$
\begin{aligned}
\mathbf{u} &= \frac{1}{\sqrt{2}}(\mathbf{t} - \mathbf{p}) \\
\mathbf{v} &= \frac{1}{\sqrt{2}}(\mathbf{t} + \mathbf{p})
\end{aligned}
\tag{2.44}
$$

2.8. Moment Tensor of Shear Faulting for Different Anisotropy Classes With Varying Orientations

In Chapter 2.1 we explain fault plane parameters and how to obtain **u** and **v** vectors. Then the definition of elasticity tensor and its rotations explained in Chapter 2.2, 2.3 and 2.4. And then we mentioned the anisotropic elasticity tensors in Chapter 2.5. Finally we explain mathematical properties of moment tensor. Now we continue on generating moment tensors by using anisotropic elasticity tensor and **u** and **v** vectors of fault plane parameters.

Moment tensor, **m**, can be generated by multiplying elasticity tensor, **C**, and fault vector **d**. Fault vector has information about fault plane parameters which are **u** and **v** [1].

$$m_{pq} = DSC_{qpkl}v_k u_l \tag{2.45}$$

D and S represents fault slip (cm) and fault area (km^2), respectively. Fault vector **d** can be written as Equation 2.46,

$$\mathbf{d} = DS(u_1v_1, u_2v_2, u_3v_3, u_2v_3 + u_3v_2, u_1v_3 + u_3v_1, u_1v_2 + u_2v_1)^T \tag{2.46}$$

In Equation 2.46 **u** and **v** is selected as unit, 1.

In this thesis, all vectors are expressed in the natural coordinate system of TI elasticity tensor; that is, the z-axis is along the direction of infinite-fold rotation axis. Elasticity tensor is rotated by rotation matrix A which is explained in Chapter 2.3 and Chapter 2.4. Elasticity tensors are rotated by using Equation 2.47,

$$C' = \overline{A}^T C \overline{A} \tag{2.47}$$

.

Generation of moment tensors are done as below,

i. We choose one fault type use specific **d** of it.
ii. Then we take anisotropic elasticity tensor and rotated it by using Euler's angles which is explained in Equation 2.47
iii. We multiply C' with **d** and get 1 x 6 vector **m** as a result.
iv. We obtain moment tensor **M**.
v. $\pm\%CLVD$ $\pm\%ISO$ are found by decomposing **M**. We also found fault plane parameters and slip vector by using DC component of **M**. These process can be found in Section 2.9.

Then we expressed **m** in matrix form as below,

$$\mathbf{M} = \begin{bmatrix} m_{11} & m_{12} & m_{13} \\ m_{12} & m_{22} & m_{23} \\ m_{13} & m_{23} & m_{33} \end{bmatrix} \tag{2.48}$$

2.9. Moment Tensor Decomposition

There are several methods for decomposing moment tensors (**M**) [3–10, 39] . Decomposition methods are developed in order to obtain physical properties of faults. In this thesis, we used Double Couple-CLVD decomposition method which is proposed by Knopoff [3] and Fitch [5]. Moment tensor is decomposed into isotropic (ISO), double couple and compensated linear vector dipole (CLVD) parts.

Before applying decomposition methods **M** must be diagonalized. To do so **M** is expressed according to the basis which are orthonormal eigenvectors of **M**. Let m_i be the eigenvalue corresponding to the orthonormal eigenvector $\mathbf{a}_i = (a_{ix}, a_{iy}, a_{iz})^T$. We can write **M** as:

$$\begin{aligned} M &= \begin{bmatrix} a_1 & a_2 & a_3 \end{bmatrix} \mathbf{m} \begin{bmatrix} a_1^T \\ a_2^T \\ a_3^T \end{bmatrix} \\ &= \begin{bmatrix} a_{1x} & a_{2x} & a_{3x} \\ a_{1y} & a_{2y} & a_{3y} \\ a_{1z} & a_{2z} & a_{3z} \end{bmatrix} \begin{bmatrix} m_1 & 0 & 0 \\ 0 & m_2 & 0 \\ 0 & 0 & m_3 \end{bmatrix} \begin{bmatrix} a_{1x} & a_{1y} & a_{1z} \\ a_{2x} & a_{2y} & a_{2z} \\ a_{3x} & a_{3y} & a_{3z} \end{bmatrix} \end{aligned} \tag{2.49}$$

m is the diagonalized moment tensor. m_3 corresponds the maximum and m_1 corresponds the minimum eigenvalue. The elements of **m** are the eigenvalues of **M**. Now we can apply decomposition method to **M**.

$$\begin{bmatrix} m_1 & 0 & 0 \\ 0 & m_2 & 0 \\ 0 & 0 & m_3 \end{bmatrix} = \frac{1}{3}\begin{bmatrix} tr(\mathbf{M}) & 0 & 0 \\ 0 & tr(\mathbf{M}) & 0 \\ 0 & 0 & tr(\mathbf{M}) \end{bmatrix} + \begin{bmatrix} m_1^* & 0 & 0 \\ 0 & m_2^* & 0 \\ 0 & 0 & m_3^* \end{bmatrix} \tag{2.50}$$

where $tr(\mathbf{M}) = m_1 + m_2 + m_3$ is the trace of the moment tensor. First term of Equation 2.50 is isotropic part of the moment tensor. Second term describes the deviatoric part of the moment tensor. Note that the decomposition is unique.

$$\begin{aligned} m_i^* &= m_i - \frac{m_1 + m_2 + m_3}{3} \\ &= m_i - \frac{1}{3} tr(\mathbf{M}) \end{aligned} \tag{2.51}$$

Now we will decompose deviatoric part into DC and CLVD components.

Assume that $\left|m_3^*\right| \geq \left|m_2^*\right| \geq \left|m_1^*\right|$. We can write deviatoric part as,

$$\begin{bmatrix} m_1^* & 0 & 0 \\ 0 & m_2^* & 0 \\ 0 & 0 & m_3^* \end{bmatrix} = m_3^* \begin{bmatrix} -\eta & 0 & 0 \\ 0 & \eta - 1 & 0 \\ 0 & 0 & 1 \end{bmatrix} \tag{2.52}$$

where $\eta = -m_1^* / \left|m_3^*\right|$ and $\eta - 1 = m_2^* / \left|m_3^*\right|$.The decomposition can be archived DC and CLVD components as,

$$m_3^* \begin{bmatrix} -\eta & 0 & 0 \\ 0 & \eta-1 & 0 \\ 0 & 0 & 1 \end{bmatrix} = m_3^*(1-2\eta) \begin{bmatrix} 0 & 0 & 0 \\ 0 & -1 & 0 \\ 0 & 0 & 1 \end{bmatrix} + m_3^*\eta \begin{bmatrix} -1 & 0 & 0 \\ 0 & -1 & 0 \\ 0 & 0 & 2 \end{bmatrix}. \tag{2.53}$$

Expressing **m** in its original coordinate system we obtain the decomposition of **M** as follows.

$$\begin{aligned} \mathbf{M} = & \frac{1}{3}(m_1+m_2+m_3)\mathbf{I} + m_3^*(1-2\eta)(a_3a_3 - a_2a_2) \\ & + m_3^*\eta(2a_3a_3 - a_2a_2 - a_1a_1) \end{aligned} \tag{2.54}$$

where **I** is 3 *x* 3 identity matrix. To estimate the deviation from seismic source of pure DC, one can use η [40],

$$\%ISO = \frac{1}{3}\frac{Tr(\mathbf{M})}{|m_3^*|} \cdot 100 \tag{2.55}$$

$$\%CLVD = 2\eta(100 - |ISO|) \tag{2.56}$$

$$\%DC = 100 - |ISO| - |CLVD|. \tag{2.57}$$

Percentages of non-DC components can be found by using Equation 2.55, 2.56 and 2.57. We found the non-DC percentages by using these formulas. Then we use the matrix which represents the DC component and then decompose it in order to recalculate fault plane parameters, Φ, δ and λ.

2.10. Physical Interpretation of Non-DC Components

There are two possible origins for CLVD and ISO components; volumetric changes in the source or anisotropy in the focal zone. ISO component can be explained by explosions and implosions whereas interpretation of CLVD component is not simple. Faulting on non planar fault or simultaneously activated neighboring faults can produce CLVD components [41,42]. Another origin of CLVD components is shear faulting in anisotropic media which is the main point of interest of this thesis [36,43]. Origin of CLVD source was invented by [3] in order to describe deep-focus earthquakes which causes phase changes in seismic records.

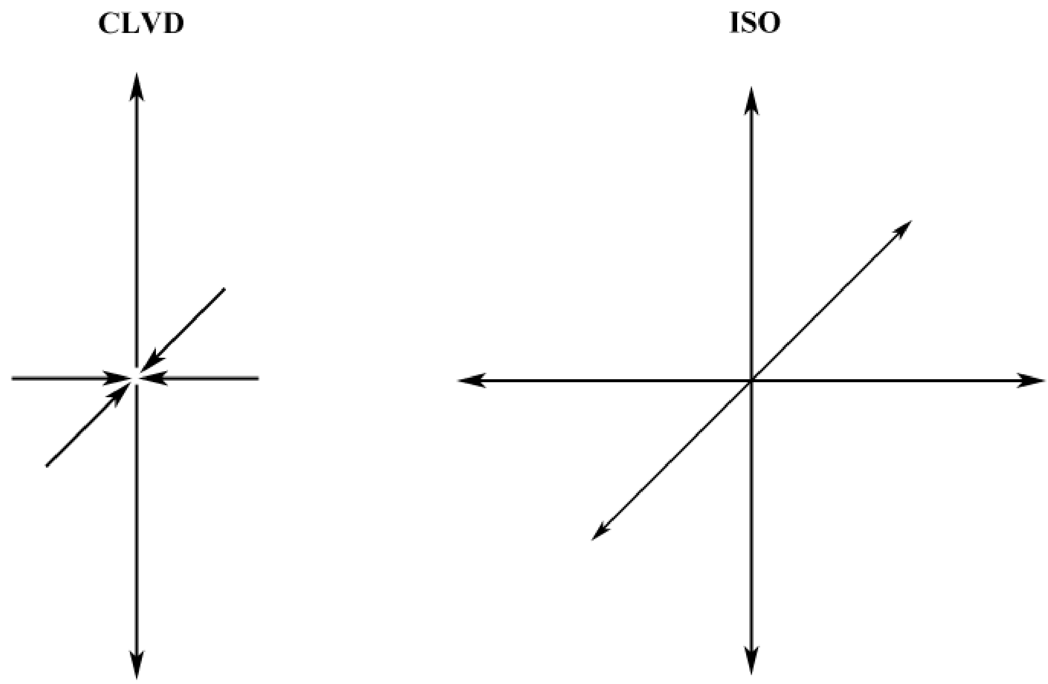

Figure 2.5. Body forces equivalents of ISO and CLVD components. In this figure both ISO and CLVD components have positive signs. Negative signs of ISO and CLVD components can be obtained by reversing the arrows.

For crustal earthquakes, tensional component in the source mechanism causes positive sign in the non-DC components. In geothermal or volcanically active areas opening cracks due to high pressure fluid which may filled by fluid or magma can cause positive ISO and

CLVD components [44–46]. Negative sign in non-DC components indicate compressional components in the source mechanism such as Collapse of a cave [47]. Non-DC components can also be seen when source is a single force. Landslides and volcanic eruptions can be expressed with a single force.

Non-DC components can also be generated by errors in the modeling. Errors in the velocity model, falsely determined earthquake locations, scattered distribution of seismic stations and noise in the seismic record can cause non-DC components. In this thesis, all data is produced synthetically which provides me to get true non-DC components.

CLVD and ISO percentages can be both positive and negative. Positive and negative indicates the direction of the forces which creates CLVD and ISO percentages. Positive ISO component means that forces that create earthquake is from center to outwards. Negative ISO component means that forces that create earthquake is from outwards to center. In other words, source radiates in all directions equally. CLVD sources have one dipole in a specific direction with strength of two and two dipole which are perpendicular to the other with a strength of one. Positive CLVD has a dipole with strength of two which is from center to outwards. In negative CLVD source this dipole is from outwards to center.

2.11. Determining Closest Isotropic Elasticity Tensor

The usage of the closest isotropic elasticity tensor is that one can calculate the distance between the given anisotropic elasticity tensor and closest isotropic tensor of it. One of the purposes of this thesis is to correlate the non-DC components of moment tensor and distance of the elasticity tensor to isotropy. This distance is basically measures the distance between elasticity tensor's distance from isotropic space. Our suggestion is that there is a direct proportion between them. Non-DC components' percentages get higher if the given elasticity tensor is farther from the isotropic space.

Let say, C is a anisotropic elasticity tensor and C^{ISO} is the closest isotropic elasticity tensor of C. Determination of closest isotropic elasticity tensor is done as below [2],

$$C_{11}^{ISO} = C_{22}^{ISO} = C_{33}^{ISO} = \frac{1}{15}[3(C_{11}+C_{22}+C_{33})+2(C_{12}+C_{13}+C_{23})+4(C_{66}+C_{55}+C_{44})]$$
$$C_{12}^{ISO} = C_{13}^{ISO} = C_{23}^{ISO} = \frac{1}{15}[C_{11}+C_{22}+C_{33}+4(C_{12}+C_{13}+C_{23})-2(C_{66}+C_{55}+C_{44})]$$
$$C_{66}^{ISO} = C_{55}^{ISO} = C_{44}^{ISO} = \frac{1}{15}[C_{11}+C_{22}+C_{33}-(C_{12}+C_{13}+C_{23})+3(C_{66}+C_{55}+C_{44})]. \tag{2.58}$$

These distances are also correlated with P and S wave anisotropies. In order to calculate the P and S wave anisotropies we used MATLAB® based software named MTEX [48].

2.12. Data

2.12.1. Elasticity Tensors

In this thesis we used several anisotropic elasticity tensor which represent by using various minerals, rocks and sub surfaces. Our assumption is that whole fault plane composed of these materials. TI [49, 50], orthotopic [11, 49] and monoclinic [51, 52] elasticity tensors are used in order to construct the fault plane.

2.12.1.1. Transversely Isotropic Elasticity Tensors. We used two different TI elasticity tensors. Elasticity tensors of materials, their physical properties and distance function figures (Appendix A) of these materials are given as below.
One of the TI elasticity tensor that we used is determined by [49]. It is a Gneiss material which is from German Continental Drilling Programme (KTB) on 7.9 - 8.2 km of the drilling. It has density of 2.75 $grcm^{-3}$. Elasticity tensor of this Gneiss is given below. By using these

figure we can see the symmetry or the orientation of the elasticity tensor of layering.

$$C^{GNEISS} = \begin{bmatrix} 102.7 & 25.1 & 25.2 & 0 & 0 & 0 \\ 25.1 & 102.7 & 25.2 & 0 & 0 & 0 \\ 25.2 & 25.2 & 71.8 & 0 & 0 & 0 \\ 0 & 0 & 0 & 26.9 & 0 & 0 \\ 0 & 0 & 0 & 0 & 26.9 & 0 \\ 0 & 0 & 0 & 0 & 0 & 38.8 \end{bmatrix}$$

Distance function figure of the material is given in Figure 2.6. One can see that material has infinite fault rotation axis.

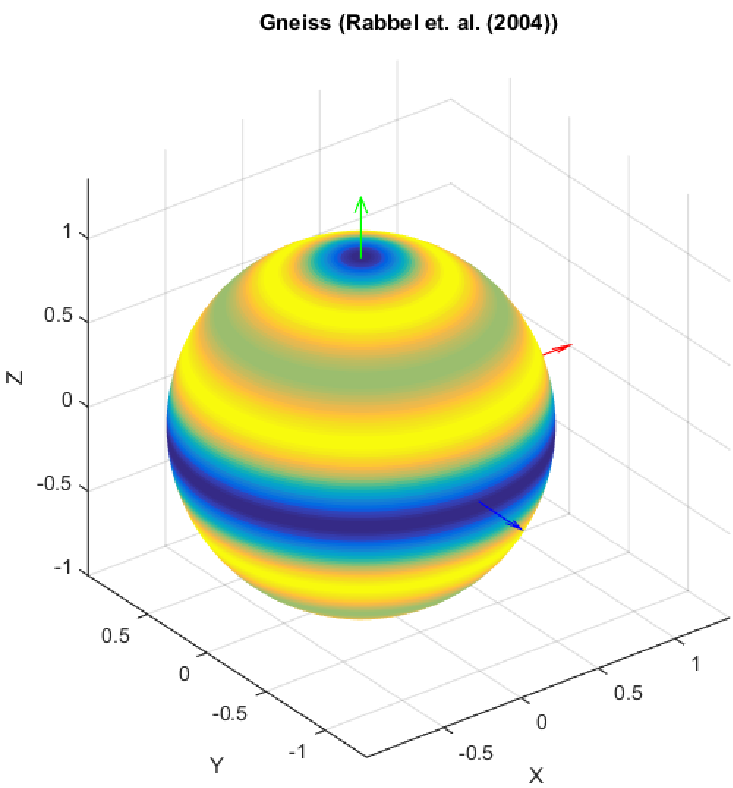

Figure 2.6. Distance Function of Elasticity tensor of Gneiss. Distance function calculates the distance between given elasticity tensor and monoclinic space [2]. By using these figure we can see the symmetry or the orientation of the elasticity tensor of layering. Dark blue represent the normal of the mirror plane orientation.

Second TI elasticity tensor that we used is calculated by [50]. It is Amphibolite mineral with the density of 3.13 $grcm^{-3}$. Elasticity tensor of Amphibolite is given below

$$C^{AMPHIBOLITE} = \begin{bmatrix} 123.1 & 45.6 & 42.8 & 0 & 0 & 0 \\ 45.6 & 123.1 & 42.8 & 0 & 0 & 0 \\ 42.8 & 42.8 & 160.7 & 0 & 0 & 0 \\ 0 & 0 & 0 & 43.3 & 0 & 0 \\ 0 & 0 & 0 & 0 & 43.3 & 0 \\ 0 & 0 & 0 & 0 & 0 & 38.75 \end{bmatrix}$$

Distance function figure of the material is given in Figure 2.7.

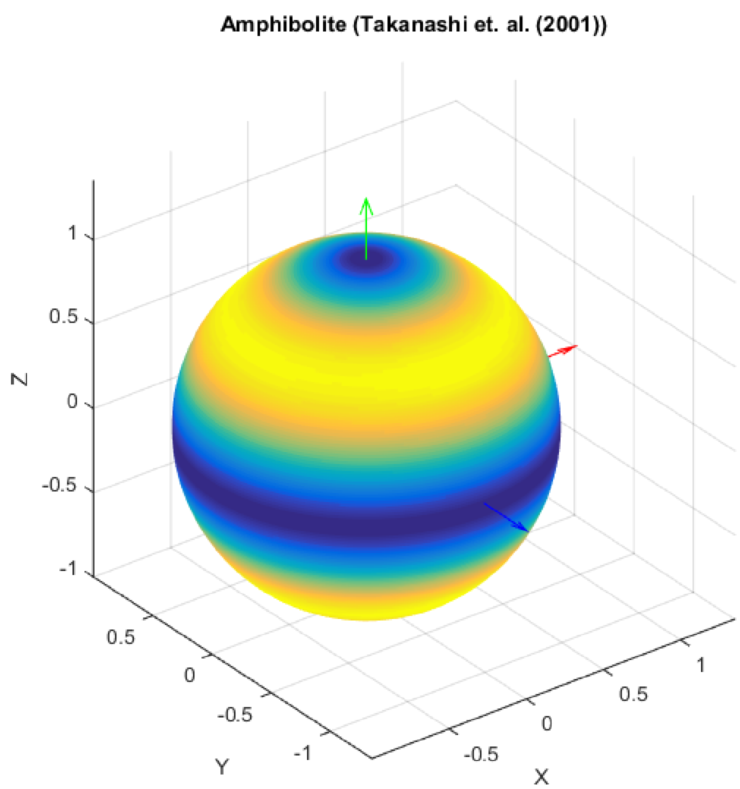

Figure 2.7. Distance Function of Elasticity tensor of Amphibolite

2.12.1.2. Orthotropic Elasticity Tensors. Two different orthotropic elasticity tensors are used. Elasticity tensors of materials, their physical properties and distance function Figures (Appendix A) of these materials are given as below.
First orthotropic material that we used is studied by [49] . It has density of 2.64 $grcm^{-3}$. Granite rock has elasticity tensor as below

$$C^{GRANITE} = \begin{bmatrix} 72.27 & 21.25 & 23.84 & 0 & 0 & 0 \\ 21.25 & 69.00 & 22.13 & 0 & 0 & 0 \\ 23.84 & 22.13 & 75.06 & 0 & 0 & 0 \\ 0 & 0 & 0 & 27.31 & 0 & 0 \\ 0 & 0 & 0 & 0 & 26.46 & 0 \\ 0 & 0 & 0 & 0 & 0 & 24.92 \end{bmatrix}$$

Distance function figure of the material is given in Figure 2.8.

Second orthotropic elasticity tensor is determined for subsurface of Tonga Deep Zone which is taken from Vavryčuk [11]. It has density of 3.92 $grcm^{-3}$. Elasticity tensor of Tonga Deep Zone is given below

$$C^{TONGA} = \begin{bmatrix} 421.8 & 145.0 & 188.9 & 0 & 0 & 0 \\ 145.0 & 447.3 & 149.9 & 0 & 0 & 0 \\ 188.9 & 149.9 & 404.9 & 0 & 0 & 0 \\ 0 & 0 & 0 & 110.5 & 0 & 0 \\ 0 & 0 & 0 & 0 & 154.8 & 0 \\ 0 & 0 & 0 & 0 & 0 & 134.5 \end{bmatrix}$$

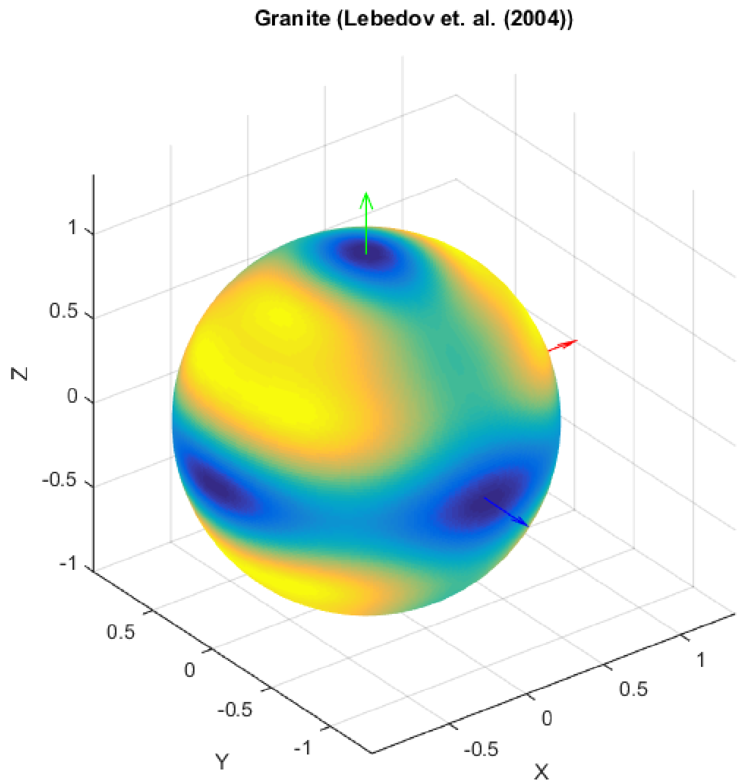

Figure 2.8. Distance Function of Elasticity tensor of Granite. Thus we can see that there are three mirror planes that orthogonal to each other. Dark blue represent the normal of the mirror plane orientation.

Distance function of Tonga Deep Zone is given in Figure 2.9

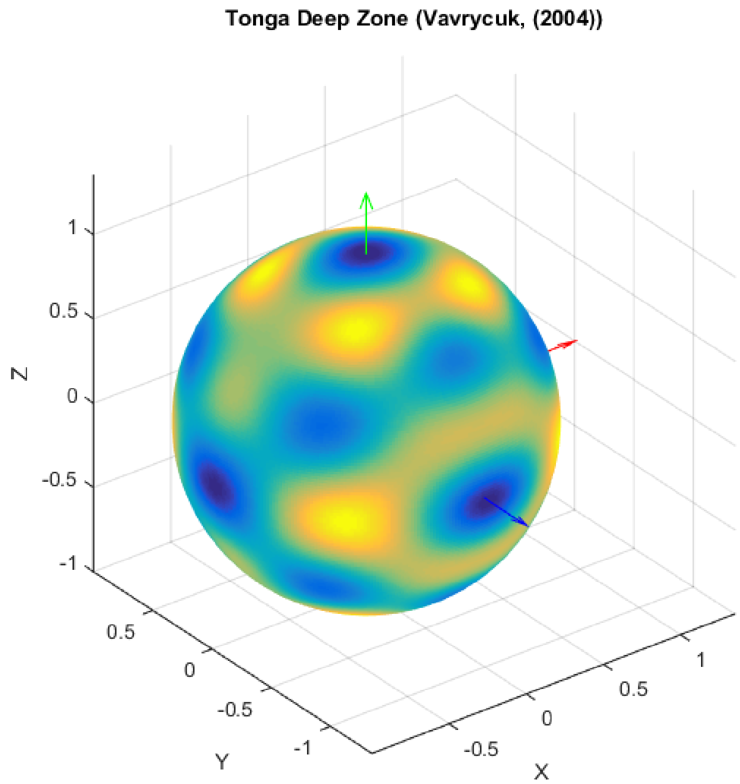

Figure 2.9. Distance Function of Elasticity tensor of Tonga Deep Zone

<u>2.12.1.3. Monoclinic Elasticity Tensors.</u> Two different monoclinic elasticity tensors are choose for the thesis. Elasticity tensors of materials, their physical properties and distance function Figures (Appendix A) of these materials are given as below.

One of the monoclinic elasticity tensor that we used is calculated for Albite mineral by [51]. It has a density of 2.62 $grcm^{-3}$. Elasticity tensor of the mineral is given below

$$C^{ALBITE} = \begin{bmatrix} 74 & 36 & 39 & 0 & -6.6 & 0 \\ 36 & 131 & 31 & 0 & -13 & 0 \\ 39 & 31 & 128 & 0 & -20 & 0 \\ 0 & 0 & 0 & 17 & 0 & -25 \\ -6.6 & -13 & -20 & 0 & 30 & 0 \\ 0 & 0 & 0 & -25 & 0 & 32 \end{bmatrix}$$

Distance function of Albite is given 2.10

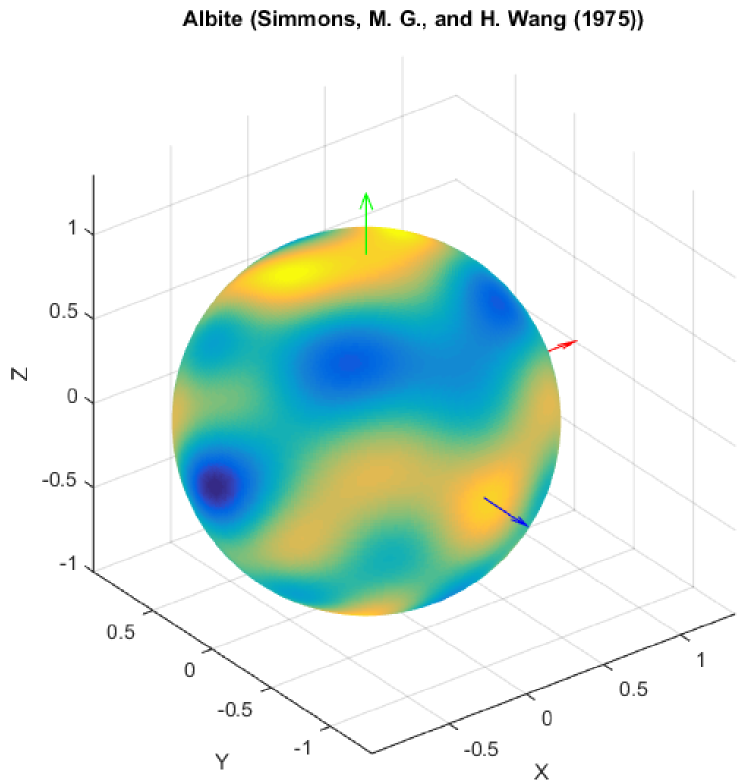

Figure 2.10. Distance Function of Elasticity tensor of Albite. Monoclinic elasticity tensor has only one mirror plane. Dark blue represent the normal of the mirror plane orientation.

Another monoclinic elasticity tensor that we used is calculated for Sanidine mineral which is calculated by [52]. It has a density of 2.57 $grcm^{-3}$. Elasticity tensor of the mineral is given below

$$C^{SANIDINE} = \begin{bmatrix} 69.3 & 41.6 & 24.0 & 0 & 0.6 & 0 \\ 41.6 & 176.2 & 14.3 & 0 & -9.4 & 0 \\ 24.0 & 14.3 & 160.8 & 0 & 7.1 & 0 \\ 0 & 0 & 0 & 19.2 & 0 & -11.5 \\ 0.6 & -9.4 & 7.1 & 0 & 19.4 & 0 \\ 0 & 0 & 0 & -11.5 & 0 & 33.4 \end{bmatrix}$$

Distance function of Sanidine is given in Figure 2.11

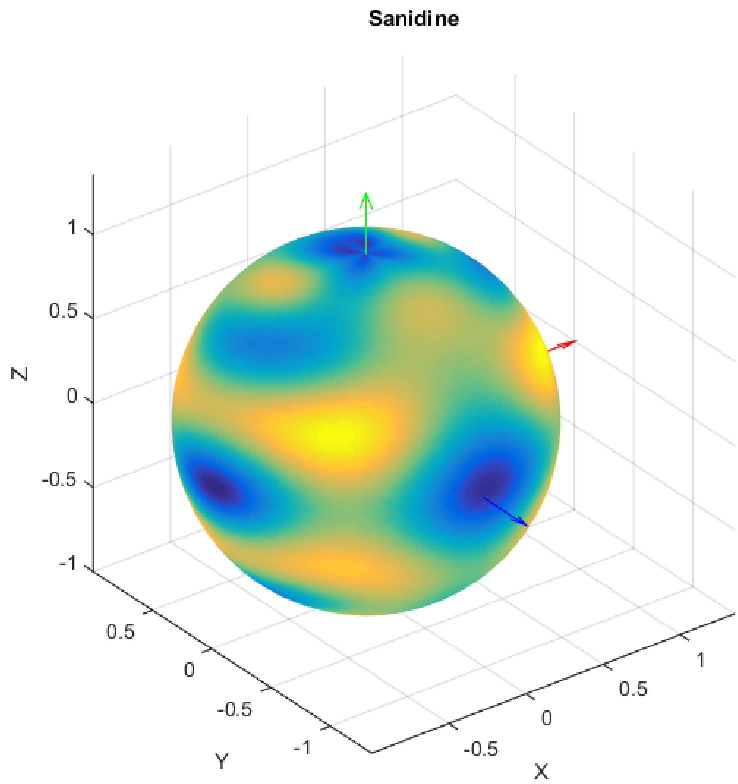

Figure 2.11. Distance Function of Elasticity tensor of Sanidine. Dark blue represent the normal of the mirror plane orientation. However, figure suggest that corresponding elasticity tensor is close to orthotropic symmetry.

2.12.2. Fault Parameters

In order to calculate moment tensors we also used shear source faults. Five fundamental shear faults which are left & right lateral strike slip, normal, reverse and dip slip fault models are used. Moment tensors are calculated by matrix multiplication of elasticity tensor, **C**, and fault vector **d**.

Table 2.1. Fault Parameters

Fault Type	Strike	Dip	Rake	d
Left Lateral Strike Slip	90	90	0	[0 0 0 0 0 -1]
Right Lateral Strike Slip	90	90	180	[0 0 0 0 0 1]
Reverse	90	45	90	[-0.5 0 0 0.5 0 0 0]
Normal	90	45	-90	[0.5 0 -0.5 0 0 0]
Dip-Slip	90	90	90	[0 0 0 0 1.0 0]

3. RESULTS

In this chapter, we first demonstrate figures that shows variations of fault orientations and slip directions due to anisotropic source region. Secondly, we plot figures that shows non-DC components percentage for different orientation of the layers in the source region. Thirdly, distance from isotropic space for given anisotropic elasticity tensor are plotted.

Moment tensors are produced for every possible rotation of given elasticity tensor. Physically this corresponds to changes the orientations of the layers in the source region. Thus each rotation of elasticity tensor varies the angle between the fault directions (fault normal and slip direction) and layers. Rotation is done by using Euler angle rotation. TI elasticity tensors have no sensitivity on θ angle. This process is done in order to visualize the results. Maximum and mean values of decomposition result for orthotropic and monoclinic materials are also divided into two sub categories which are positive and negative values of the results. Main purpose of doing this process is to understand the characteristics of decomposition results more easily. Some elastic materials' decomposition result may vary dramatically.

Anisotropic source region might change the angles of a fault plane even if the given fault has pure shear features. Elasticity tensor with TI symmetry have no sensitivity on θ angle. Since two Euler angle is enough to determine the orientation of the TI tensor. Hence moment tensor is uniquely defined for a particular direction. This enables to visualize the decomposition results of TI elasticity tensors; namely variation of fault angles and of non-DC percentage component figures.

However this is not the case for orthotropic and monoclinic elasticity tensors since one direction does not determine the orientation of these tensors. Specifically the orientation of other coordinate axes must be determined to produce a unique moment tensor. To overcome this problem, we take both maximum and mean values to achieve a unique number that corresponds to the variation of fault parameter.

In this chapter decomposition results are separated into subsections. All subsections contain different part of decomposition results. Fault angles, non-DC components and distance between the isotropic space and given anisotropic materials' features are given in separate sub sections. All subsections contain all anisotropic elasticity tensors and all fault type results.

3.1. Variation on Fault Angles

Variation of strike, dip and rake angles for given anisotropic source region is evaluated and plotted in this chapter . Results are calculated for six different elasticity tensor and five different fault types. Figures in this section are only plotted for dip-slip fault model except Tonga Deep Zone elasticity tensor. All five fault types results are given for this tensor.

Figures in the following parts of this section is obtained by using the following procedure,
First we rotate elasticity tensor C for every possible orientation by using Euler angles. For each rotation we have different elasticity tensors. Then we generate moment tensor by using this elasticity tensor, **C** and fault plane vector **d**. Then we decompose the generated moment tensor. Then we take the DC part of the moment tensor and obtain the fault plane parameters. Figures in this chapter show the variation between the real values which are given in Table 2.1 and the calculated result from DC part of moment tensor **M**.

3.1.1. Gneiss

Visualizing Gneiss is possible for all angles since it has TI symmetry class and do not sensitivity on θ angle. Figure 3.1 is for dip-slip fault model.

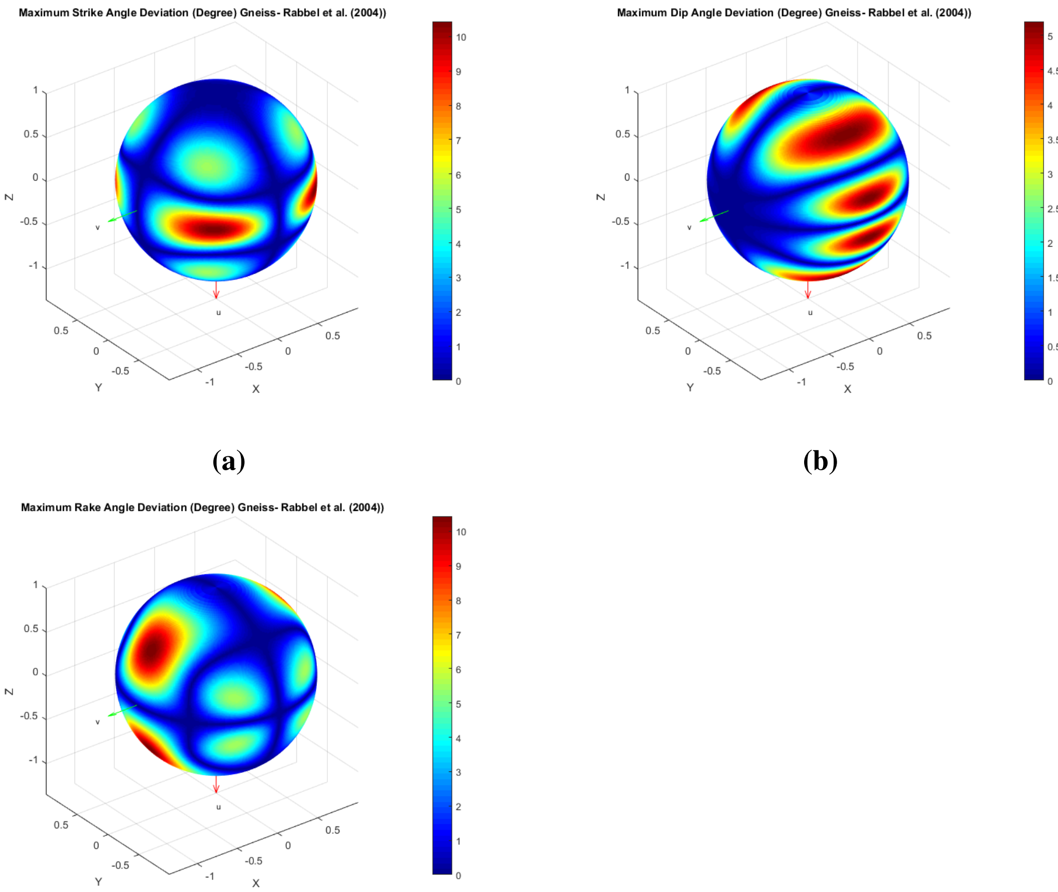

(a) **(b)**

(c)

Figure 3.1. Variation of Fault parameters Φ (a), δ (b) and λ (c) of Gneiss. Red arrow ($\mathbf{u}$) and green arrow ($\mathbf{v}$) are slip vector and fault normal, respectively. Red colored areas imply high variations and dark blue colored areas imply low or no variations. ψ angle increase from left to right on figures. ϕ angle increase from North pole to South pole for fixed ψ angle.

3.1.2. Amphibolite

Visualizing Amphibolite for all possible ϕ and ψ angles. Results can be seen in Figure 3.2

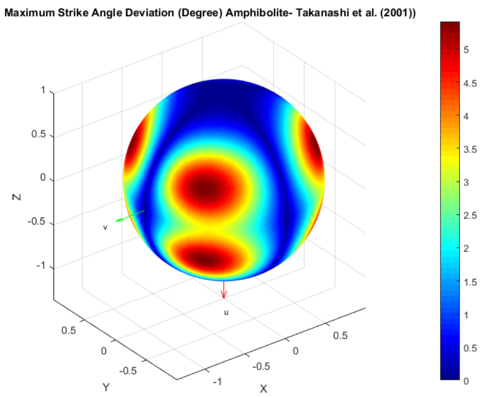

(a)

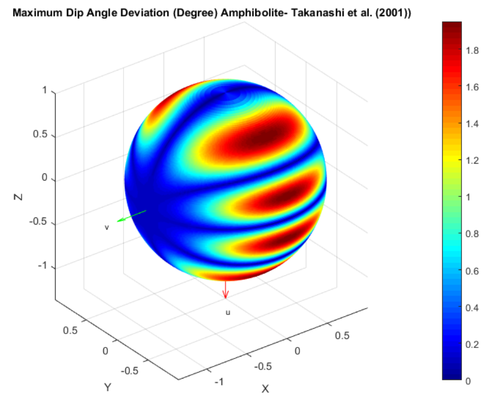

(b)

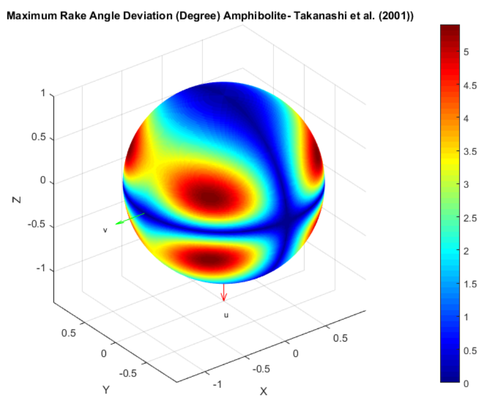

(c)

Figure 3.2. Variation of Fault parameters Φ (a), δ (b) and λ (c) of Amphibolite. Red arrow (**u**) and green arrow (**v**) are slip vector and fault normal, respectively. Red colored areas imply high variations and dark blue colored areas imply low or no variations. ψ angle increase from left to right on figures. ϕ angle increase from North pole to South pole for fixed ψ angle.

3.1.3. Granite

Visualizing Granite is not possible since it has orthotropic symmetry class and has sensitivity on θ angle. In order to overcome this problem we plotted the maximum and mean values of varied θ. Figure 3.3 and Figure 3.4 show maximum and mean plots respectively.

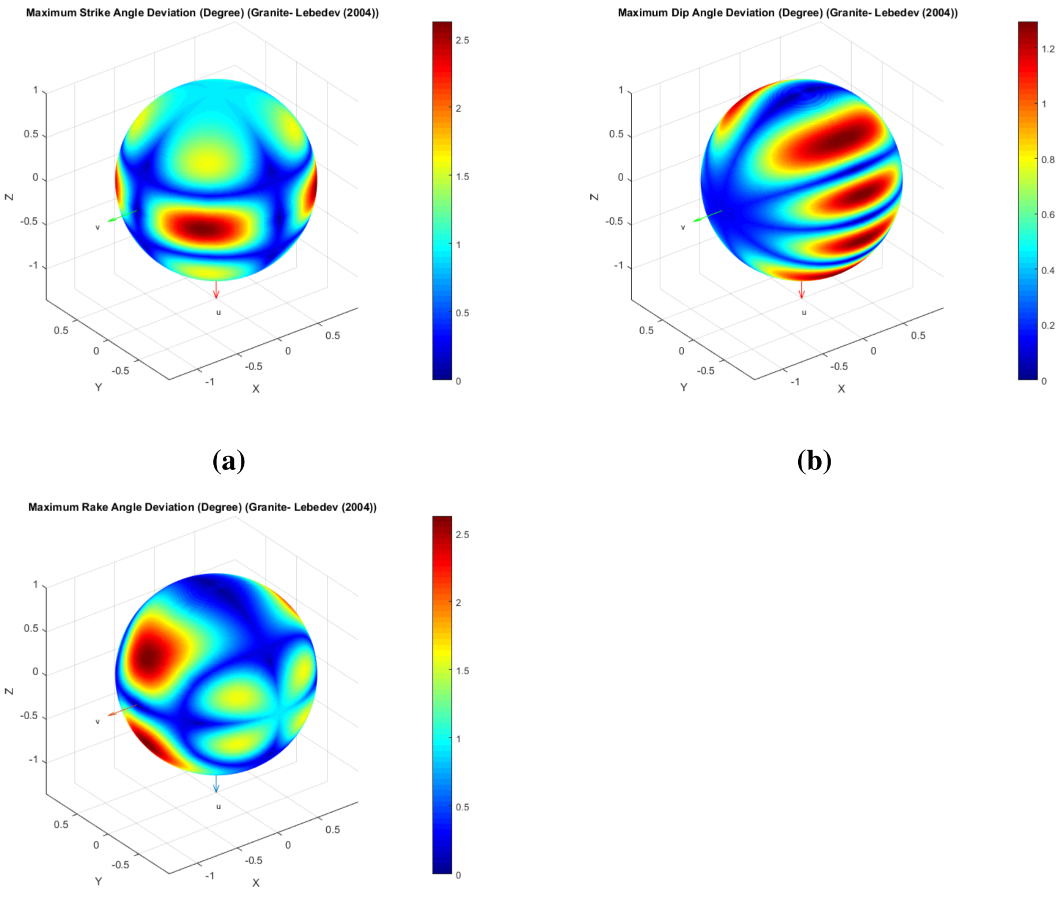

(a) **(b)**

(c)

Figure 3.3. Maximum variation of Fault parameters Φ (a), δ (b) and λ (c) of Granite. Red arrow (**u**) and green arrow (**v**) are slip vector and fault normal, respectively. Red colored areas imply high variations and dark blue colored areas imply low or no variations. ψ angle increase from left to right on figures. ϕ angle increase from North pole to South pole for fixed ψ angle.

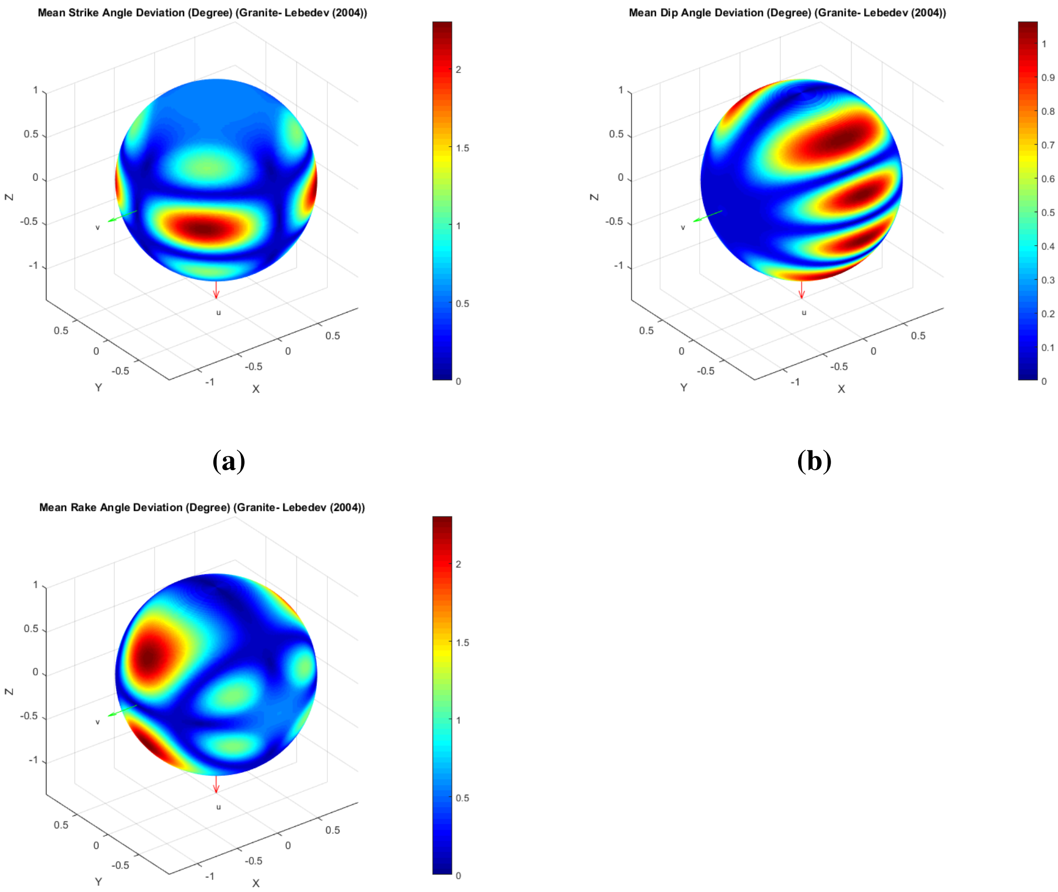

(a) **(b)**

(c)

Figure 3.4. Mean variation of Fault parameters Φ (a), δ (b) and λ (c) of Granite. Red arrow (**u**) and green arrow (**v**) are slip vector and fault normal, respectively. Red colored areas imply high variations and dark blue colored areas imply low or no variations. ψ angle increase from left to right on figures. ϕ angle increase from North pole to South pole for fixed ψ angle.

3.1.4. Tonga Deep Zone

Tonga Deep Zone is the only elasticity tensor which represents a sub surface on this thesis. This is why we plot positive and negative values for all five different fault types of maximum and mean values.

3.1.4.1. Normal Fault. Strike, dip and rake angle are 90,45 and -90 degree respectively. Variation of maximum and mean values are in Figure 3.5 and Figure 3.6.

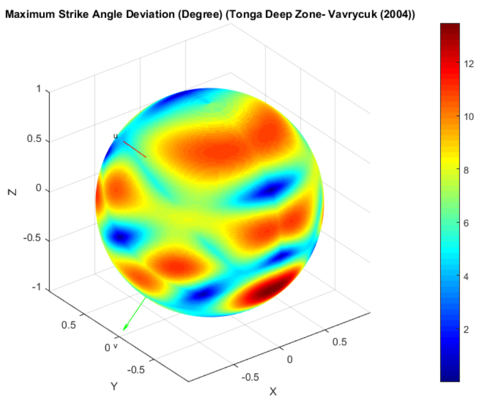

(a)

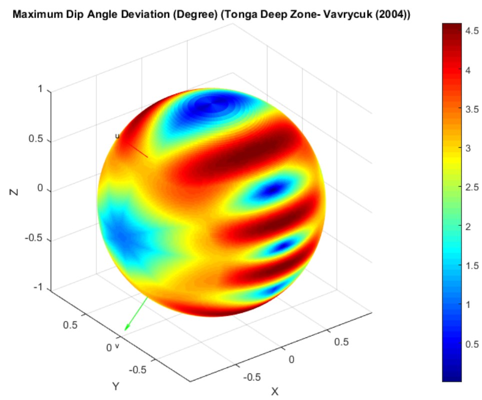

(b)

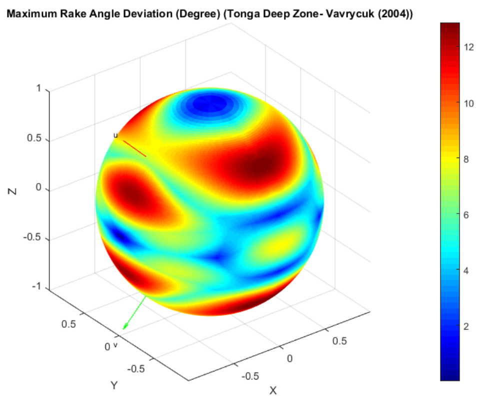

(c)

Figure 3.5. Maximum variation of fault parameters Φ (a), δ (b) and λ (c) of Tonga Deep Zone for Normal Fault. Red arrow (**u**) and green arrow (**v**) are slip vector and fault normal, respectively. Red colored areas imply high variations and dark blue colored areas imply low or no variations. ψ angle increase from left to right on figures. ϕ angle increase from North pole to South pole for fixed ψ angle.

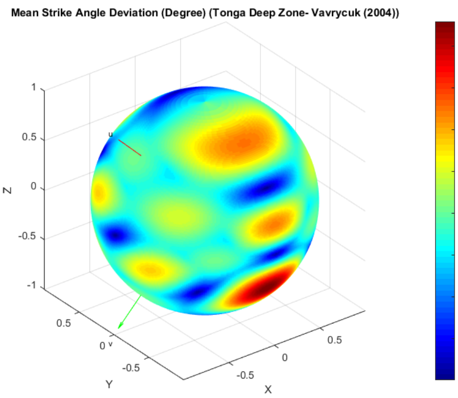

(a)

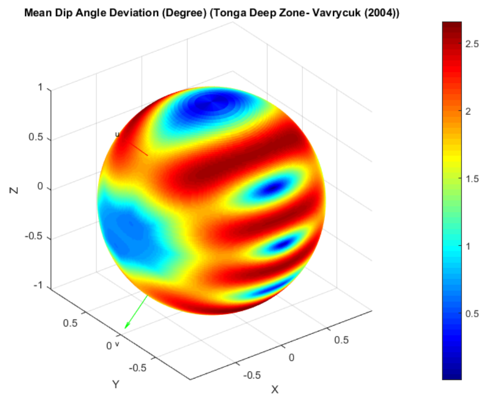

(b)

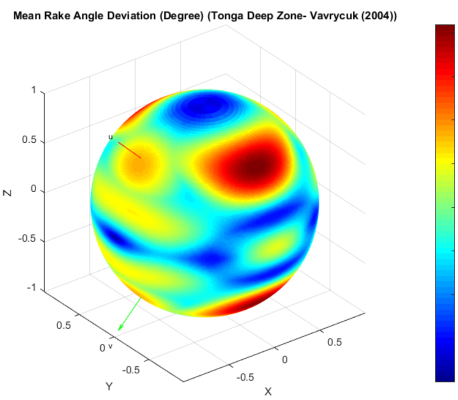

(c)

Figure 3.6. Mean variation of fault parameters Φ (a), δ (b) and λ (c) of Tonga Deep Zone for Normal Fault. Red arrow (**u**) and green arrow (**v**) are slip vector and fault normal, respectively. Red colored areas imply high variations and dark blue colored areas imply low or no variations. ψ angle increase from left to right on figures. ϕ angle increase from North pole to South pole for fixed ψ angle.

<u>3.1.4.2. Reverse Fault.</u> Strike, dip and rake angle are 90, 45 and 90 degree respectively. Variation of maximum and mean values are in Figure 3.7 and Figure 3.8.

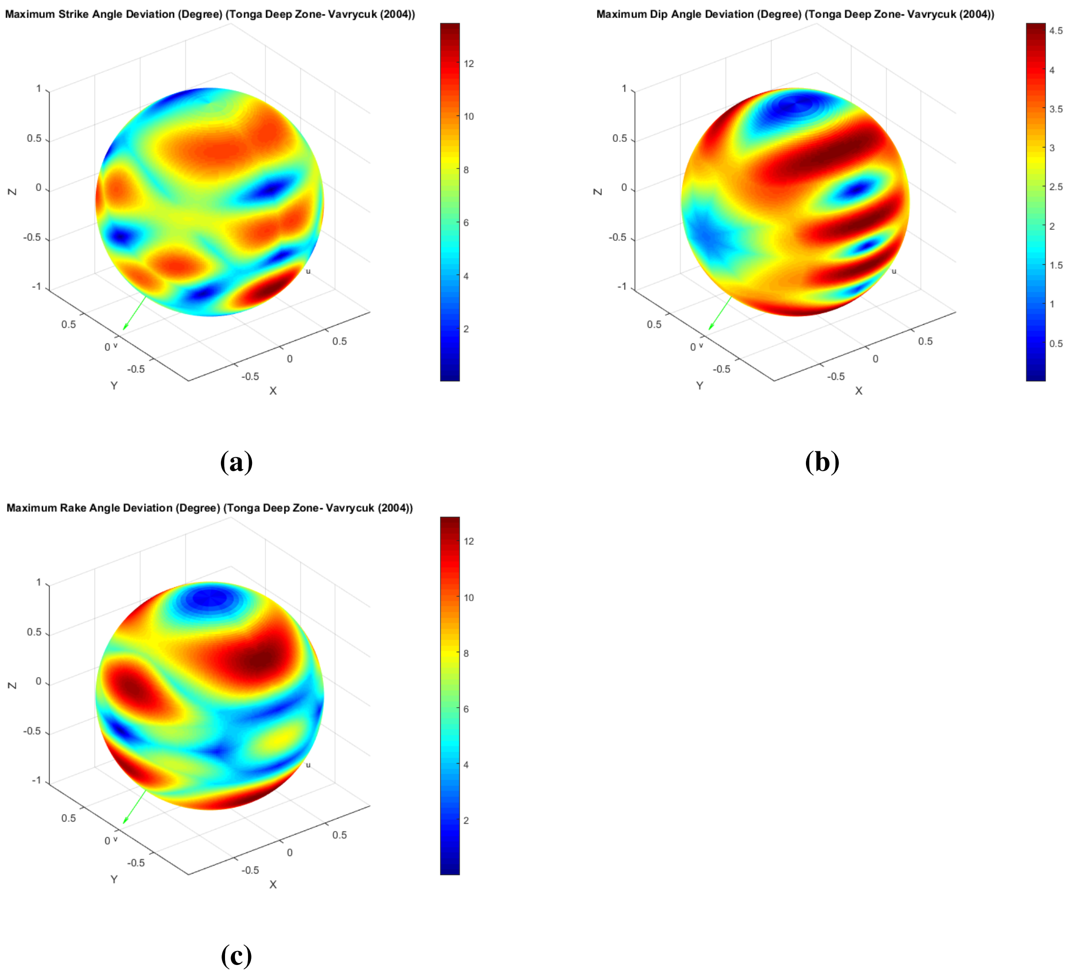

Figure 3.7. Maximum variation of fault parameters Φ (a), δ (b) and λ (c) of Tonga Deep Zone for Reverse Fault. Red arrow (**u**) and green arrow (**v**) are slip vector and fault normal, respectively. Red colored areas imply high variations and dark blue colored areas imply low or no variations. ψ angle increase from left to right on figures. ϕ angle increase from North pole to South pole for fixed ψ angle.

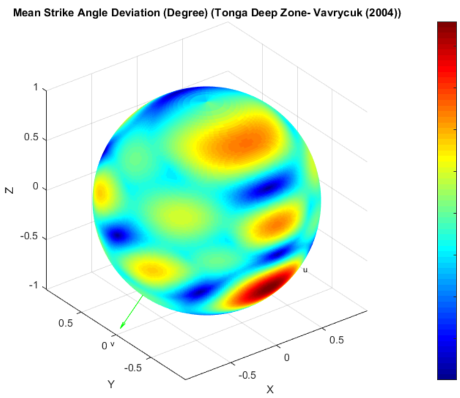

(a)

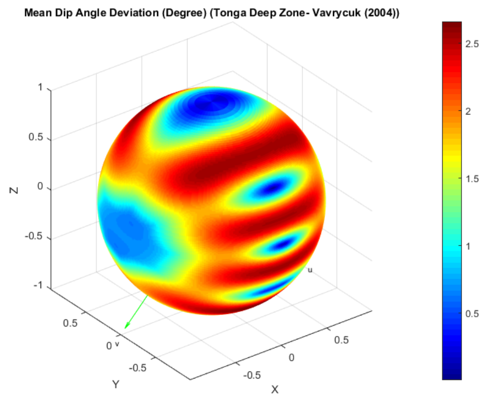

(b)

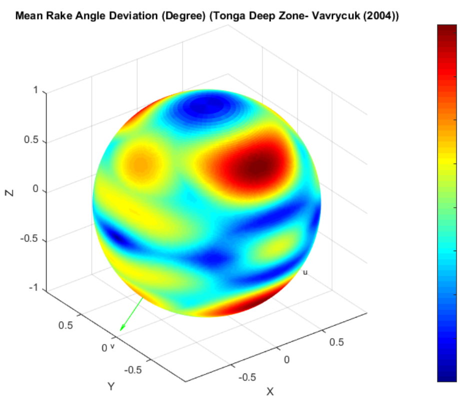

(c)

Figure 3.8. Mean variation of fault parameters Φ (a), δ (b) and λ (c) of Tonga Deep Zone for Reverse Fault. Red arrow (**u**) and green arrow (**v**) are slip vector and fault normal, respectively. Red colored areas imply high variations and dark blue colored areas imply low or no variations. ψ angle increase from left to right on figures. ϕ angle increase from North pole to South pole for fixed ψ angle.

3.1.4.3. Dip-Slip Fault. Strike, dip and rake angle are 90 degree for each parameter. Variation of maximum and mean values are in Figure 3.9 and Figure 3.10.

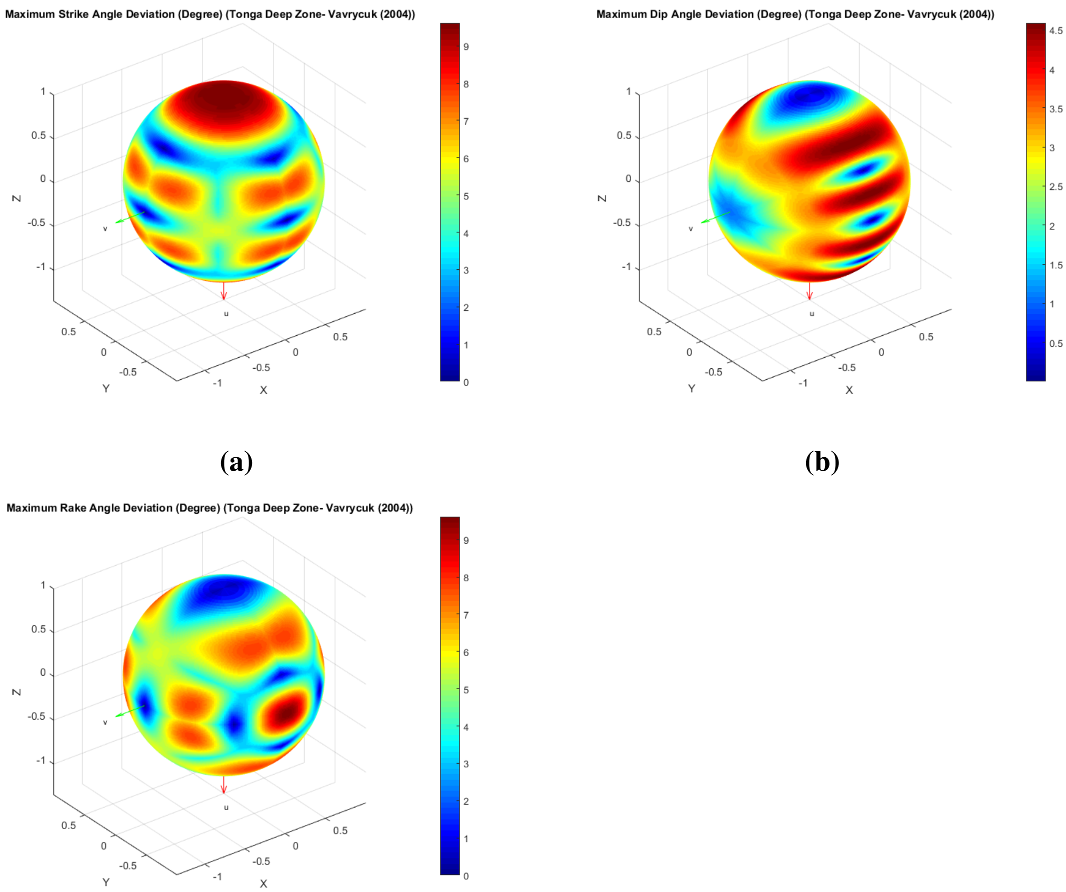

(a) **(b)**

(c)

Figure 3.9. Maximum variation of fault parameters Φ (a), δ (b) and λ (c) of Tonga Deep Zone for Dip-Slip Fault. Red arrow (**u**) and green arrow (**v**) are slip vector and fault normal, respectively. Red colored areas imply high variations and dark blue colored areas imply low or no variations. ψ angle increase from left to right on figures. ϕ angle increase from North pole to South pole for fixed ψ angle.

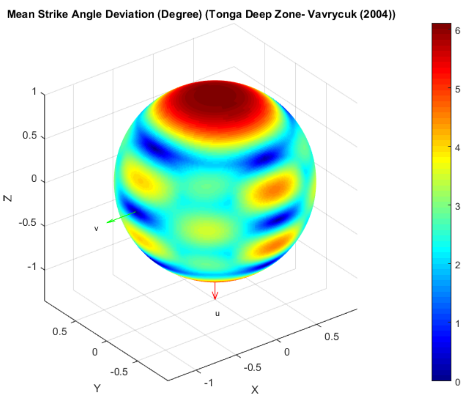

(a)

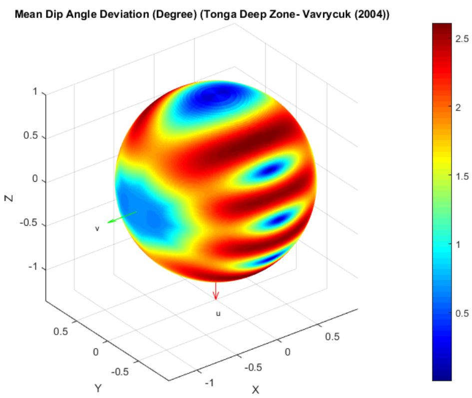

(b)

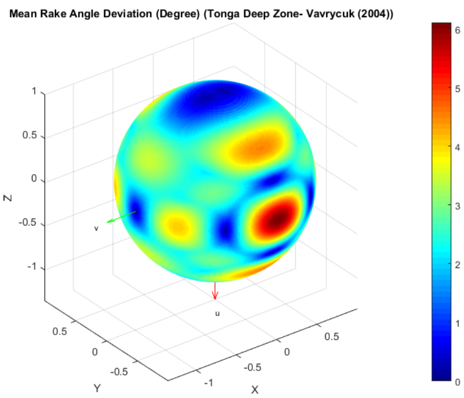

(c)

Figure 3.10. Mean variation of fault parameters Φ (a), δ (b) and λ (c) of Tonga Deep Zone for Dip-Slip Fault. Red arrow (**u**) and green arrow (**v**) are slip vector and fault normal, respectively. Red colored areas imply high variations and dark blue colored areas imply low or no variations. ψ angle increase from left to right on figures. ϕ angle increase from North pole to South pole for fixed ψ angle.

3.1.4.4. Left Lateral Strike Slip Fault. Strike, dip and rake angle are 90, 90 and 0 degree respectively. Variation of maximum and mean values are in Figure 3.11 and Figure 3.12.

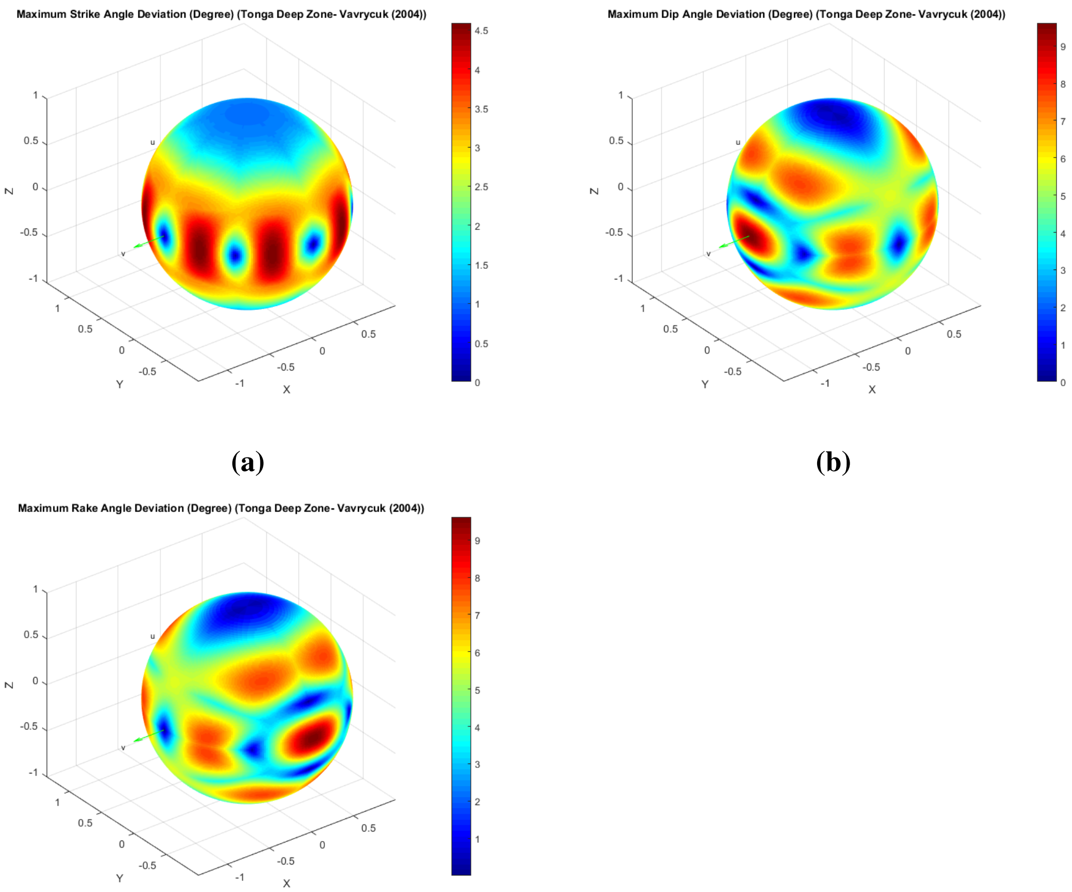

(a) **(b)** **(c)**

Figure 3.11. Maximum variation of fault parameters Φ (a), δ (b) and λ (c) of Tonga Deep Zone for Left Lateral Strike Slip Fault. Red arrow (**u**) and green arrow (**v**) are slip vector and fault normal, respectively. Red colored areas imply high variations and dark blue colored areas imply low or no variations. ψ angle increase from left to right on figures. ϕ angle increase from North pole to South pole for fixed ψ angle.

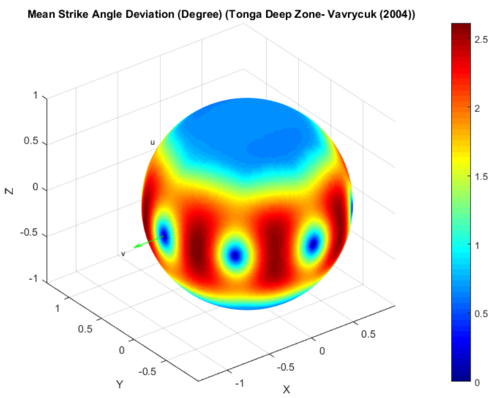

(a)

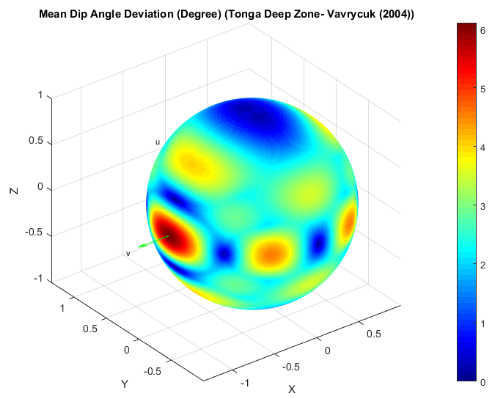

(b)

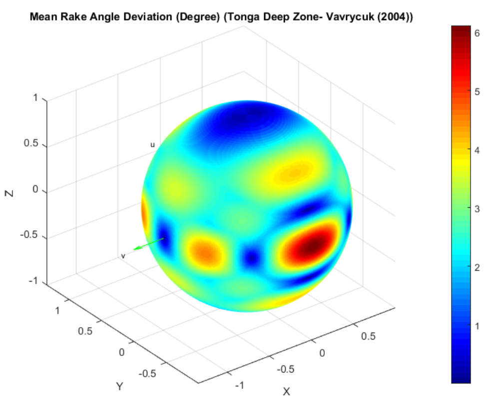

(c)

Figure 3.12. Mean variation of fault parameters Φ (a), δ (b) and λ (c) of Tonga Deep Zone for Left Lateral Strike Slip Fault. Red arrow (**u**) and green arrow (**v**) are slip vector and fault normal, respectively. Red colored areas imply high variations and dark blue colored areas imply low or no variations. ψ angle increase from left to right on figures. ϕ angle increase from North pole to South pole for fixed ψ angle.

3.1.4.5. Right Lateral Strike Slip Fault. Strike, dip and rake angle are 90, 90 and 180 degree respectively. Variation of maximum and mean values are in Figure 3.13 and Figure 3.14.

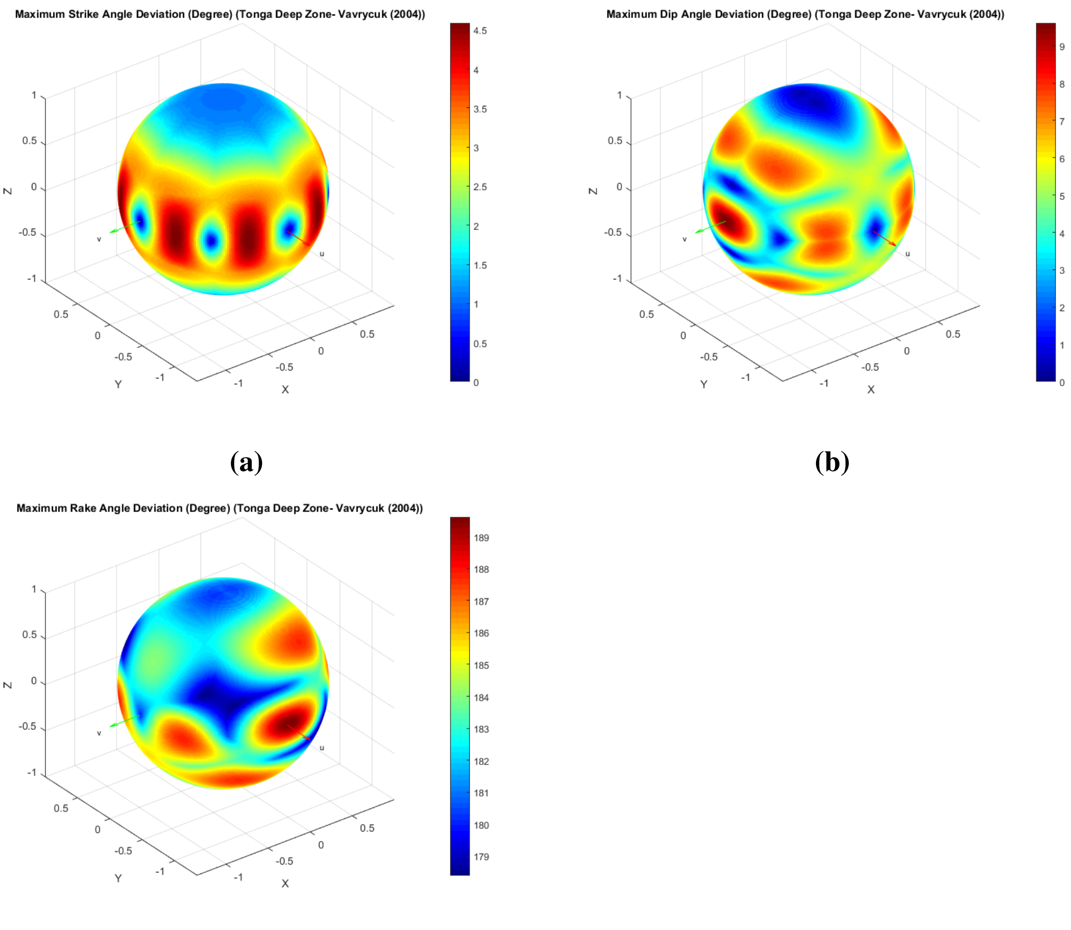

(a) **(b)**

(c)

Figure 3.13. Maximum variation of fault parameters Φ (a), δ (b) and λ (c) of Tonga Deep Zone for Right Lateral Strike Slip Fault. Red arrow (**u**) and green arrow (**v**) are slip vector and fault normal, respectively. Red colored areas imply high variations and dark blue colored areas imply low or no variations. ψ angle increase from left to right on figures. ϕ angle increase from North pole to South pole for fixed ψ angle.

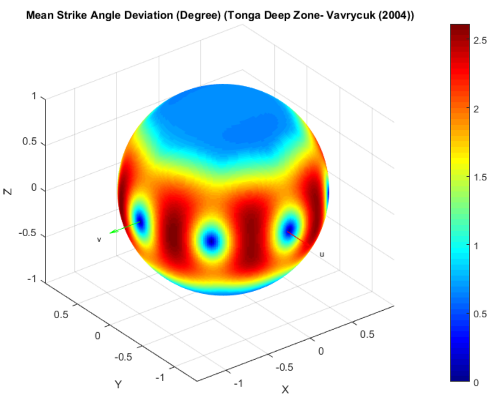

(a)

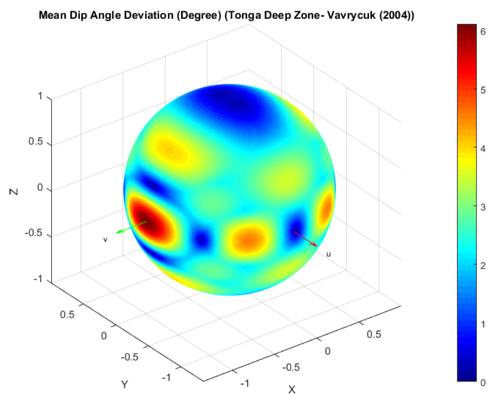

(b)

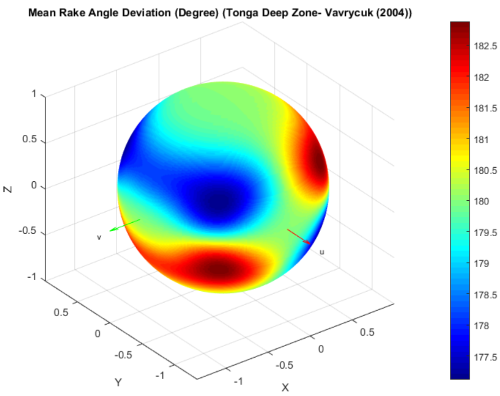

(c)

Figure 3.14. Mean variation of fault parameters Φ (a), δ (b) and λ (c) of Tonga Deep Zone for Right Lateral Strike Slip Fault.

3.1.5. Albite

Albite is one the monoclinic elasticity tensor that we used in order to produce moment tensor. Monoclinic elasticity tensor are sensitive on θ as orthotropic. We plot the maximum and mean values of variation of fault parameters. Figure 3.15 and Figure 3.16 show maximum and mean plots respectively.

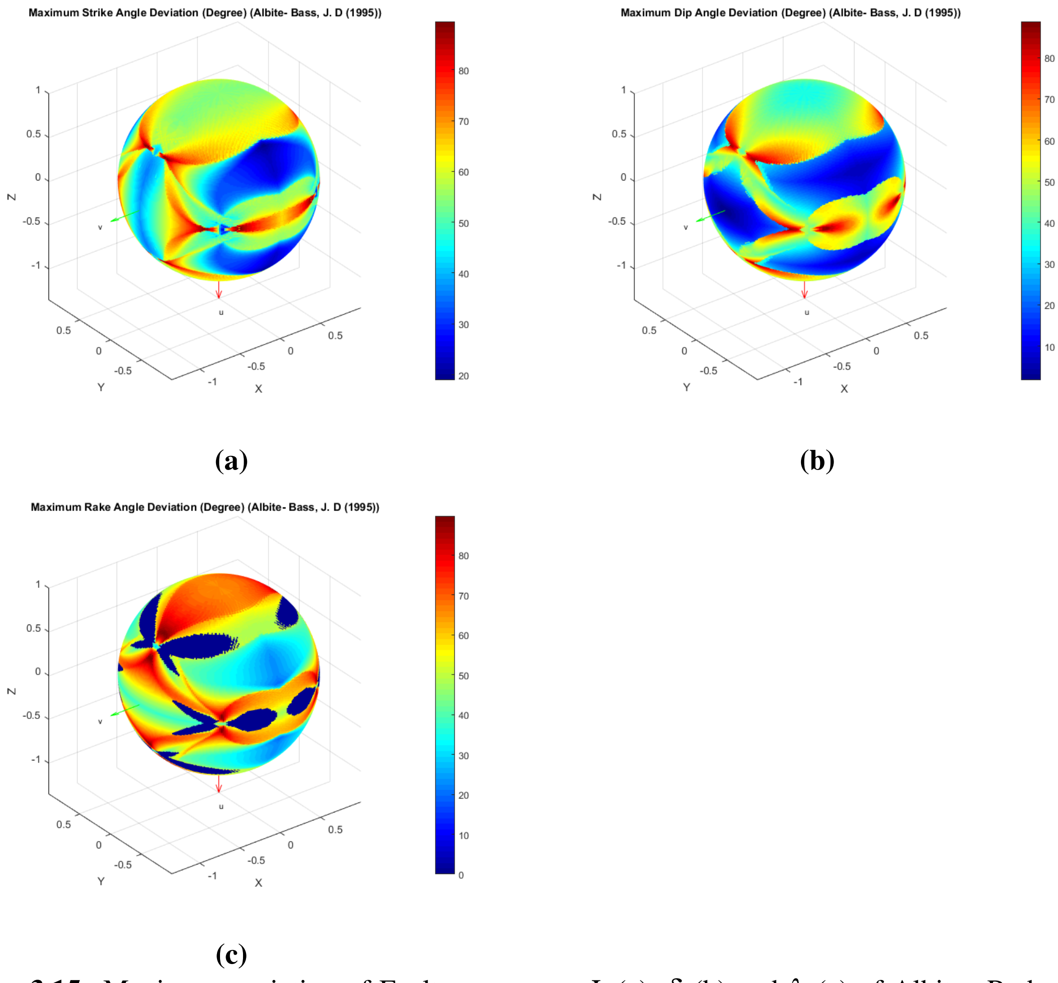

Figure 3.15. Maximum variation of Fault parameters Φ (a), δ (b) and λ (c) of Albite. Red arrow (**u**) and green arrow (**v**) are slip vector and fault normal, respectively. Red colored areas imply high variations and dark blue colored areas imply low or no variations. ψ angle increase from left to right on figures. ϕ angle increase from North pole to South pole for fixed ψ angle.

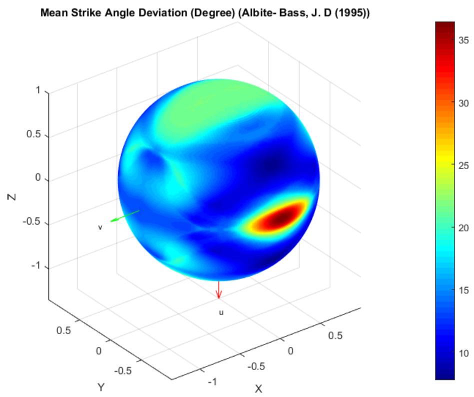

(a)

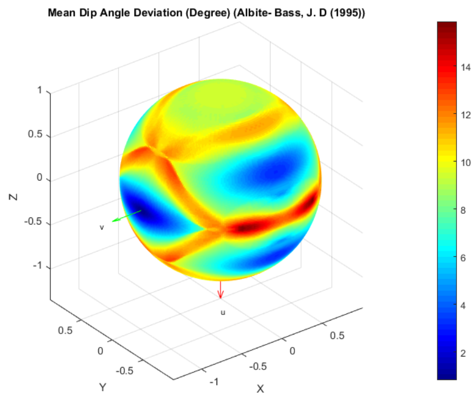

(b)

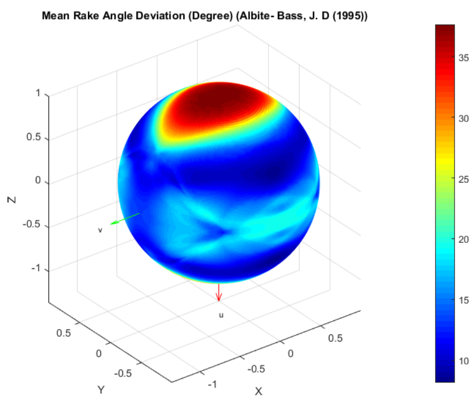

(c)

Figure 3.16. Mean variation of Fault parameters Φ (a), δ (b) and λ (c) of Albite. Red arrow (**u**) and green arrow (**v**) are slip vector and fault normal, respectively. Red colored areas imply high variations and dark blue colored areas imply low or no variations. ψ angle increase from left to right on figures. ϕ angle increase from North pole to South pole for fixed ψ angle.

3.1.6. Sanidine

Sanidine is the second monoclinic elasticity tensor. Monoclinic elasticity tensor are sensitive on θ as orthotropic. We plot the maximum and mean values of variation of fault parameters. Figure 3.17 and Figure 3.18 show maximum and mean plots respectively.

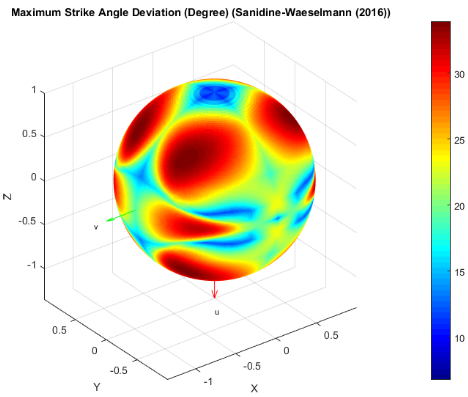

(a)

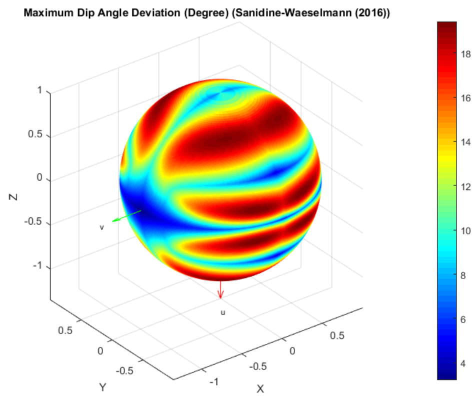

(b)

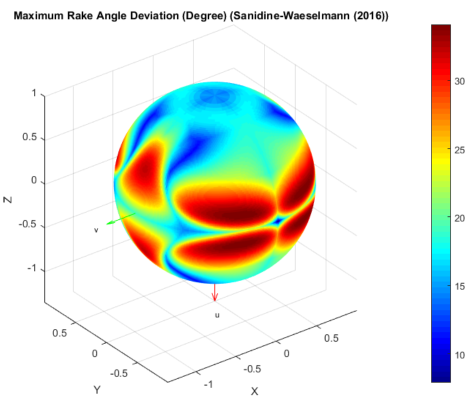

(c)

Figure 3.17. Maximum variation of Fault parameters Φ (a), δ (b) and λ (c) of Sanidine. Red arrow (**u**) and green arrow (**v**) are slip vector and fault normal, respectively. Red colored areas imply high variations and dark blue colored areas imply low or no variations. ψ angle increase from left to right on figures. ϕ angle increase from North pole to South pole for fixed ψ angle.

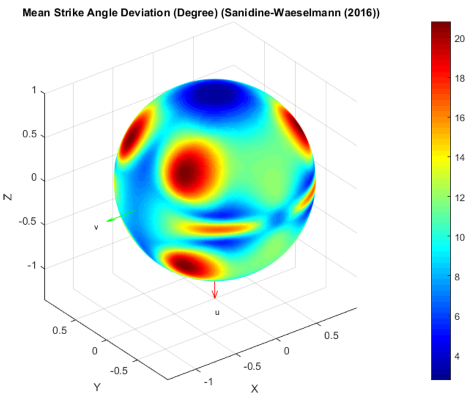

(a)

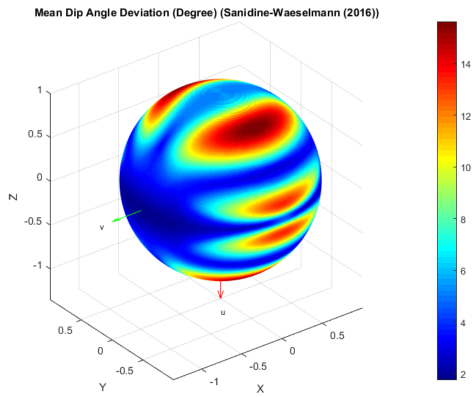

(b)

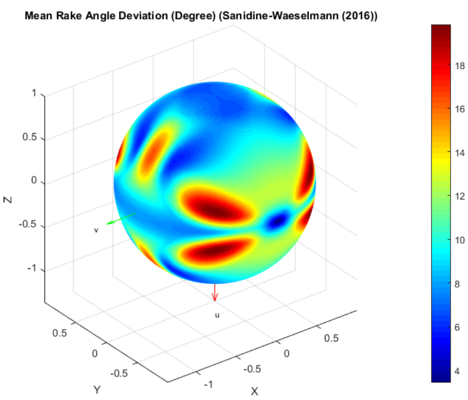

(c)

Figure 3.18. Mean variation of Fault parameters Φ (a), δ (b) and λ (c) of Sanidine. Red arrow (**u**) and green arrow (**v**) are slip vector and fault normal, respectively. Red colored areas imply high variations and dark blue colored areas imply low or no variations. ψ angle increase from left to right on figures. ϕ angle increase from North pole to South pole for fixed ψ angle.

3.2. Variation on Non Double Couple Sources

Non-DC components of earthquake sources are the other parameters on moment tensor decomposition. All our initial earthquake sources are pure shear sources which cannot produce non-DC components in isotropic earthquake source medium. However, anisotropic source region can produce both positive and negative results that indicate the direction of forces that produce earthquakes. Figures in this section are only for dip-slip fault model except Tonga Deep Zone elasticity tensor. All five fault types results are given for this tensor.

Figures in the following parts of this section is obtained by the terminology at below, First we rotate elasticity tensor C for every possible orientation by using Euler angles. For each rotation we have different elasticity tensors. Then we generate by using this elasticity tensor, **C** and fault plane vector **d**. Then we decompose the generated moment tensor. Moreover we find the parts of moment tensor which indicate ISO, DC and CLVD components. Finally the calculate the percentage of ISO, DC and CLVD parts. Figures in this chapter show the positive part of ISO and CLVD percentages except Tonga Deep Zone (Subsection 3.2.4). In subsection 3.2.4 both positive and negative results are plotted.

3.2.1. Gneiss

Visualizing Gneiss is possible for all angles since it has TI symmetry class and do not sensitive on θ angle. Figure 3.19 is for dip-slip fault model.

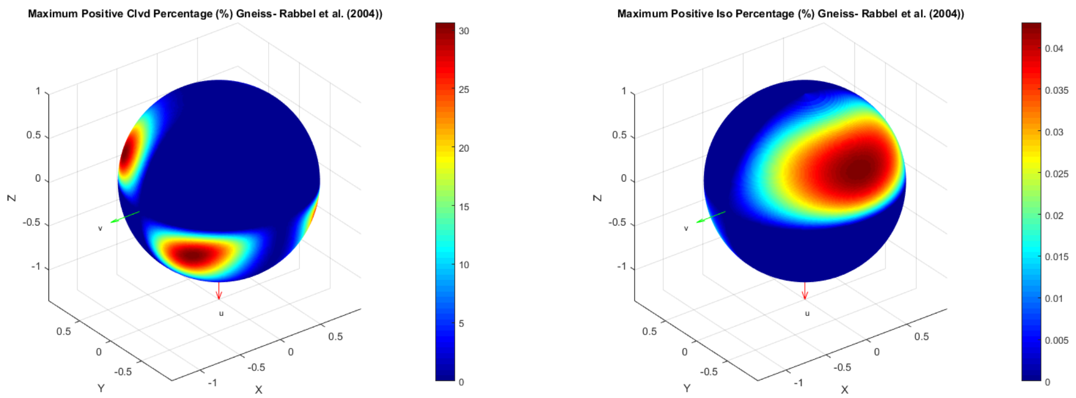

(a) **(b)**

Figure 3.19. Percentage of CLVD (a) and ISO (b) parts of earthquake source of Gneiss. Red arrow (**u**) and green arrow (**v**) are slip vector and fault normal, respectively. Red colored areas imply high percentages and dark blue colored areas imply low or zero percentages. ψ angle increase from left to right on figures. ϕ angle increase from North pole to South pole for fixed ψ angle.

3.2.2. Amphibolite

Amphibolite is the other elasticity tensor with TI features. Figure 3.20 is for dip-slip fault model.

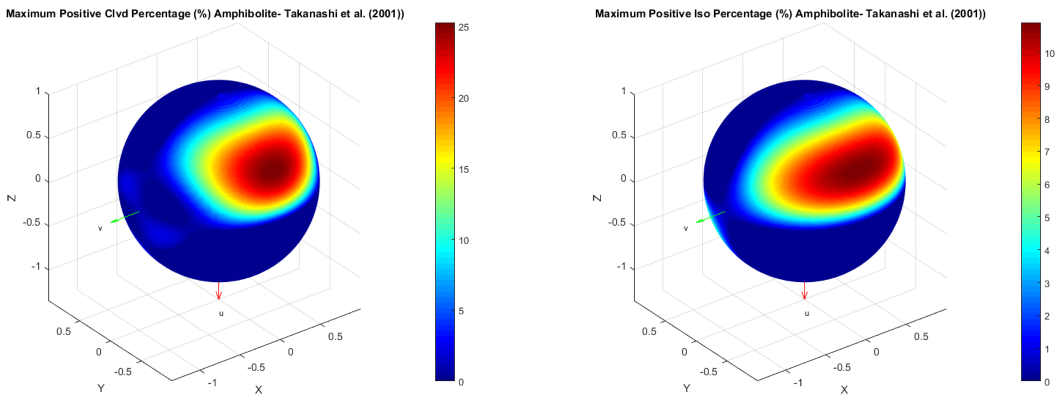

(a) **(b)**

Figure 3.20. Percentage of CLVD (a) and ISO (b) parts of earthquake source of Amphibolite. Red arrow (**u**) and green arrow (**v**) are slip vector and fault normal, respectively. Red colored areas imply high percentages and dark blue colored areas imply low or zero percentages. ψ angle increase from left to right on figures. ϕ angle increase from North pole to South pole for fixed ψ angle.

3.2.3. Granite

Granite has orthotropic symmetry classes. It has sensibility on θ angle. In order to plot its result we take the maximum and mean values on varied θ angle. Decomposition result of Granite material are given in Figure 3.21 and Figure 3.22

3.2.4. Tonga Deep Zone

In this material we plotted results for five different fault types which is also done in subsection 3.1.4. Moreover, we also plotted the cases of positive and negative earthquake sources.

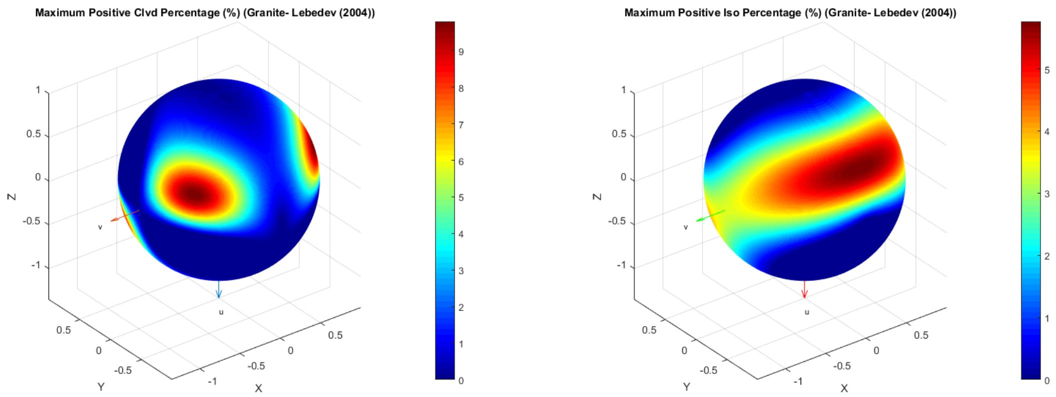

(a) (b)

Figure 3.21. Percentage of maximum CLVD (a) and ISO (b) parts of earthquake source of Granite. Red arrow (**u**) and green arrow (**v**) are slip vector and fault normal, respectively. Red colored areas imply high percentages and dark blue colored areas imply low or zero percentages. ψ angle increase from left to right on figures. ϕ angle increase from North pole to South pole for fixed ψ angle.

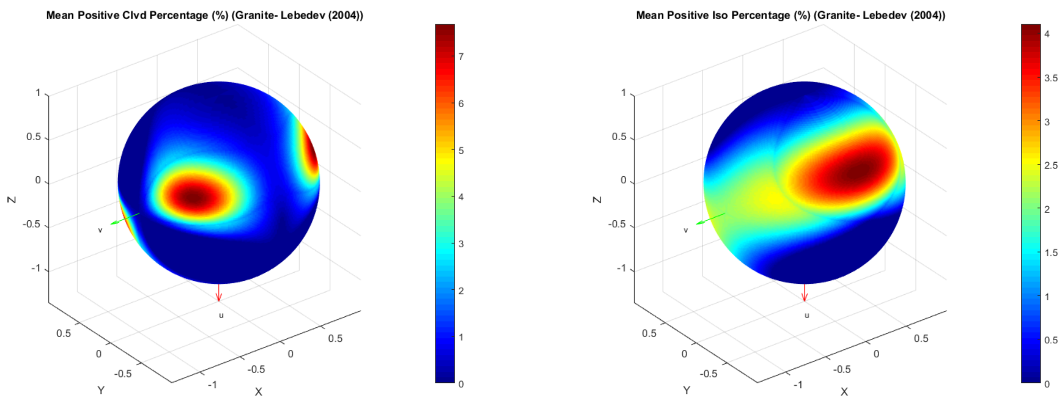

(a) (b)

Figure 3.22. Percentage of mean CLVD (a) and ISO (b) parts of earthquake source of Granite. Red arrow (**u**) and green arrow (**v**) are slip vector and fault normal, respectively. Red colored areas imply high percentages and dark blue colored areas imply low or zero percentages. ψ angle increase from left to right on figures. ϕ angle increase from North pole to South pole for fixed ψ angle.

3.2.4.1. Normal Fault. Results of non-DC components of Tonga Deep Zone elasticity tensor for normal fault are plotted in Figure 3.23 and 3.24.

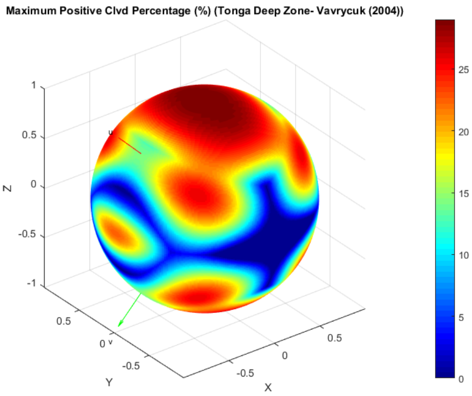

(a)

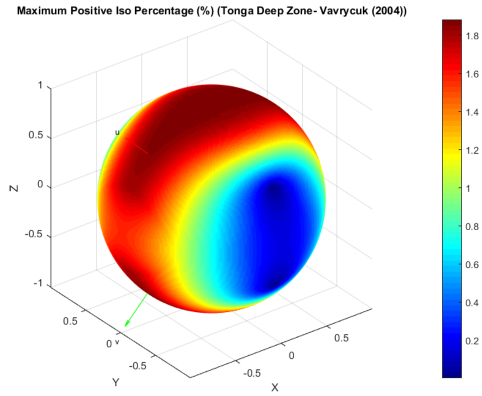

(b)

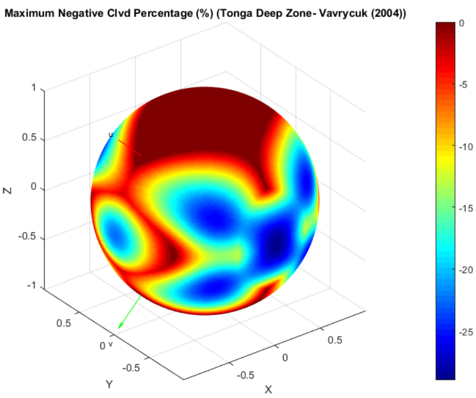

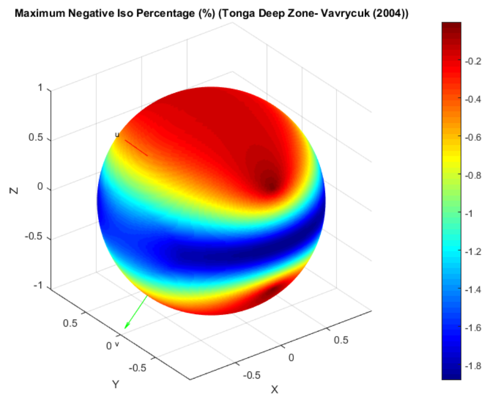

(c) **(d)**

Figure 3.23. Percentage of maximum positive and negative CLVD (a) and ISO (b) parts of earthquake source of Tonga Deep Zone for Normal Fault. Red arrow (**u**) and green arrow (**v**) are slip vector and fault normal, respectively. Red colored areas imply high percentages and dark blue colored areas imply low or zero percentages for positive result. Indication of colors are reversed for negative results. ψ angle increase from left to right on figures. ϕ angle increase from North pole to South pole for fixed ψ angle.

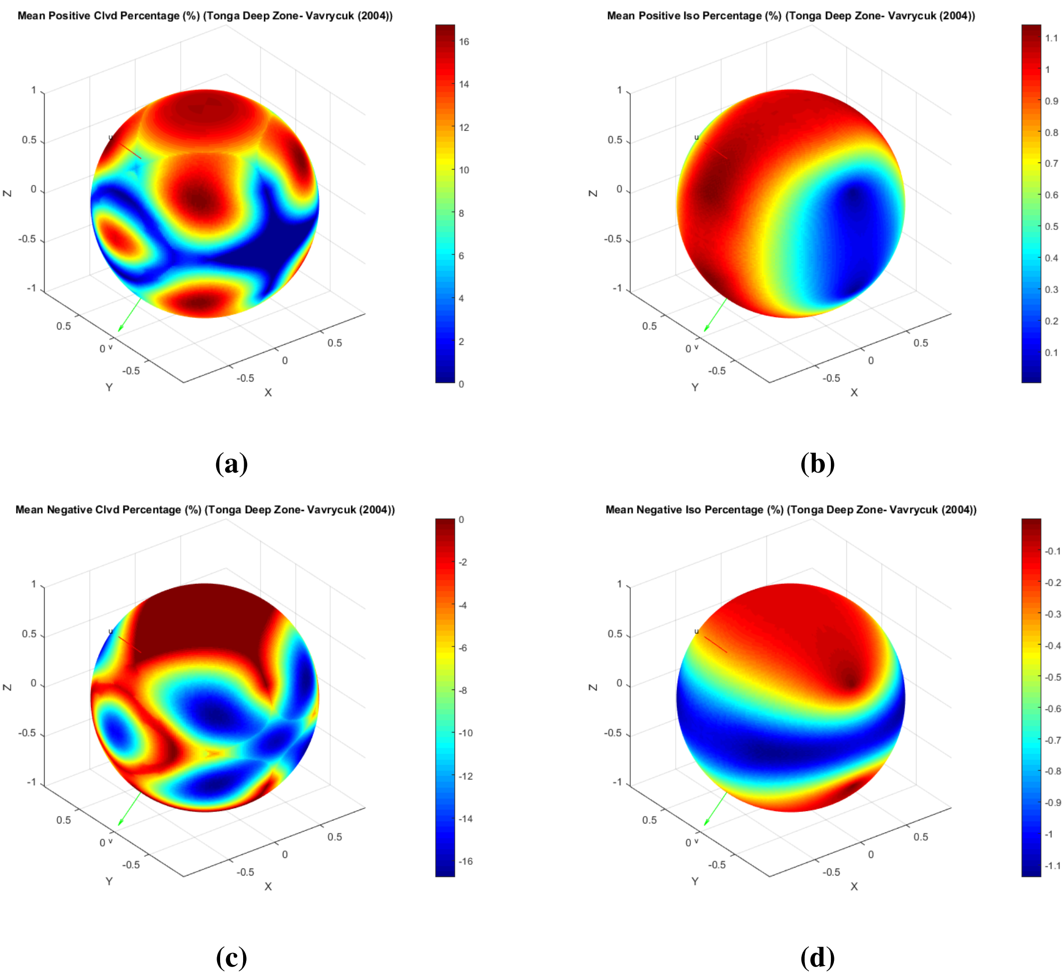

Figure 3.24. Percentage of mean positive and negative CLVD (a) and ISO (b) parts of earthquake source of Tonga Deep Zone for Normal Fault. Red arrow (**u**) and green arrow (**v**) are slip vector and fault normal, respectively. Red colored areas imply high percentages and dark blue colored areas imply low or zero percentages for positive result. Indication of colors are reversed for negative results. ψ angle increase from left to right on figures. ϕ angle increase from North pole to South pole for fixed ψ angle.

3.2.4.2. Reverse Fault. Results of non-DC components of Tonga Deep Zone elasticity tensor for reverse fault are plotted in Figure 3.25 and 3.26.

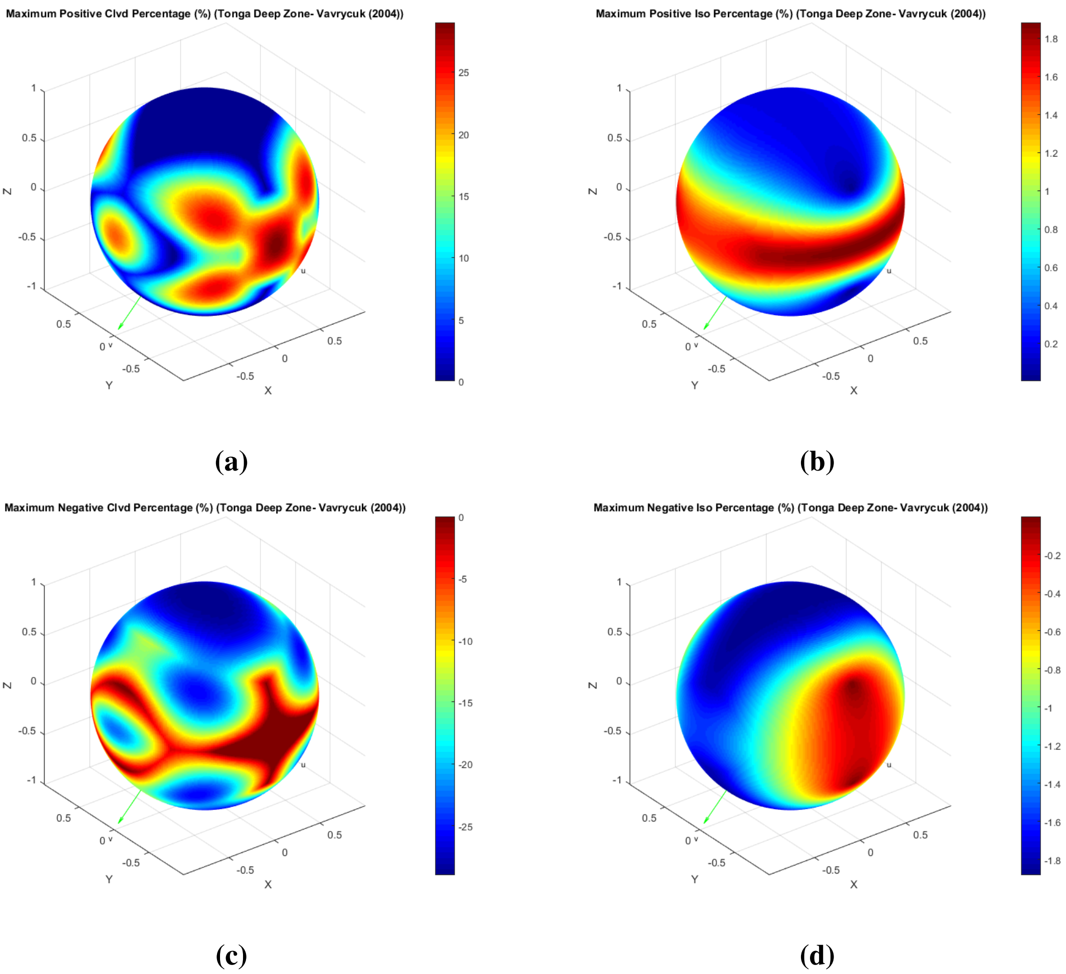

Figure 3.25. Percentage of maximum positive and negative CLVD (a) and ISO (b) parts of earthquake source of Tonga Deep Zone for Reverse Fault. Red arrow (**u**) and green arrow (**v**) are slip vector and fault normal, respectively. Red colored areas imply high percentages and dark blue colored areas imply low or zero percentages for positive result. Indication of colors are reversed for negative results. ψ angle increase from left to right on figures. ϕ angle increase from North pole to South pole for fixed ψ angle.

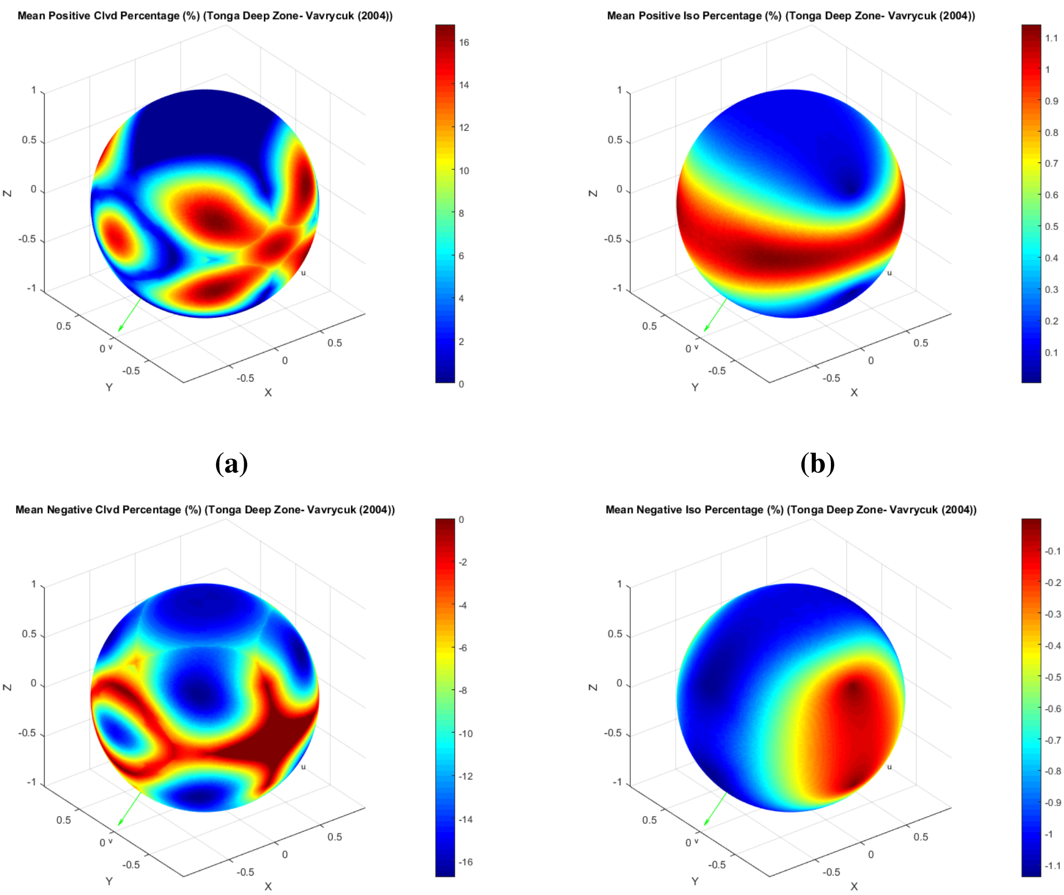

(a) **(b)**

(c) **(d)**

Figure 3.26. Percentage of mean positive and negative CLVD (a) and ISO (b) parts of earthquake source of Tonga Deep Zone for Normal Fault. Red arrow (**u**) and green arrow (**v**) are slip vector and fault normal, respectively. Red colored areas imply high percentages and dark blue colored areas imply low or zero percentages for positive result. Indication of colors are reversed for negative results. ψ angle increase from left to right on figures. ϕ angle increase from North pole to South pole for fixed ψ angle.

3.2.4.3. Dip-Slip Fault. Results of non-DC components of Tonga Deep Zone elasticity tensor for dip-slip fault are plotted in Figure 3.27 and 3.28.

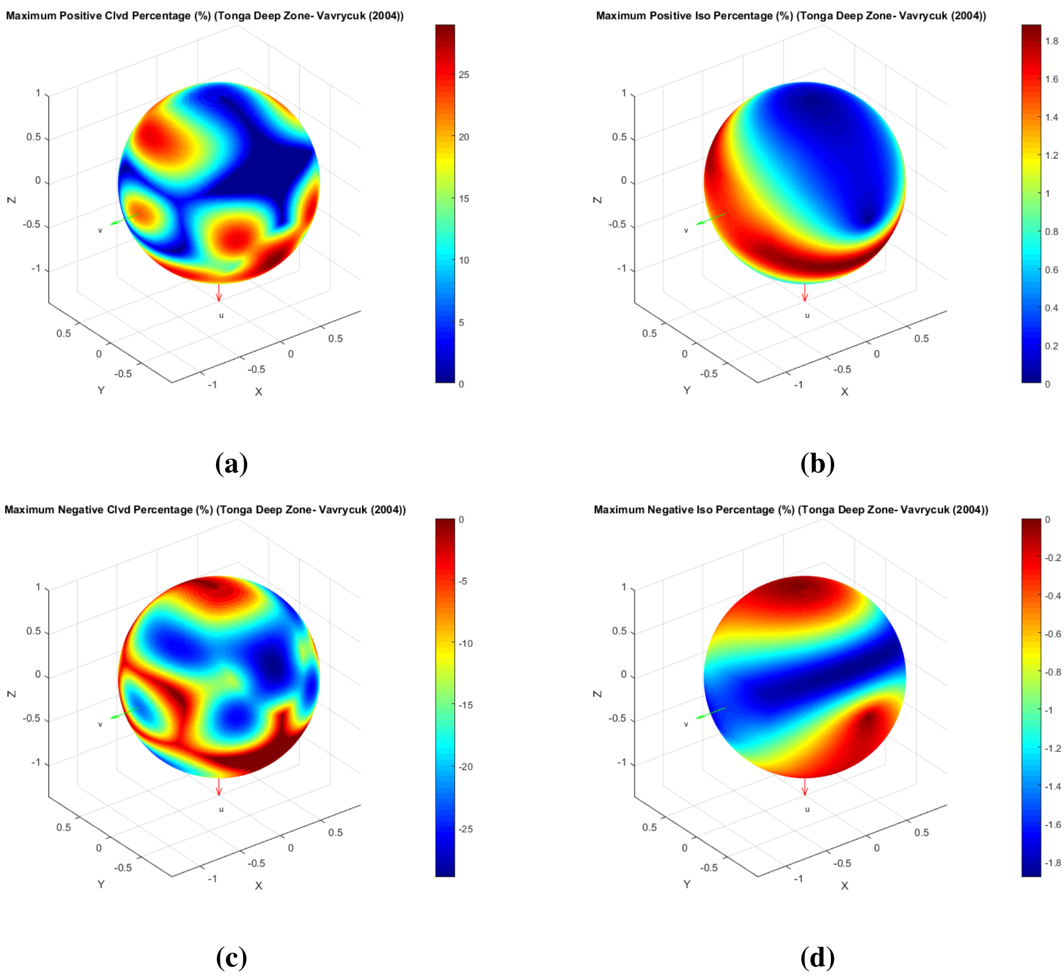

Figure 3.27. Percentage of maximum positive and negative CLVD (a) and ISO (b) parts of earthquake source of Tonga Deep Zone for Dip-Slip Fault. Red arrow (**u**) and green arrow (**v**) are slip vector and fault normal, respectively. Red colored areas imply high percentages and dark blue colored areas imply low or zero percentages for positive result. Indication of colors are reversed for negative results. ψ angle increase from left to right on figures. ϕ angle increase from North pole to South pole for fixed ψ angle.

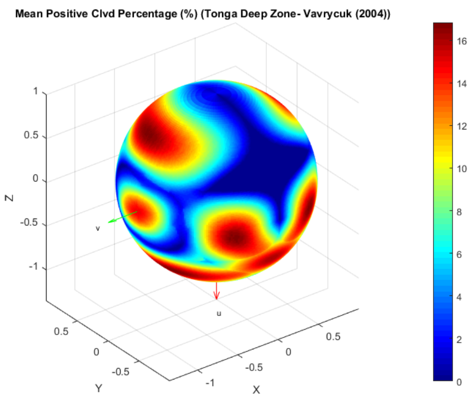

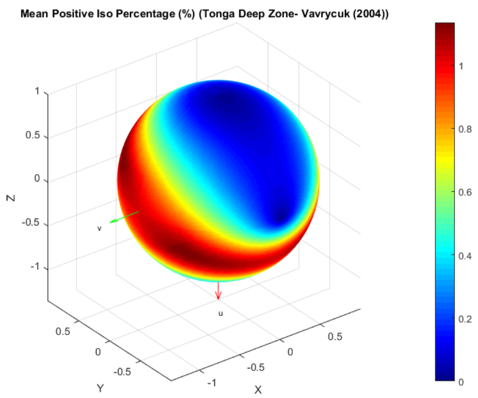

(a) **(b)**

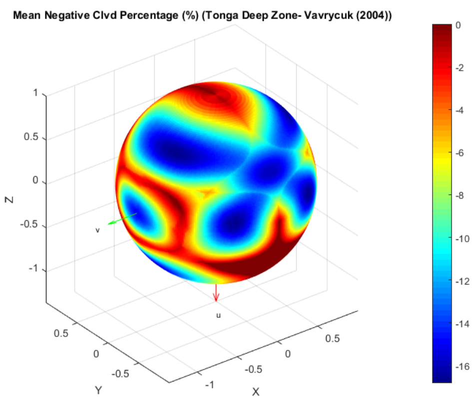

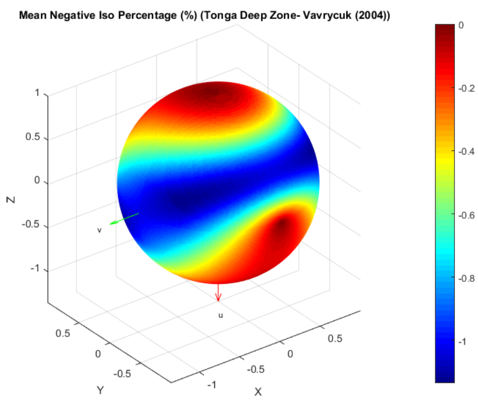

(c) **(d)**

Figure 3.28. Percentage of mean positive and negative CLVD (a) and ISO (b) parts of earthquake source of Tonga Deep Zone for Dip-Slip Fault. Red arrow (**u**) and green arrow (**v**) are slip vector and fault normal, respectively. Red colored areas imply high percentages and dark blue colored areas imply low or zero percentages for positive result. Indication of colors are reversed for negative results. ψ angle increase from left to right on figures. ϕ angle increase from North pole to South pole for fixed ψ angle.

3.2.4.4. Left Lateral Strike Slip Fault. Results of non-DC components of Tonga Deep Zone elasticity tensor for left lateral strike slip fault are plotted in Figure 3.29 and 3.30.

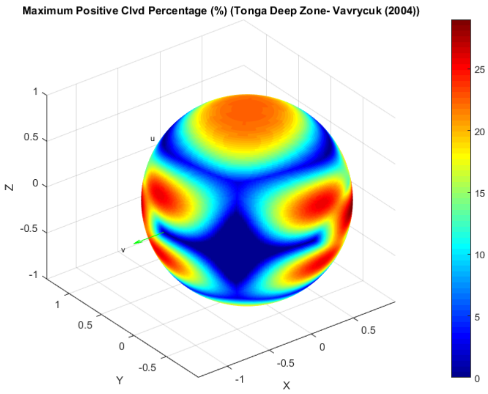

(a)

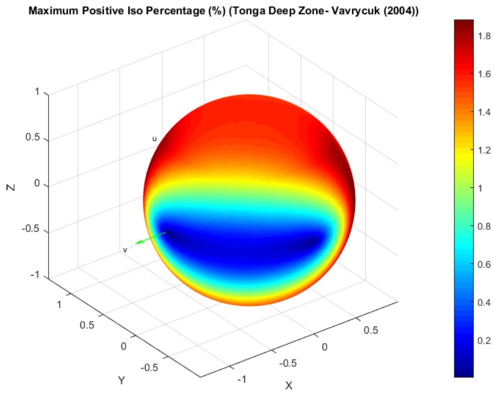

(b)

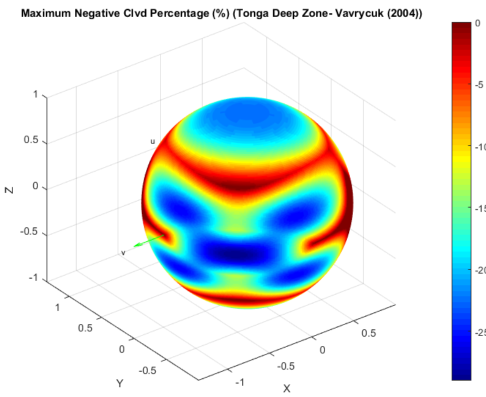

(c)

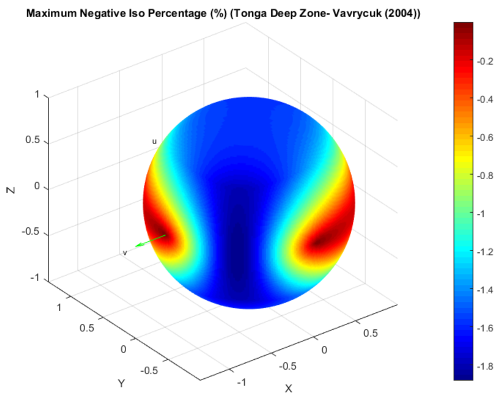

(d)

Figure 3.29. Percentage of maximum positive and negative CLVD (a) and ISO (b) parts of earthquake source of Tonga Deep Zone for Left Lateral Strike Slip Fault. Red arrow (**u**) and green arrow (**v**) are slip vector and fault normal, respectively. Red colored areas imply high percentages and dark blue colored areas imply low or zero percentages for positive result. Indication of colors are reversed for negative results. ψ angle increase from left to right on figures. ϕ angle increase from North pole to South pole for fixed ψ angle.

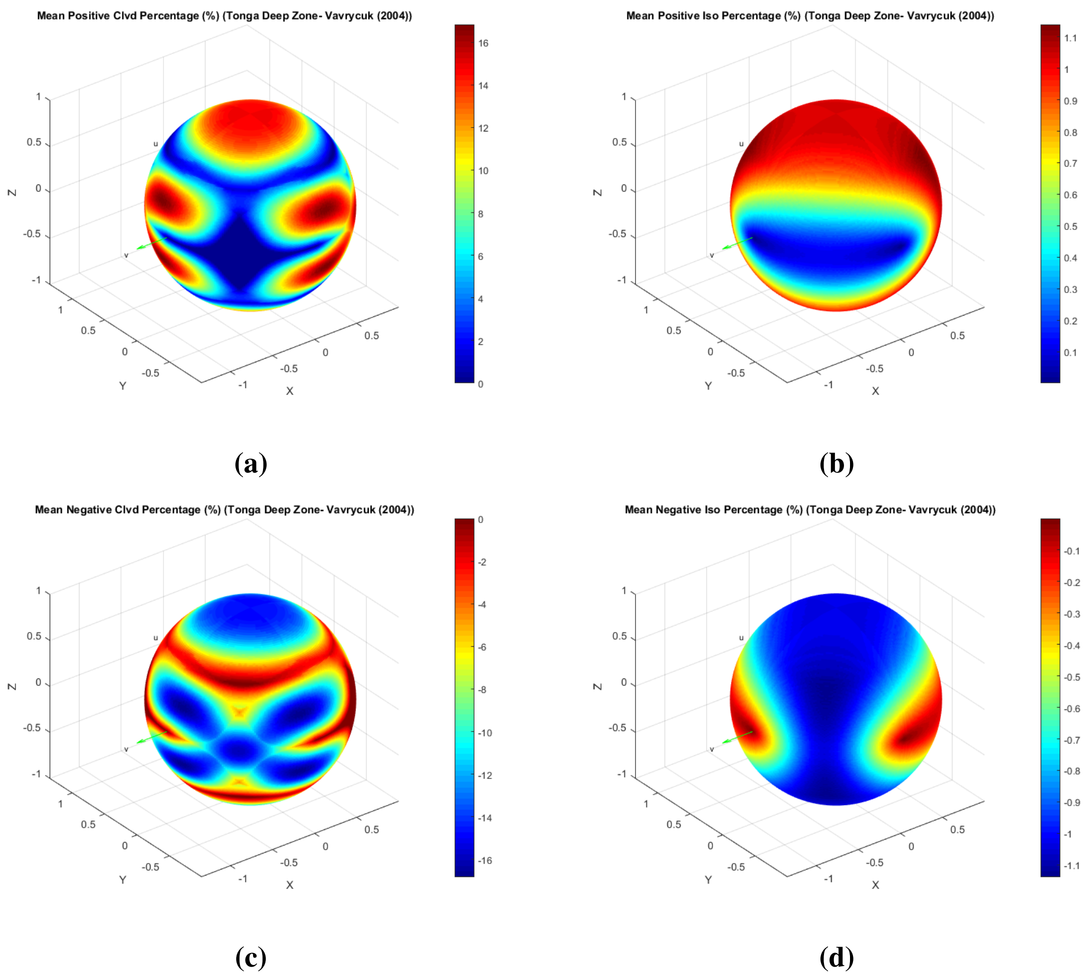

Figure 3.30. Percentage of mean positive and negative CLVD (a) and ISO (b) parts of earthquake source of Tonga Deep Zone for Left Lateral Strike Slip Fault. Red arrow (**u**) and green arrow (**v**) are slip vector and fault normal, respectively. Red colored areas imply high percentages and dark blue colored areas imply low or zero percentages for positive result. Indication of colors are reversed for negative results. ψ angle increase from left to right on figures. ϕ angle increase from North pole to South pole for fixed ψ angle.

<u>3.2.4.5. Right Lateral Strike Slip Fault.</u> Results of non-DC components of Tonga Deep Zone elasticity tensor for right lateral strike slip fault are plotted in Figure 3.31 and 3.32.

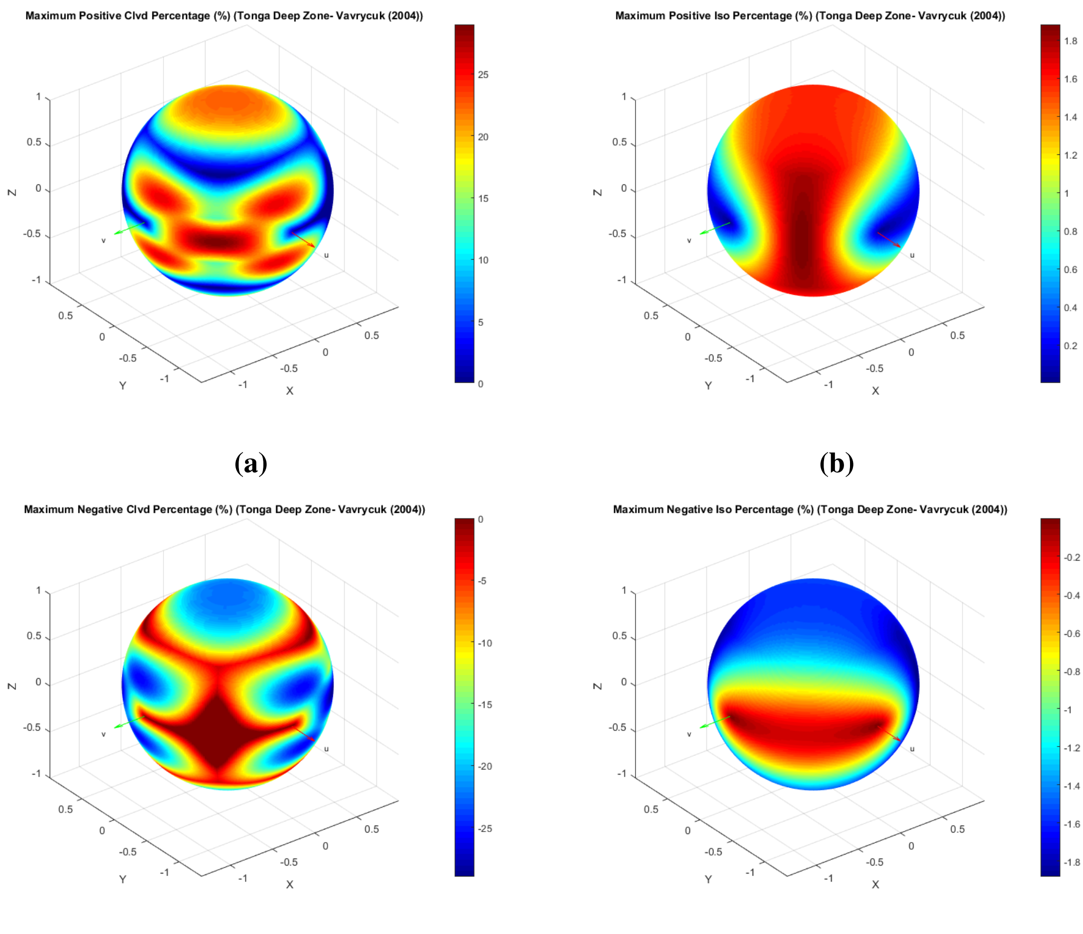

(c) **(d)**

Figure 3.31. Percentage of maximum positive and negative CLVD (a) and ISO (b) parts of earthquake source of Tonga Deep Zone for Right Lateral Strike Slip Fault. Red arrow (**u**) and green arrow (**v**) are slip vector and fault normal, respectively. Red colored areas imply high percentages and dark blue colored areas imply low or zero percentages for positive result. Indication of colors are reversed for negative results. ψ angle increase from left to right on figures. ϕ angle increase from North pole to South pole for fixed ψ angle.

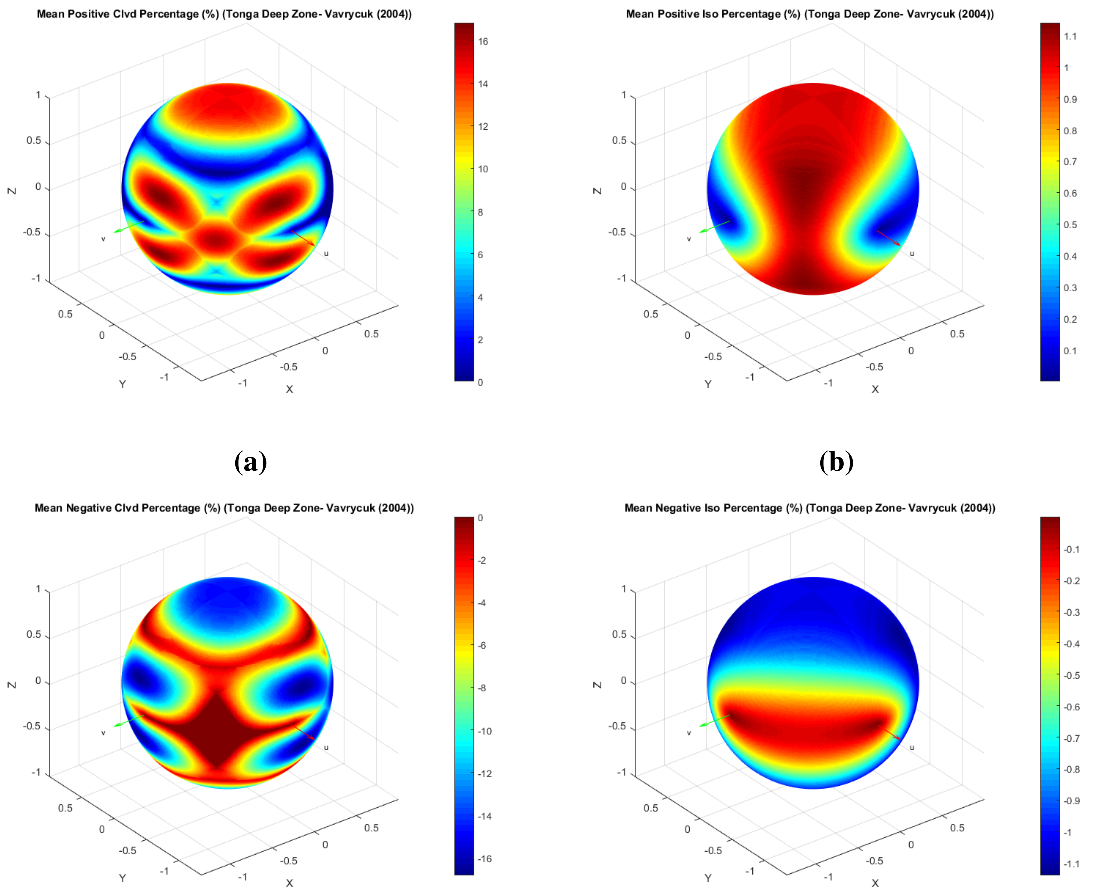

(a) **(b)**

(c) **(d)**

Figure 3.32. Percentage of mean positive and negative CLVD (a) and ISO (b) parts of earthquake source of Tonga Deep Zone for Right Lateral Strike Slip Fault. Red arrow (**u**) and green arrow (**v**) are slip vector and fault normal, respectively. Red colored areas imply high percentages and dark blue colored areas imply low or zero percentages for positive result. Indication of colors are reversed for negative results. ψ angle increase from left to right on figures. ϕ angle increase from North pole to South pole for fixed ψ angle.

3.2.5. Albite

Albite has monoclinic symmetry thus it is sensitivity on θ Euler angle. We plot the maximum and mean values of variation of fault parameters. Results can be seen in Figure 3.33 and Figure 3.34

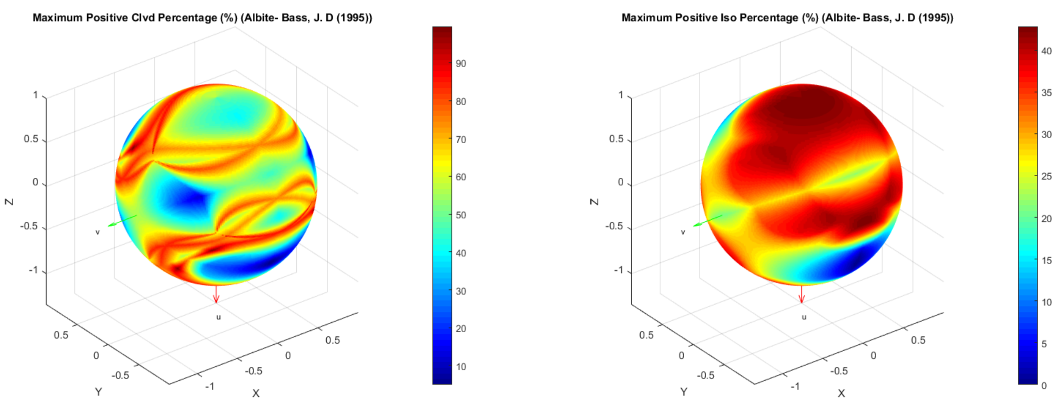

(a) **(b)**

Figure 3.33. Percentage of maximum CLVD (a) and ISO (b) parts of earthquake source of Albite. Red arrow (**u**) and green arrow (**v**) are slip vector and fault normal, respectively. Red colored areas imply high percentages and dark blue colored areas imply low or zero percentages. ψ angle increase from left to right on figures. ϕ angle increase from North pole to South pole for fixed ψ angle.

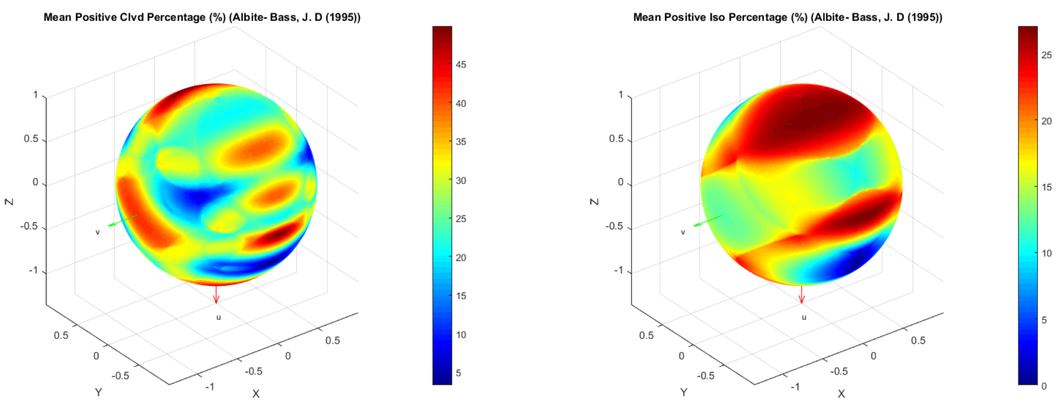

(a) **(b)**

Figure 3.34. Percentage of mean CLVD (a) and ISO (b) parts of earthquake source of Albite. Red arrow (**u**) and green arrow (**v**) are slip vector and fault normal, respectively. Red colored areas imply high percentages and dark blue colored areas imply low or zero percentages. ψ angle increase from left to right on figures. ϕ angle increase from North pole to South pole for fixed ψ angle.

3.2.6. Sanidine

Sanidine mineral is the second material with monoclinic symmetry. We plot the maximum and mean values of variation of fault parameters. Results can be seen in Figure 3.35 and Figure 3.36.

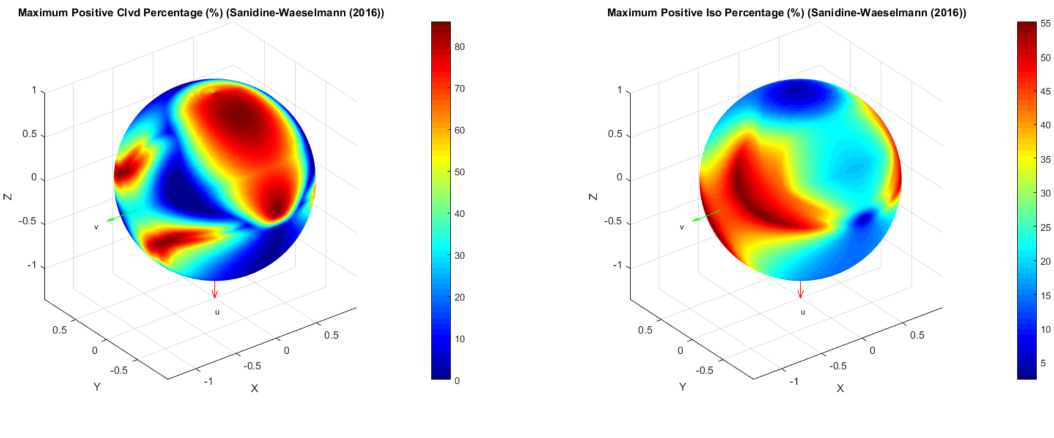

(a) **(b)**

Figure 3.35. Percentage of maximum CLVD (a) and ISO (b) parts of earthquake source of Sanidine. Red arrow (**u**) and green arrow (**v**) are slip vector and fault normal, respectively. Red colored areas imply high percentages and dark blue colored areas imply low or zero percentages. ψ angle increase from left to right on figures. ϕ angle increase from North pole to South pole for fixed ψ angle.

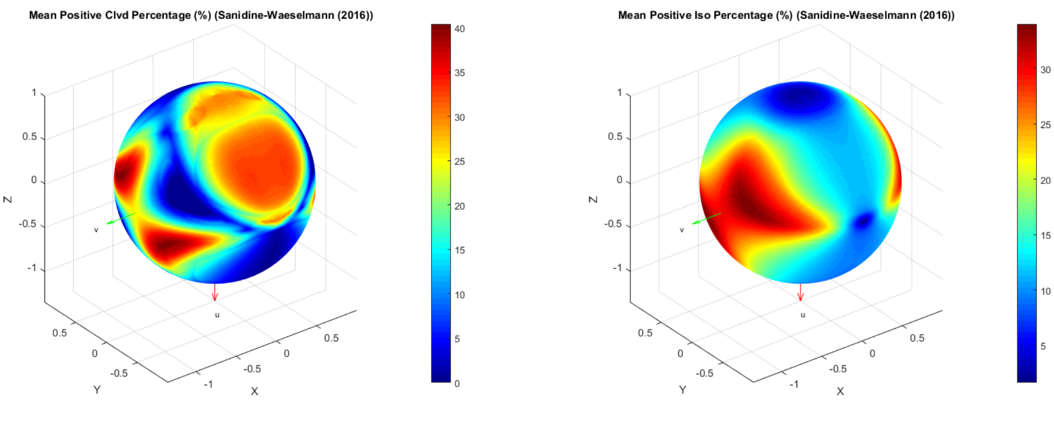

(a) **(b)**

Figure 3.36. Percentage of mean CLVD (a) and ISO (b) parts of earthquake source of Sanidine. Red arrow (**u**) and green arrow (**v**) are slip vector and fault normal, respectively. Red colored areas imply high percentages and dark blue colored areas imply low or zero percentages. ψ angle increase from left to right on figures. ϕ angle increase from North pole to South pole for fixed ψ angle.

3.3. Distance From Closest Isotropic Space

Distance from isotropic spaces for a given anisotropic elasticity tensors are calculated by using the equation A.3. In order to calculate it, one should first calculate the closest isotropic elasticity tensor for given anisotropic elasticity tensor by using equation 2.58. In order to test it, we find closest isotropic elasticity tensors of anisotropic elasticity tensors that we use.

Our assumption is that variation of fault parameters and percentages of non-DC components are related to distance from isotropic space of the material. Results can be seen in table 3.1

Table 3.1. Table of Distance From Isotropic Spaces

	Gneiss	Amphibolite	Granite
Distance to Isotropic Space	14.3316	13.3192	1.7171
	Tonga Deep Zone	Albite	Sanidine
	7.8662	170.7883	185.0637

3.3.1. MTEX Results

In order to test our assumption we also want to correlate these results with a well known open source software named MTEX. P wave anisotropy percentage and S wave percentage for all possible rotation of each elasticity tensor are calculated. P wave anisotropy percentages are shown in table 3.2 and S wave anisotropy percentages are in Figure 3.37, Figure 3.38, Figure 3.39, Figure 3.40, Figure 3.41 and Figure 3.42.

Table 3.2. P Wave Anisotropy (%)

	Gneiss	Amphibolite	Granite
P wave Anisotropy (%)	17.8488	13.3074	4.5179
	Tonga Deep Zone	Albite	Sanidine
	7.3344	46.8890	46.8748

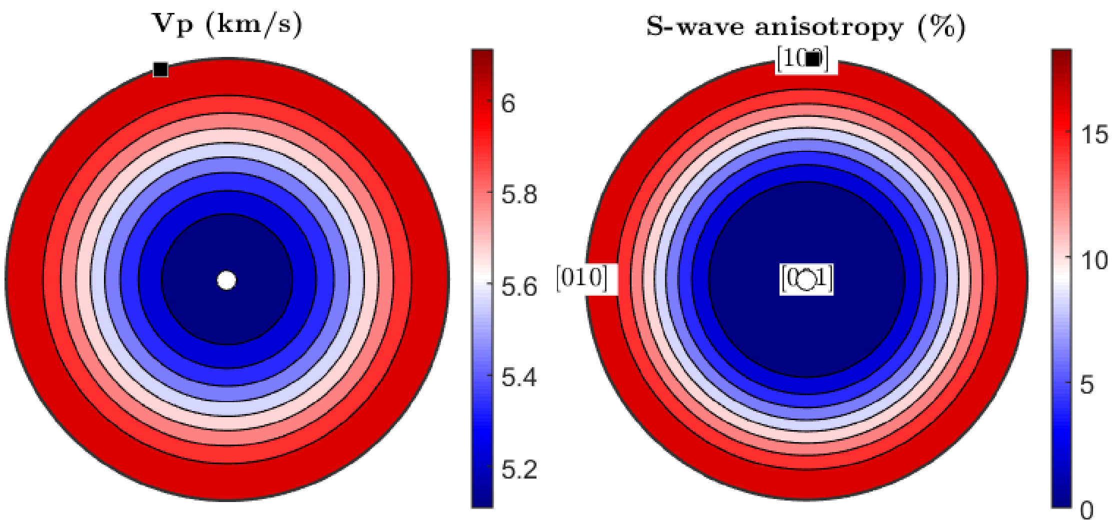

Figure 3.37. P & S wave anisotropies, velocities and polarization and P/S wave ratio of Gneiss

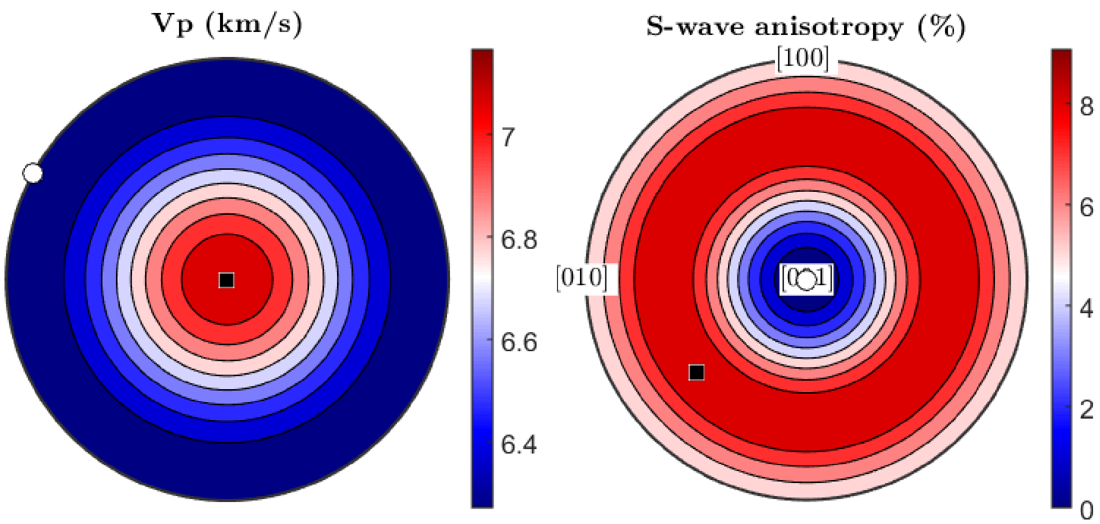

Figure 3.38. P & S wave anisotropies, velocities and polarization and P/S wave ratio of Amphibolite

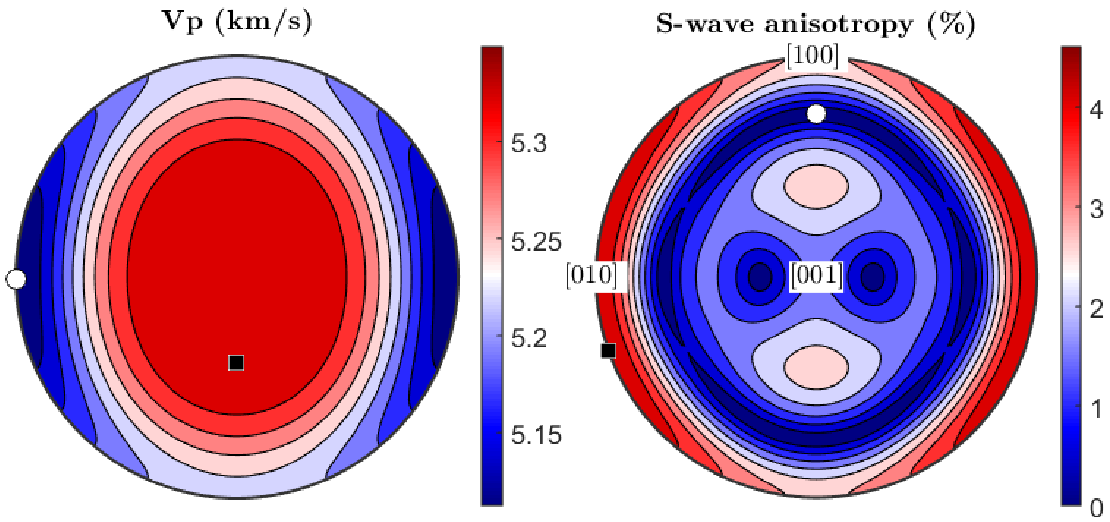

Figure 3.39. P & S wave anisotropies, velocities and polarization and P/S wave ratio of Granite

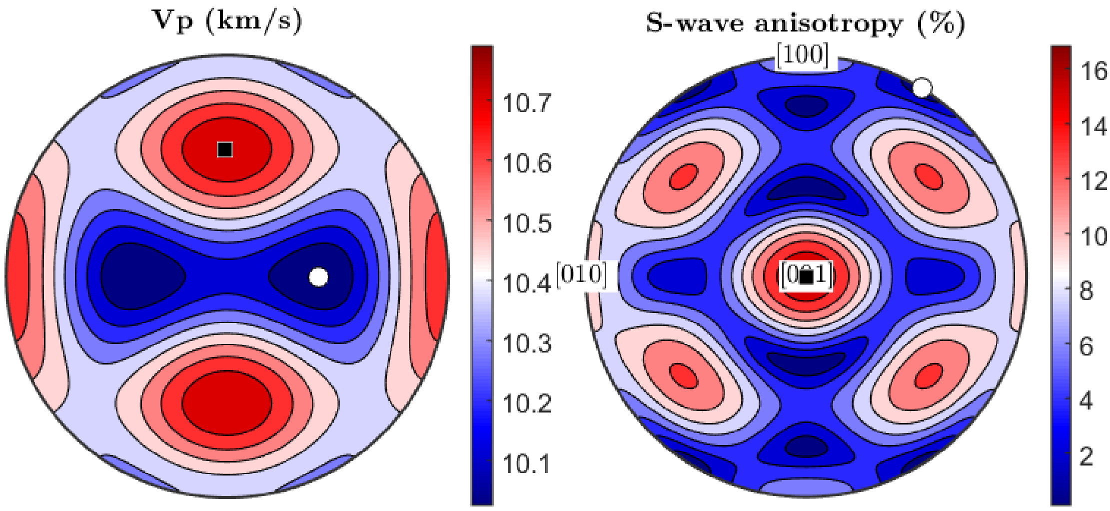

Figure 3.40. P & S wave anisotropies, velocities and polarization and P/S wave ratio of Tonga Deep Zone

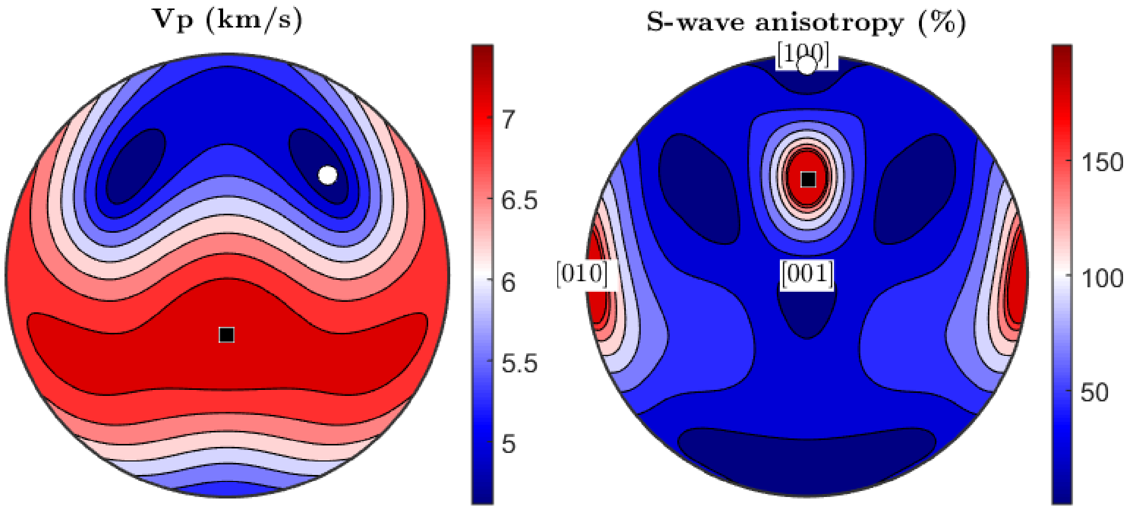

Figure 3.41. P & S wave anisotropies, velocities and polarization and P/S wave ratio of Albite

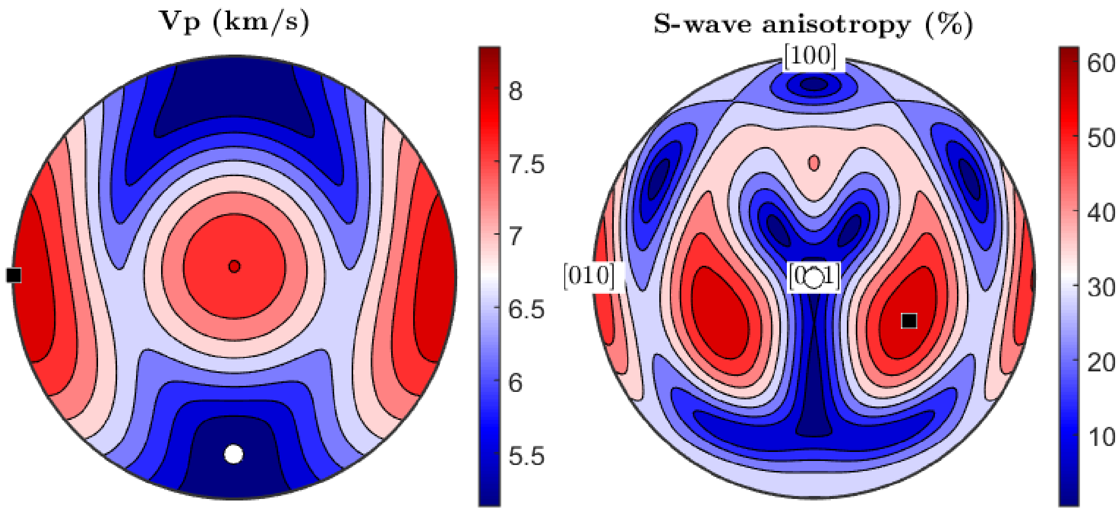

Figure 3.42. P & S wave anisotropies, velocities and polarization and P/S wave ratio of Sanidine

4. DISCUSSION

In this chapter decomposition, distance from isotropic space and MTEX results are represented. Compared numerical results can be found in Table 3.1, Table 3.2 and Table 4.1.

Non-DC decomposition results have the same amount of positive and negative parts, where positive and negative non-DC shows the forces. Figures are positive results for all materials except Tonga Deep Zone. Although we plotted these results in different figures, numerical values are equal to each other in absolute sense.

Two different materials with TI symmetry class generate almost same percentage of CLVD component. However shape of the figures, which shows the CLVD component for different orientation of elasticity tensor, are different (Figure 3.19a and Figure 3.20a). ISO components have the same shape with different percentages (Figure 3.19b and Figure 3.20b). Positive and negative percentages are generated at the same face of the sphere but in different hemisphere. Maximum CLVD% in absolute sense has eight different but relevant ϕ and ψ combination which are 45, 135, 225 and 315 degrees of ψ and 45 and 135 degrees of ϕ. Gneiss' ISO% and Amphibolite's CLVD% percentages get their maximum values in absolute sense in 270 degree of ψ and 45 degree of ϕ. Variation of strike, dip and rake angles of Gneiss and Amphibolite are comperable (Figures 3.1 and 3.2). Variation of strike, dip and rake angles of Gneiss almost two time higher than Amphibolite. But both of these materials get their maximum variations on almost same specific combination of ϕ and ψ.

Table 4.1. Moment Tensor Decomposition Results of Elasticity Tensors

<table>
<tr><th colspan="2"></th><th>Gneiss</th><th>Amphibolite</th><th>Granite</th><th>Tonga Deep Zone</th><th>Albite</th><th>Sanidine</th></tr>
<tr><td rowspan="2">Strike</td><td>Max</td><td rowspan="2">10.00</td><td rowspan="2">5.00</td><td>2.50</td><td>9.00</td><td>90.00</td><td>35.00</td></tr>
<tr><td>Mean</td><td>2.20</td><td>6.00</td><td>32.00</td><td>20.00</td></tr>
<tr><td rowspan="2">Dip</td><td>Max</td><td rowspan="2">5.00</td><td rowspan="2">1.80</td><td>1.20</td><td>4.50</td><td>90.00</td><td>19.00</td></tr>
<tr><td>Mean</td><td>1.00</td><td>2.50</td><td>16.00</td><td>16.00</td></tr>
<tr><td rowspan="2">Rake</td><td>Max</td><td rowspan="2">10.00</td><td rowspan="2">5.00</td><td>2.50</td><td>9.00</td><td>90.00</td><td>35.00</td></tr>
<tr><td>Mean</td><td>2.20</td><td>6.00</td><td>32.00</td><td>20.00</td></tr>
<tr><td rowspan="2">± CLVD (%)</td><td>Max</td><td rowspan="2">30.00</td><td rowspan="2">25.00</td><td>9.50</td><td>30.00</td><td>100.00</td><td>80.00</td></tr>
<tr><td>Mean</td><td>7.30</td><td>16.00</td><td>48.00</td><td>40.00</td></tr>
<tr><td rowspan="2">± ISO (%)</td><td>Max</td><td rowspan="2">0.04</td><td rowspan="2">11.00</td><td>5.50</td><td>1.80</td><td>41.00</td><td>55.00</td></tr>
<tr><td>Mean</td><td>4.00</td><td>1.20</td><td>26.00</td><td>33.00</td></tr>
</table>

Distances from the isotropic space of Gneiss and Amphibolite are close to each other (Table 3.1). Gneiss and Amphibolite P wave velocity anisotropies are correlated with variation of fault plane angles, 6% and 8% respectively. S wave anisotropy of Amphibolite is close to P wave anisotropy, however, Gneiss has two times bigger S wave anisotropy percentage with respect to P wave anisotropy (Table 4.1). P wave anisotropy percentage of TI materials are almost identical. S wave anisotropy percentages, however, are not correlated with each other (Figure 3.37 and 3.38). Both non-DC and fault parameters of Granite and Amphibolite generate similar shapes with [9] which used theoretical elasticity tensor on moment tensor decomposition. There might be a correlation between moment tensor decomposition results for TI symmetry classes.

Materials with orthotropic elasticity tensor generate different percentages of non-DC components (Figures 3.21 and Figures 3.27). Granite can produce 9.5 CLVD% and 5.5 ISO% sources whereas Tonga Deep Zone can produce 30 CLVD% and 1.8 ISO%. Distances from the isotropic space of Granite and Tonga Deep Zone are 1.7171 and 7.8662, respectively (Table 3.1). Both of these orthotropic materials are close to isotropic space compared with TI materials which are 14.3316 and 13.3192 (Table 4.1). Even if Tonga Deep Zone is relatively close to isotropic space, it generates almost same amount of non-DC component as TI materials (Table 4.1). Maximum CLVD% figures of Granite have full correlation with CLVD% of Gneiss. ISO% figures are also correlated with each other (Figures 3.19b, 3.21b). Granite and Tonga Deep Zone, however, have no similarities on both CLVD% and ISO% plots (Figures 3.21b, 3.9c). Tonga Deep Zone gets maximum CLVD% with similar to Granite but it also have high percentages on other ϕ and ψ combinations. ISO% results of Tonga Deep Zone has non-zero values in almost every combination of ϕ and ψ. P wave anisotropies of Granite and Tonga Deep Zone are 4.5179 and 7.3344 percentages, respectively (Figure 3.39 and 3.40). They produces different amount of non-DC percentage even if their P wave anisotropy percentages are relatively close to each other. S wave anisotropy percentages are, however, not close to each other (Figure 3.39 and 3.40). S wave anisotropy of Granite is four times bigger than Tonga Deep Zone. ISO results are $\pm$ 5% and $\pm$ 1% for Granite and Tonga Deep Zone, respectively. Percentages of ISO parts of earthquake sources are related with the distance from isotropic space of their elasticity tensors. Shape of the CLVD percentage figures of Granite are similar to Gneiss material even if they have different symmetry classes (Figure 3.19a and Figure 3.21a). Variation of fault parameters are slightly different with each other which can be correlated with the distance from isotropic spaces (Figures 3.3 and 3.9). Fault plane parameters of Granite can vary 2.5 degrees for strike and rake and 1.2 degrees for dip angles. Tonga Deep Zone can produce 9 degrees of strike and rake and 4.5 degrees of dip angles. Shape of variation of dip angle are both similar for Granite and Tonga Deep Zone (Figures 3.3b and 3.9b).

Tonga Deep Zone is decomposed for five different fault types. Results show that fault plane does not effect the amount of non-DC components and variations of fault plane parameters but effect the shape of the plot (Figures 3.5, 3.7, 3.9, 3.11, 3.13, 3.23, 3.25, 3.27, 3.29 and 3.31). We expect this result since both the magnitude and shape of the elasticity tensor remain same.

Monoclinic materials, Albite and Sanidine, can generate huge amount of non-DC components and fault plane parameters can change vastly. Shear sources in isotropic source region generate pure DC. Strike, dip and rake angles are the same angles of fault planes. Both Albite and Sanidine can generate so great percentages of non-DC components that one cannot describe the earthquake with fault plane parameters. Albite, for instance, can generate $\pm$ 100 CLVD% component (Figure 3.33a) in which case the fault parameters are not meaningful anymore. Albite mineral can also generate up to $\pm$ 41 ISO% component (Figure 3.33b). Sanidine material can generate up to $\pm$ 80 CLVD% (Figure 3.35a) and $\pm$ 55 ISO% component (Figure 3.35b). Both Sanidine and Albite generate their maximum CLVD and ISO percentages on different orientation. One must recall that an earthquake cannot generate more than 100% source. Even though Sanidine material has no similarity with TI materials its dip and rake angle variation figures are similar to TI materials (Figures 3.1, 3.2 and 3.17). Strike, dip and rake angle variation of Albite mineral can be up to 90 degree (Figures 3.15). Sanidine, on the other hand, can generate maximum 35 degree strike and rake angle variation and 19 degree dip angle variation (Figure 3.17). There are discontinuities in fault plane angle parameter variations of both Albite and Sanidine. This can be linked with high amount of non-DC percentages of the earthquake sources. Variation of dip angle of Sanidine, however, has similarities with Gneiss and Amphibolite (Figures 3.1b, 3.17b). Distance from the isotropic space of Albite and Sanidine are 170.7883 and 185.7883, respectively (Table 3.1). They are more than 10 times farther from the isotropic space than TI materials. P wave anisotropy of these materials are 46.8890 and 46.8748 which is correlating with the results of isotropic space distances. S wave anisotropies are, however, not correlate P wave anisotropy results. S wave anisotropy percentages of Albite and Sanidine are 190% and 60%, respectively (Figures 3.41 and 3.42).

5. CONCLUSION

Conclusions can be summarized as follows,

i. Shear faults in anisotropic source region can generate huge amount of non-DC components depending on the strength of the anisotropy.
ii. The amount of non-DC components are related with the symmetry class of anisotropic material.
iii. Fault types cannot change the amount of non-DC components or strike, dip and rake angles but it can change the orientation of figures.
iv. Variation of non-DC components and strike, dip and rake angles are determined by the anisotropic material's distance from isotropic space. Materials which are farther from isotropic space produce more non-DC components and strike, dip and rake angles varied from original value.
v. Materials with TI symmetry generate a particular type of certain type of non-DC and strike, dip and rake angles plots.
vi. In order to visualize moment tensor decomposition result of a material with sensitivity on θ, e.g. orthotropic and monoclinic elasticity tensors, angle one can take the mean or maximum values on θ angle. Maximum values can be a good way to understand the capabilities of anisotropic source region.
vii. CLVD and ISO results of moment tensor decomposition can be positive and negative. Negative and positive results have always same percentage in absolute sense.
viii. Monoclinic elasticity tensors can produce such high amount of non-DC components that it can be hard to interpret the earthquake source as a shear source. In some combination of Φ, ψ and θ monoclinic source region can produce almost $\pm$ 100% CLVD source. Moreover, in some cases combination of ISO and CLVD parts of earthquake can be up to $\pm$ 100% as well. In such cases strike, dip and rake angles cannot explain the fault.
ix. There is a correlation between the material's distance from isotropic space and P wave anisotropy percentage of the material. Materials which are farther from isotropic space have more P wave anisotropy percentages. S wave anisotropy percentages, however, are

not correlated with neither P wave anisotropy nor distance from isotropic space.

REFERENCES

1. Aki, K. and P. G. Richards, “Quantitati6e Seismology: Theory and Methods”, , 1980.

2. Diner, Ç., M. Kochetov and M. A. Slawinski, “Identifying symmetry classes of elasticity tensors using monoclinic distance function”, *Journal of Elasticity*, Vol. 102, No. 2, pp. 175–190, 2011.

3. Knopoff, L. and M. J. Randall, “The compensated linear-vector dipole: A possible mechanism for deep earthquakes”, *Journal of Geophysical Research*, Vol. 75, No. 26, pp. 4957–4963, 1970.

4. Hudson, J., “Wave speeds and attenuation of elastic waves in material containing cracks”, *Geophysical Journal International*, Vol. 64, No. 1, pp. 133–150, 1981.

5. Fitch, T. J., D. W. McCOWAN and M. W. Shields, “Estimation of the seismic moment tensor from teleseismic body wave data with applications to intraplate and mantle earthquakes”, *Journal of Geophysical Research: Solid Earth*, Vol. 85, No. B7, pp. 3817–3828, 1980.

6. Sipkin, S. A., “Interpretation of non-double-couple earthquake mechanisms derived from moment tensor inversion”, *Journal of Geophysical Research: Solid Earth*, Vol. 91, No. B1, pp. 531–547, 1986.

7. Kuge, K. and T. Lay, “Data-dependent non-double-couple components of shallow earthquake source mechanisms: Effects of waveform inversion instability”, *Geophysical research letters*, Vol. 21, No. 1, pp. 9–12, 1994.

8. Vavryčuk, V., “Inversion for parameters of tensile earthquakes”, *Journal of Geophysical Research: Solid Earth*, Vol. 106, No. B8, pp. 16339–16355, 2001.

9. Vavryčuk, V., “Focal mechanisms in anisotropic media”, *Geophysical Journal Interna-*

tional, Vol. 161, No. 2, pp. 334–346, 2005.

10. Vavryčuk, V., "Tensile earthquakes: Theory, modeling, and inversion", *Journal of Geophysical Research: Solid Earth*, Vol. 116, No. B12, 2011.

11. Vavryčuk, V., "Inversion for anisotropy from non-double-couple components of moment tensors", *Journal of Geophysical Research: Solid Earth*, Vol. 109, No. B7, 2004.

12. Vavryčuk, V., "Elastodynamic and elastostatic Green tensors for homogeneous weak transversely isotropic media", *Geophysical Journal International*, Vol. 130, No. 3, pp. 786–800, 1997.

13. Fojtíková, L., V. Vavryčuk, A. Cipciar and J. Madarás, "Focal mechanisms of microearthquakes in the Dobrá Voda seismoactive area in the Malé Karpaty Mts.(Little Carpathians), Slovakia", *Tectonophysics*, Vol. 492, No. 1, pp. 213–229, 2010.

14. Stierle, E., V. Vavryčuk, J. Šílenỳ and M. Bohnhoff, "Resolution of non-double-couple components in the seismic moment tensor using regional networksI: a synthetic case study", *Geophysical Journal International*, Vol. 196, No. 3, pp. 1869–1877, 2014.

15. Babuska, V. and M. Cara, *Seismic anisotropy in the Earth*, Vol. 10, Springer Science & Business Media, 1991.

16. Rabbel, W. and W. D. Mooney, "Seismic anisotropy of the crystalline crust: what does it tell us?", *Terra Nova*, Vol. 8, No. 1, pp. 16–21, 1996.

17. Silver, P. G., "Seismic anisotropy beneath the continents: probing the depths of geology", *Annual review of earth and planetary sciences*, Vol. 24, pp. 385–432, 1996.

18. Savage, M., "Seismic anisotropy and mantle deformation: what have we learned from shear wave splitting?", *Reviews of Geophysics*, Vol. 37, No. 1, pp. 65–106, 1999.

19. Ross, A., G. Foulger and B. R. Julian, "Non-double-couple earthquake mechanisms at

the Geysers geothermal area, California", *Geophysical Research Letters*, Vol. 23, No. 8, pp. 877–880, 1996.

20. Julian, B., A. Miller and G. Foulger, "Non-double-couple earthquake mechanisms at the Hengill-Grensdalur volcanic complex, southwest Iceland", *Geophysical Research Letters*, Vol. 24, No. 7, pp. 743–746, 1997.

21. Evison, F. F., "Earthquakes and faults", *Bulletin of the Seismological Society of America*, Vol. 53, No. 5, pp. 873–891, 1963.

22. Bridgeman, P., "Polymorphic transitions and geologic phenomena", *Am. J. Sci. A*, Vol. 243, pp. 90–97, 1945.

23. Kirby, S. H., W. B. DuRHAM and L. A. Stern, "Mantle phase changes and deep-earthquake faulting in subducting lithosphere", *Science*, Vol. 252, No. 5003, pp. 216–225, 1991.

24. Benioff, H., "Earthquake source mechanisms", *Science*, Vol. 143, No. 3613, pp. 1399–1406, 1964.

25. Bernal, J., "Discussion", *Observatory*, Vol. 59, p. 268, 1936.

26. Musgrave, M. J., "Crystal acoustics", , 1970.

27. Helbig, K., *Foundations of anisotropy for exploration seismics*, Vol. 22, Pergamon Press, 1994.

28. Cerveny, V., *Seismic ray theory*, Cambridge university press, 2005.

29. Kawasaki, I. and T. Tanimoto, "Radiation patterns of body waves due to the seismic dislocation occurring in an anisotropic source medium", *Bulletin of the Seismological Society of America*, Vol. 71, No. 1, pp. 37–50, 1981.

30. Kuge, K. and H. Kawakatsu, “Deep and intermediate-depth non-double couple earthquakes: interpretation of moment tensor inversions using various passbands of very broadband seismic data”, *Geophysical Journal International*, Vol. 111, No. 3, pp. 589–606, 1992.

31. Julian, B. R., A. D. Miller and G. Foulger, “Non-double-couple earthquakes 1. Theory”, *Reviews of Geophysics*, Vol. 36, No. 4, pp. 525–549, 1998.

32. Herrmann, R. B., “A student’s guide to the use of P and S wave data for focal mechanism determination”, *Seismological Research Letters*, Vol. 46, No. 4, pp. 29–39, 1975.

33. Bos, L., P. Gibson, M. Kotchetov and M. Slawinski, “Classes of anisotropic media: a tutorial”, *Studia Geophysica et Geodaetica*, Vol. 48, No. 1, pp. 265–287, 2004.

34. Rudajev, V. and J. Šílenỳ, “Seismic events with non-shear component: II. Rock bursts with implosive source component”, *Pure and Applied Geophysics*, Vol. 123, No. 1, pp. 17–25, 1985.

35. Šílenỳ, J. and A. Milev, “Source mechanism of mining induced seismic events—resolution of double couple and non double couple models”, *Tectonophysics*, Vol. 456, No. 1, pp. 3–15, 2008.

36. Rößler, D., F. Krüger and G. Rümpker, “Retrieval of moment tensors due to dislocation point sources in anisotropic media using standard techniques”, *Geophysical Journal International*, Vol. 169, No. 1, pp. 136–148, 2007.

37. Udías, A., R. Madariaga, E. Buforn *et al.*, *Source Mechanisms of Earthquakes: Theory and Practice*, Cambridge University Press, 2014.

38. Gilbert, F., “Derivation of source parameters from low-frequency spectra”, *Philosophical Transactions for the Royal Society of London. Series A, Mathematical and Physical Sciences*, pp. 369–371, 1973.

39. Jost, M. u. and R. Herrmann, "A student's guide to and review of moment tensors", *Seismological Research Letters*, Vol. 60, No. 2, pp. 37–57, 1989.

40. Dziewonski, A., T.-A. Chou and J. Woodhouse, "Determination of earthquake source parameters from waveform data for studies of global and regional seismicity", *Journal of Geophysical Research: Solid Earth*, Vol. 86, No. B4, pp. 2825–2852, 1981.

41. Frohlich, C., "The nature of deep-focus earthquakes", *Annual Review of Earth and Planetary Sciences*, Vol. 17, p. 227, 1989.

42. Kawakatsu, H., "Insignificant isotropic component in the moment tensor of deep earthquakes", *Nature*, Vol. 351, No. 6321, pp. 50–53, 1991.

43. Vavryčuk, V., "On the retrieval of moment tensors from borehole data", *Geophysical Prospecting*, Vol. 55, No. 3, pp. 381–391, 2007.

44. Panza, G. F. and A. Saraò, "Monitoring volcanic and geothermal areas by full seismic moment tensor inversion: are non-double-couple components always artefacts of modelling?", *Geophysical Journal International*, Vol. 143, No. 2, pp. 353–364, 2000.

45. Vavryčuk, V., "Non-double-couple earthquakes of 1997 January in West Bohemia, Czech Republic: evidence of tensile faulting", *Geophysical Journal International*, Vol. 149, No. 2, pp. 364–373, 2002.

46. Templeton, D. C. and D. S. Dreger, "Non-double-couple earthquakes in the Long Valley volcanic region", *Bulletin of the Seismological Society of America*, Vol. 96, No. 1, pp. 69–79, 2006.

47. Stickney, M. C. and K. F. Sprenke, "Seismic events with implosional focal mechanisms in the Coeur d'Alene mining district, Northern Idaho", *Journal of Geophysical Research: Solid Earth*, Vol. 98, No. B4, pp. 6523–6528, 1993.

48. Bachmann, F., R. Hielscher and H. Schaeben, "Texture analysis with MTEX–free and

open source software toolbox", *Solid State Phenomena*, Vol. 160, pp. 63–68, 2010.

49. Rabbel, W., T. Beilecke, T. Bohlen, D. Fischer, A. Frank, J. Hasenclever, G. Borm, J. Kück, K. Bram, G. Druivenga *et al.*, "Superdeep vertical seismic profiling at the KTB deep drill hole (Germany): Seismic close-up view of a major thrust zone down to 8.5 km depth", *Journal of Geophysical Research: Solid Earth*, Vol. 109, No. B9, 2004.

50. Takanashi, M., O. Nishizawa, K. Kanagawa and K. Yasunaga, "Laboratory measurements of elastic anisotropy parameters for the exposed crustal rocks from the Hidaka Metamorphic Belt, Central Hokkaido, Japan", *Geophysical Journal International*, Vol. 145, No. 1, pp. 33–47, 2001.

51. Simmons, G., H. Wang *et al.*, "Single crystal elastic constants and calculated aggregate properties", , 1971.

52. Waeselmann, N., J. M. Brown, R. J. Angel, N. Ross, J. Zhao and W. Kaminsky, "The elastic tensor of monoclinic alkali feldspars", *American Mineralogist*, Vol. 101, No. 5, pp. 1228–1231, 2016, `http://ammin.geoscienceworld.org/content/101/5/1228`.

53. Gazis, D. and R. Wallis, "Surface tension and surface modes in semi-infinite lattices", *Surface Science*, Vol. 3, No. 1, pp. 19–32, 1965.

APPENDIX A: DISTANCE FUNCTION

The best approximation in the Frobenius norm is the orthogonal projection $pr_{sym}(c)$ of tensor **c** on the linear space of all tensors on this class. The projection calculation can be written as below,

$$pr_{sym}(c) = \int_{G^{sym}} (g \circ c) d\mu(g), \tag{A.1}$$

where the integration is over the symmetry group G^{sym}. Its elements are g, represented as A matrix, with respect to the invariant measure μ [53].
Transformation on the space of elasticity tensor is given by $C \longrightarrow ACA^T$. Because tensors $c - pr_{sym}(c)$ and $pr_{sym}(c)$ are normal to one another, we have

$$\left\| c - pr_{sym}(c) \right\|^2 = \|C\|^2 - \left\| pr_{sym}(c) \right\|^2 \tag{A.2}$$

It can be written as,

$$d_{sym}^2 = \|C\|^2 - \|C^{sym}\|^2 \tag{A.3}$$

Distance from monoclinic space of a given elasticity tensor (in Kelvin notation), for instance, can be found as below,

$$dist_{mono} = 2(C_{14}^2 + C_{24}^2 + C_{34}^2 + C_{15}^2 + C_{25}^2 + C_{35}^2 + C_{46}^2 + C_{56}^2) \tag{A.4}$$

APPENDIX B: VOIGT AND KELVIN NOTATIONS OF ELASTICITY TENSOR

Due to the symmetry of stress and strain tensor, elasticity tensor can be written in a matrix form which contains six independent equations. This allows us to express elasticity tensor as an elasticity matrix. Components of elasticity tensor, 36, can be written as 6×6 elasticity matrix.
Since c_{ijkl} is symmetric 81 components of c_{ijpq} reduces to 21 components.

$$c = \begin{bmatrix} C_{1111} & C_{1122} & C_{1133} & C_{1123} & C_{1131} & C_{1112} \\ * & C_{2222} & C_{2233} & C_{2223} & C_{2231} & C_{2212} \\ * & * & C_{3333} & C_{3323} & C_{3331} & C_{3312} \\ * & * & * & C_{2323} & C_{2331} & C_{2312} \\ * & * & * & * & C_{3131} & C_{3112} \\ * & * & * & * & * & C_{1212} \end{bmatrix}$$

$$c_{ijpq} = c_{jipq} = c_{ijqp} = c_{pqij} \tag{B.1}$$

$$\sigma_{ij} = c_{ijpq}\varepsilon_{pq} \tag{B.2}$$

$$\varepsilon_{pq} = \frac{1}{2}(u_{p,q} + u_{q,p}) \tag{B.3}$$

Since ij and pq are symmetric, one can define these terms as,

$$ij \leftrightarrow k$$

$$pq \leftrightarrow l$$

Such symmetry can also be applied to c_{ijkl}, and it becomes,

$$c_{ijpq} = C_{kl}$$

Due to these symmetries, we can define each couple as one index:

$$11 \leftrightarrow 1$$

$$22 \leftrightarrow 2$$

$$33 \leftrightarrow 3$$

$$23 \leftrightarrow 4$$

$$13 \leftrightarrow 5$$

$$12 \leftrightarrow 6$$

This allows us to write elasticity tensor in a matrix form:

$$C = \begin{bmatrix} C_{11} & C_{12} & C_{13} & C_{14} & C_{15} & C_{16} \\ * & C_{22} & C_{23} & C_{24} & C_{25} & C_{26} \\ * & * & C_{33} & C_{34} & C_{35} & C_{36} \\ * & * & * & C_{44} & C_{45} & C_{46} \\ * & * & * & * & C_{55} & C_{56} \\ * & * & * & * & * & C_{66} \end{bmatrix}$$

As an example, C_{12} corresponds to c_{1122} and C_{54} corresponds to c_{1323}. Hence, stress-strain for a general elastic continuum that obeys Hooke's Law can be written as

$$\begin{bmatrix} \sigma_{11} \\ \sigma_{22} \\ \sigma_{33} \\ \sigma_{23} \\ \sigma_{13} \\ \sigma_{12} \end{bmatrix} = \begin{bmatrix} C_{11} & C_{12} & C_{13} & C_{14} & C_{15} & C_{16} \\ * & C_{22} & C_{23} & C_{24} & C_{25} & C_{26} \\ * & * & C_{33} & C_{34} & C_{35} & C_{36} \\ * & * & * & C_{44} & C_{45} & C_{46} \\ * & * & * & * & C_{55} & C_{56} \\ * & * & * & * & * & C_{66} \end{bmatrix} \begin{bmatrix} \varepsilon_{11} \\ \varepsilon_{22} \\ \varepsilon_{33} \\ 2\varepsilon_{23} \\ 2\varepsilon_{13} \\ 2\varepsilon_{12} \end{bmatrix} \tag{B.4}$$

where the stress and the strain tensor components are mapped to the matrix for as below,

$$\begin{bmatrix} \sigma_{11} & \sigma_{12} & \sigma_{13} \\ \sigma_{12} & \sigma_{22} & \sigma_{23} \\ \sigma_{13} & \sigma_{23} & \sigma_{33} \end{bmatrix} \rightarrow \begin{bmatrix} \sigma_{11} \\ \sigma_{22} \\ \sigma_{33} \\ \sigma_{23} \\ \sigma_{13} \\ \sigma_{12} \end{bmatrix}, \begin{bmatrix} \varepsilon_{11} & \varepsilon_{12} & \varepsilon_{13} \\ \varepsilon_{12} & \varepsilon_{22} & \varepsilon_{23} \\ \varepsilon_{13} & \varepsilon_{23} & \varepsilon_{33} \end{bmatrix} \rightarrow \begin{bmatrix} \varepsilon_{11} \\ \varepsilon_{22} \\ \varepsilon_{33} \\ 2\varepsilon_{23} \\ 2\varepsilon_{13} \\ 2\varepsilon_{12} \end{bmatrix} \tag{B.5}$$

This representation is called Voigt notation. This allows us to represent second-rank strain and stress tensors as a vector in six dimensional space. The Voigt mapping preserves the elastic energy denstiy and the elasticity tensor. However, one can easily notice that some stress and strain tensors are treated differently. Thus we lose all advantages of tensor algebra. In order to preserve the equivalency of last three row of stress and strain tensor, one can use Kelvin notation.

$$\begin{bmatrix} \sigma_{11} & \sigma_{12} & \sigma_{13} \\ \sigma_{12} & \sigma_{22} & \sigma_{23} \\ \sigma_{13} & \sigma_{23} & \sigma_{33} \end{bmatrix} \rightarrow \begin{bmatrix} \sigma_{11} \\ \sigma_{22} \\ \sigma_{33} \\ \sqrt{2}\sigma_{23} \\ \sqrt{2}\sigma_{13} \\ \sqrt{2}\sigma_{12} \end{bmatrix}, \begin{bmatrix} \varepsilon_{11} & \varepsilon_{12} & \varepsilon_{13} \\ \varepsilon_{12} & \varepsilon_{22} & \varepsilon_{23} \\ \varepsilon_{13} & \varepsilon_{23} & \varepsilon_{33} \end{bmatrix} \rightarrow \begin{bmatrix} \varepsilon_{11} \\ \varepsilon_{22} \\ \varepsilon_{33} \\ \sqrt{2}\varepsilon_{23} \\ \sqrt{2}\varepsilon_{13} \\ \sqrt{2}\varepsilon_{12} \end{bmatrix} \tag{B.6}$$

Then, the stress-strain equation can be written as,

$$\begin{bmatrix} \sigma_{11} \\ \sigma_{22} \\ \sigma_{33} \\ \sqrt{2}\sigma_{23} \\ \sqrt{2}\sigma_{13} \\ \sqrt{2}\sigma_{12} \end{bmatrix} = \begin{bmatrix} c_{1111} & c_{1122} & c_{1133} & \sqrt{2}c_{1123} & \sqrt{2}c_{1113} & \sqrt{2}c_{1112} \\ c_{2211} & c_{2222} & c_{2233} & \sqrt{2}c_{2223} & \sqrt{2}c_{2213} & \sqrt{2}c_{2212} \\ c_{3311} & c_{3322} & c_{3333} & \sqrt{2}c_{3323} & \sqrt{2}c_{3313} & \sqrt{2}c_{3312} \\ \sqrt{2}c_{1123} & \sqrt{2}c_{2223} & \sqrt{2}c_{3323} & 2c_{2323} & 2c_{1313} & 2c_{1313} \\ \sqrt{2}c_{1113} & \sqrt{2}c_{2213} & \sqrt{2}c_{3313} & 2c_{2313} & 2c_{1313} & 2c_{1312} \\ \sqrt{2}c_{1112} & \sqrt{2}c_{2212} & \sqrt{2}c_{3312} & 2c_{2312} & 2c_{1312} & 2c_{1212} \end{bmatrix} \begin{bmatrix} \varepsilon_{11} \\ \varepsilon_{22} \\ \varepsilon_{33} \\ \sqrt{2}\varepsilon_{23} \\ \sqrt{2}\varepsilon_{13} \\ \sqrt{2}\varepsilon_{12} \end{bmatrix} \tag{B.7}$$

This notation enables us to use tensor algebra for the matrix presentation in 6D. Kelvin mapping preserves the elastic energy density. Norms of the three tensors are preserved. Stress and strain are treated identically. However, the value of elasticity tensor components are changed.

In order to decompose moment tensor, elasticity tensors are defined in Voigt notation.

APPENDIX C: SYMMETRY CLASSES

C.1. Isotropic

For isotropic elasticity tensor, all coordinate systems are natural coordinate systems. No particular orientation is required. Isotropic elasticity tensor is of the form

$$C^{ISO} = \begin{bmatrix} C_{11} & C_{11}-2C_{44} & C_{11}-2C_{44} & 0 & 0 & 0 \\ C_{11}-2C_{44} & C_{11} & C_{11}-2C_{44} & 0 & 0 & 0 \\ C_{11}-2C_{44} & C_{11}-2C_{44} & C_{11} & 0 & 0 & 0 \\ 0 & 0 & 0 & C_{44} & 0 & 0 \\ 0 & 0 & 0 & 0 & C_{44} & 0 \\ 0 & 0 & 0 & 0 & 0 & C_{44} \end{bmatrix}$$

In isotropic elasticity tensor, there only two independent elastic parameters; namely, C_{11} and C_{44}. These two are also called Lamé parameters. C_{44} is called rigidity and $C_{11}-2C_{44}$ is callad first Lamé parameter.

C.2. Cubic

For cubic symmetry, coordinate axes which are aligned with 4-fold rotation axes of the cube. One can show cubic symmetry in matrix form as below,

$$C^{CUBIC} = \begin{bmatrix} C_{11} & C_{12} & C_{12} & 0 & 0 & 0 \\ C_{12} & C_{11} & C_{12} & 0 & 0 & 0 \\ C_{12} & C_{12} & C_{11} & 0 & 0 & 0 \\ 0 & 0 & 0 & C_{44} & 0 & 0 \\ 0 & 0 & 0 & 0 & C_{44} & 0 \\ 0 & 0 & 0 & 0 & 0 & C_{44} \end{bmatrix}$$

In cubic elasticity tensor, there are three independent elastic parameters; namely, C_{11},C_{12} and C_{44}.

C.3. Tetragonal

Tetragonal symmetry class contains a 4-fold rotation and a reflection through the plane that contains the axis of rotation. If e_3 is parallel to the axis of rotation, then natural basis is where e_1 and e_2 are parallel of the normal of any two orthogonal symmetry planes. Matrix representation of a tetragonal elasticity tensor in a matrix form as below,

$$C^{TETRA} = \begin{bmatrix} C_{11} & C_{12} & C_{13} & 0 & 0 & 0 \\ C_{12} & C_{11} & C_{13} & 0 & 0 & 0 \\ C_{13} & C_{13} & C_{33} & 0 & 0 & 0 \\ 0 & 0 & 0 & C_{44} & 0 & 0 \\ 0 & 0 & 0 & 0 & C_{44} & 0 \\ 0 & 0 & 0 & 0 & 0 & C_{66} \end{bmatrix}$$

One can notice that, the only difference between tetragonal and TI is that C_{66} parameter of the matrix.

C.4. Trigonal

Trigonal symmetry class contains a 3-fold rotation. If e_3 is parallel to the axis of rotation, then natural basis is where either e_1 or e_2 is aligned with the normal of any two orthogonal symmetry planes. Matrix representation of a trigonal elasticity tensor with respect to natural basis in a matrix form as below,

$$C^{TRIGONAL} = \begin{bmatrix} C_{11} & C_{12} & C_{13} & C_{14} & C_{15} & 0 \\ C_{12} & C_{11} & C_{13} & -C_{14} & -C_{15} & 0 \\ C_{13} & C_{13} & C_{33} & 0 & 0 & 0 \\ C_{14} & C_{14} & 0 & C_{44} & 0 & -C_{15} \\ C_{15} & -C_{15} & 0 & 0 & C_{44} & C_{14} \\ 0 & 0 & 0 & -C_{15} & C_{14} & \frac{C_{11}-C_{12}}{2} \end{bmatrix}$$

C.5. Generally Anisotropic

Generally anisotropic is the most general form that describes stress-strain equations. It can be shown as a matrix as below,

$$C^{GENANISO} = \begin{bmatrix} C_{11} & C_{12} & C_{13} & C_{14} & C_{15} & C_{16} \\ C_{12} & C_{22} & C_{23} & C_{24} & C_{25} & C_{26} \\ C_{13} & C_{23} & C_{33} & C_{34} & C_{35} & C_{36} \\ C_{14} & C_{24} & C_{34} & C_{44} & C_{45} & C_{46} \\ C_{15} & C_{25} & C_{35} & C_{45} & C_{55} & C_{56} \\ C_{16} & C_{26} & C_{36} & C_{46} & C_{56} & C_{66} \end{bmatrix}$$

Generally anisotropic elasticity tensor only have point symmetry. It has twenty one independent parameters.